Observatório Nacional

DISSERTAÇÃO DE MESTRADO

EVALUATION OF THE DYNAMICAL STATE OF THE HIGH-REDSHIFT GALAXY CLUSTER SPT-CL J2215-3537

VINICIUS DOS SANTOS BESSA RIBEIRO

RIO DE JANEIRO
2025

Ministério da Ciência, Tecnologia, Inovações e Comunicações
Observatório Nacional
Programa de Pós-Graduação

Dissertação de Mestrado

EVALUATION OF THE DYNAMICAL STATE OF THE HIGH-REDSHIFT GALAXY CLUSTER SPT-CL J2215-3537

por

Vinicius dos Santos Bessa Ribeiro

Dissertação submetida ao Corpo Docente do Programa de Pós-graduação em Astronomia do Observatório Nacional, como parte dos requisitos necessários para a obtenção do Grau de Mestre em Astronomia.

Orientador: Dr. Renato de Alencar Dupke

Rio de Janeiro, RJ – Brasil
Setembro de 2025

d484 dos Santos Bessa Ribeiro, Vinicius
Evaluation of the Dynamical State of the High-redshift Galaxy Cluster SPT-CL J2215-3537 [Rio de Janeiro] 2025.
xxii, 71 p. 29,7 cm: graf. il. tab.

Dissertação (mestrado) - Observatório Nacional - Rio de Janeiro, 2025.

1. Galaxy clusters. 2. Intracluster medium. 3. Dynamical state. 4. X-ray. I. Observatório Nacional. II. Título.

CDU 000.000.000

“EVALUATION OF THE DYNAMICAL STATE OF THE HIGH-REDSHIFT GALAXY CLUSTER SPT-CL J2215-3537”

VINICIUS DOS SANTOS BESSA RIBEIRO

DISSERTAÇÃO SUBMETIDA AO CORPO DOCENTE DO PROGRAMA DE PÓS-GRADUAÇÃO EM ASTRONOMIA DO OBSERVATÓRIO NACIONAL COMO PARTE DOS REQUISITOS NECESSÁRIOS PARA A OBTENÇÃO DO GRAU DE MESTRE EM ASTRONOMIA.

Aprovada por:

Dr. Renato de Alencar Dupke – Observatório Nacional (Orientador)

Dra. Clarissa Martins Siqueira – Observatório Nacional

Dr. Raimundo Lopes de Oliveira Filho – Universidade Federal de Sergipe

RIO DE JANEIRO, RJ – BRASIL
2 DE SETEMBRO DE 2025

believe it or not
this very if
is everything you got

— *Paulo Leminski*

Agradecimentos

Nada de valor genuíno pode ser alcançado de forma solitária. Para que as potências humanas se concretizem, é necessário que haja ação no mundo. O homem conhece a verdadeira gentileza ao ser afetado por aqueles de coração gentil; a criança desenvolve sua curiosidade e pensamento crítico ao ser instigada pelas mentes curiosas. Nesse sentido, sou profundamente grato aos colegas, amigos, familiares e mentores que, sobretudo através dos seus bons exemplos, moldaram-me de algum modo.

Agradeço à minha mãe, Adriana Bessa, pelo amor, apoio e educação. Ao meu pai, pelo amor e por nutrir em mim o gosto pelo conhecimento desde cedo. Aos meus tios, Andresa e Jean-Antoine, pelo carinho e por terem sido boas influências intelectuais. Ao meu irmão, Victor Bessa, do quem tenho muito orgulho. Aos meus primos, Jean Jr. e Eduardo, os quais considero como irmãos. Agradeço ainda aos meus amigos de longuíssima data, Adailton, Henrique e Pedro Paulo. Curiosamente, eles estudam física, química e biologia, respectivamente, formando a tríade da ciência. Henrique, em especial, é um amigo como poucos nesse mundo. Ainda me espanto como conseguimos conversar de forma tão fluida independentemente do meio de comunicação (sério, até no chat do chess.com). Aos meus antigos colegas da UFC, Alessandro, Iury e Márcio, sinto saudade de nossas fantásticas conversas sobre física.

Também agradeço imensamente a todos que conheci durante o mestrado. Primeiramente ao meu orientador, Dr. Renato Dupke, que foi fundamental para o amadurecimento acadêmico que adquiri nos últimos anos. Lembro-me de mandar um primeiro email dizendo que tinha interesse em estudar estruturas em larga escala. Na primeira entrevista, Renato disse algo como "Huh, então você quer estudar estruturas em larga escala, não é?", e prosseguiu para apresentar com entusiasmo três projetos que o interessavam na época. O projeto que desenvolvemos foi marcado por um ambiente de real interesse pelas questões científicas que nos propusemos a investigar e, acima de tudo, pela liberdade de explorar ideias e métodos sem que fôssemos excessivamente restringidos por receitas ou manuais. Em resumo, eu não poderia ter pedido por uma orientação melhor. Ainda na linha de mentores, sou extremamente grato ao Dr. Alberto Ardila, ao Dr. Eduardo Telles, ao Dr. Jailson Alcaniz e ao Dr. Raimundo Lopes, por terem ministrado disciplinas de forma instigante e por representarem para mim exemplos de pesquisadores de excelência. Ao Dr. Rafael Eufrásio, que é também uma inspiração para mim desde que fui a uma

palestra sua no IFCE em 2015 sobre astronomia multimensageira. Posteriormente, Rafael foi meu co-orientador de IC e me proporcionou valiosas lições de astronomia e análise de dados. À Dra. Mariana Penna Lima, por ter me orientado no DESC e ter gentilmente acompanhado minha trajetória desde o fim da graduação. À Dra. Yolanda Jiménez-Teja pelas úteis discussões durante reuniões do grupo e pelo apoio com o artigo do projeto. Agradeço também aos colegas de grupo, Dr. Nícolas Oliveira, Dra. Rebeca Batalha, Juliana Duarte e Ricardo Marzall.

Agradeço a todos os funcionários e colaboradores do observatório, em especial Mari e Ana Maria, que foram sempre muito gentis e prestativas. À Giane Boldrim e Christianne Garnier, por proporcionarem mais emoção nos corredores do prédio e por terem me ajudado inúmeras vezes com questões burocráticas, que eram frequentemente mais desafiadores do que a pesquisa em si. Devo agradecer aos amigos que fiz no ON. Primeiramente ao Romualdo Eleutério, a quem, por alguma razão, sinto que conheço há uns 10 anos. De fato, um amigo e cientista raiz que admiro imensamente! À Mariane Dias, cuja personalidade, gentileza e dedicação muito me admira, e por sempre deixar chás na minha mesa, que eram muito apreciados após longas madrugadas de trabalho. À Maria Eduarda (Duda), pela maravilhosa amizade, apoio, papos reflexivos, e cafés na copa. Agradeço ao Patrick Prado, que é um cara extremamente prestativo, engenhoso e gente fina, além de ter sido uma referência para mim no grupo de Raios-X (e no vôlei). Ao Vinicius Sanches, meu xará, parceiro de júri da IOAA, primeira referência quando o assunto é jatos e AGN's, um grande amigo que me apoiou em diversos momentos do mestrado. Ao Antonis Leon (A.K.A Toninho), não poderia ter tido um colega de sala melhor, simplesmente a pessoa mais autêntica, gente fina e engraçada do prédio. Ao Ícaro Meidem pelo apoio em momentos variados e pelo alto astral com que leva a vida. Agradeço ainda ao Alessandro, Débora, Eddie, Éfren, Elis, Ester, Gabriela, Raquel e Rodolpho pelo companheirismo no dia a dia. Agradeço aos membros da banca, Dra. Clarissa Martins e Dr. Raimundo Lopes, pelas valiosas sugestões para a melhoria deste manuscrito. Por fim, agradeço à fundamental ajuda financeira proporcionada pela CAPES e pela FAPERJ.

Vinicius dos Santos Bessa Ribeiro

EVALUATION OF THE DYNAMICAL STATE OF THE HIGH-REDSHIFT GALAXY CLUSTER SPT-CL J2215-3537

RESUMO

A determinação precisa do estado dinâmico de aglomerados de galáxias é crítica para a cosmologia de aglomerados, uma vez que processos próximos ao equilíbrio no meio intra-aglomerado de sistemas dinamicamente relaxados permitem a derivação da distribuição de massa e outras importantes relações de escala com incertezas mínimas. Recentemente, o aglomerado de galáxias SPT-CL J2215-3537 ($z = 1.16$) foi identificado como um dos aglomerados relaxados mais distantes usando o critério de *symmetry–peakiness–alignment* (SPA), que consiste na construção de estatísticas morfológicas de raios-X para avaliar o grau de relaxamento. No entanto, SPT-CLJ0615-5746 ($z = 0.97$), previamente classificado como relaxado pelo critério SPA, mostrou sinais de estar em estado de fusão quando analisado pela fração de luz intra-aglomerado e por análises tradicionais de raios-X. O presente trabalho tem como objetivo avaliar o estado dinâmico de SPT-CL J2215-3537 por meio de análises espectrais e de imagem em raios-X. A caracterização das propriedades termodinâmicas do meio intra-aglomerado e de suas características morfológicas revela assinaturas de frentes frias de oscilação no eixo SE-NW. Encontramos um candidato a cavidade fantasma e estimamos sua potência mecânica como $\log_{10}(P_{\rm cav}/10^{42}{\rm erg\ s^{-1}}) = 2.66 \pm 0.23$, indicando que o resfriamento radiativo excede fortemente o aquecimento por feedback da galáxia central ativa. Os resultados de nossa análise combinada sugerem que SPT-CL J2215-3537 está levemente perturbado. Utilizamos o modelo de precipitação regulada por feedback para mostrar que o núcleo do aglomerado provavelmente está em um estado transitório em direção a um ciclo estável de resfriamento-feedback nos próximos $\sim 100 \pm 70$ milhões de anos. Adicionalmente, recalculamos parâmetros morfológicos tradicionais de raios-X e apresentamos uma discussão sobre suas limitações para aglomerados em alto redshift.

Vinicius dos Santos Bessa Ribeiro

EVALUATION OF THE DYNAMICAL STATE OF THE HIGH-REDSHIFT GALAXY CLUSTER SPT-CL J2215-3537

ABSTRACT

The accurate determination of the dynamical state of galaxy clusters is critical for cluster cosmology, as near-equilibrium processes in the intracluster medium of dynamically relaxed systems enable the derivation of the mass distribution and other important scaling relations with minimal uncertainties. Recently the galaxy cluster SPT-CL J2215-3537 ($z = 1.16$) has been identified as one of the most distant relaxed cluster using the *symmetry–peakiness–alignment* (SPA) criterion, which consists in the construction of X-ray morphological statistics to assess the degree of relaxation. However, SPT-CLJ0615-5746 ($z = 0.97$), which was previously marked as relaxed by the SPA treatment, showed signs to be in a merging state when analyzed by the intracluster light fraction and traditional X-ray analysis. The present work aims to evaluate the dynamical state of SPT-CL J2215-3537 through X-ray spectral and imaging analyzes. The characterization of the thermodynamical properties of the intracluster medium and its morphological features reveals signatures of sloshing cold fronts in the SE-NW axis. We find a ghost cavity candidate and estimate its mechanical power as $\log_{10}(P_{\rm cav}/10^{42}{\rm erg\ s^{-1}}) = 2.66 \pm 0.23$, indicanting that radiative cooling strongly exceeds AGN feedback heating. The results from our combined analysis suggest that SPT-CL J2215-3537 is mildly disturbed. We use the feedback-regulated precipitation framework to show that the cluster's core is likely in a transient state towards a stable cooling-feedback cycle within the next $\sim 100 \pm 70$ Myr. We additionally recalculate traditional X-ray morphological parameters and present a discussion of its limitations for high-redshift clusters.

List of Figures

List of Tables

Contents

Chapter 1

Introduction

In the hierarchical model of structure formation, galaxy clusters are the most massive and recently formed gravitationally bound systems in the Universe (Kravtsov and Borgani 2012). Their evolution is governed by the continuous accretion of matter and potential mergers with nearby groups or clusters. The dynamical state of these systems can be investigated through spatially resolved spectroscopic analysis of the intracluster medium (ICM) in X-rays (Zhang et al. 2024). Determining the precise dynamical state is essential, as quasi-equilibrium processes in dynamically relaxed clusters allow the derivation of mass distributions and scaling relations with minimal uncertainty (Barnes et al. 2021).

Although the discovery of cool-core, relaxed clusters is favored due to their enhanced surface brightness, high-redshift objects are significantly affected by selection biases such as X-ray flux limits. Recently, the galaxy cluster SPT-CL J2215-3537 ($z = 1.16$) was identified as one of the most distant relaxed cluster known, based on the symmetry–peakiness–alignment (SPA) method (Mantz et al. 2022), which uses morphological X-ray statistics to evaluate structural relaxation (Mantz et al. 2015).

A cluster's dynamical state reflects the degree of disturbance in its gravitational potential and associated matter. If the cluster is in dynamical equilibrium, it is considered relaxed; otherwise, it is classified as disturbed, often due to ongoing mergers or recent accretion events. High-redshift clusters pose particular challenges for dynamical state assessments due to observational biases, such as limited X-ray flux sensitivity, which restrict the application of direct diagnostic methods. Automated classification techniques often rely on geometric features in X-ray images, such as asymmetry and centroid shift measures, under the assumption that disturbed 3D structures will project with asymmetries in 2D space.

Relaxed galaxy clusters are widely used to constrain key cosmological parameters, such as the baryon fraction and the Hubble parameter (Allen et al. 2004; Allen et al. 2008). These constraints are further strengthened when high-redshift clusters are included in the sample, as shown by Mantz et al. (2022). However, incorrect assessments of a cluster's dynamical state (especially at high redshift) can introduce significant systematic

errors in cosmological parameter estimation. Although recent classification methods based in the regularity of the X-ray emission were designed to be redshift-independent and robust to data quality variations (Mantz et al. 2015; Yuan and Han 2020), they can still yield inaccurate results due to intrinsic biases in high-redshift observations. For example, Jiménez-Teja et al. (2023) confirmed, using both X-ray and intracluster light (ICL) analyses, that SPT-CLJ0615-5746 was undergoing multiple mergers, contrary to its initial SPA-based classification as relaxed in Mantz et al. (2022).

SPT-CL J2215-3537 is a particularly intriguing system, since it has been classified as the most distant relaxed galaxy cluster and shows signs of an intense cooling flow, a prominent cool core, an active galactic nucleus (AGN), and high star formation rates in the central brightest cluster galaxy (BCG) (Calzadilla et al. 2023). If this characterization is confirmed, it would imply that highly evolved structures can already be in place at $z > 1$, in a cosmic era expected to be dominated by merging systems.

A re-evaluation of SPT-CL J2215-3537 using complementary X-ray imaging and spectral analyses is critical. The combination of high redshift, apparent relaxation, AGN activity, and central starburst makes it a key laboratory for studying the cooling-feedback cycle and structure formation in the early Universe. This research aims to assess the dynamical state of SPT-CL J2215-3537 through X-ray spectral and imaging analyses, enabling the characterization of the ICM's thermodynamic properties and its morphological features.

Chapter 2

Bibliographic Review

2.1 Galaxy Clusters and Groups

Clusters of galaxies are the largest gravitationally bound structures in the universe. These aggregates may contain hundreds of galaxies, with physical size typically varying from 0.2 to 2 Mpc and total masses that exceed 10^{14} $M_{\odot}$ (Sarazin 1988). The baryonic mass is dominated by the hot intracluster gas, which is roughly 3-10 times larger than the mass derived from the luminosity of galaxies, while dark matter dominates the gravitational potential, with a value of approximately 10 times that of the baryonic matter (Seward and Charles 2010). We can also have smaller systems of bound galaxies known as galaxy groups, which consist of up to a few dozen components. Despite this scale distinction, both clusters and groups can be defined as large-scale structures that accumulated enough matter to decouple from the Hubble expansion.

The number of galaxies in a cluster defines its *richness*. This measure depends on the adoption of some membership criteria, which must be preferably independent of distance and morphology. Another useful information about a cluster comes from the luminosity function of its galaxies. The differential luminosity function n(L)dL gives us the number of galaxies with luminosities lying in the range [L, L + dL]. Knowing the statistical distribution of luminosities for a given cluster allows to estimate its richness and even its distance from us (Sarazin 1988).

Many schemes have been proposed to classify clusters and groups of galaxies based on their morphological characteristics. Zwicky et al. (1968) proposed to classify the clusters as *compact*, *medium compact* and *open*, where these categories are related to the concentration of galaxies as they were seen on the photometric plate. Bautz and Morgan (1970) based their classification scheme (BM) on the dominance of the brightest galaxy in the cluster. That is, if the central dominant galaxy (cD) have a brightness and extension that stands out in comparison to the elliptical galaxies, the cluster is classified as type I. Clusters without that dominant object are classified as type III, while type II

Table 2.1: Properties of groups and clusters of galaxies.

Property	Groups	Clusters
Richness	2–30 galaxies	30–300 galaxies
Radial velocity dispersion	100–500 km s^{-1}	400–1400 km s^{-1}
Mass	$10^{12.5}$–10^{14} $M_\odot$	10^{14}–$10^{15.5}$ $M_\odot$
T_X	< 2 keV	2–14 keV
L_X	$< 10^{43}$ erg s^{-1}	10^{43}–10^{45} erg s^{-1}

Notes: Adapted from the book *Exploring the X-ray Universe* (Seward and Charles 2010).

would be an intermediary category. Rood and Sastry (1971) developed a classification system (RS) that takes in account the spatial distribution of the ten brightest galaxies in the cluster. As shown in Figure 2.1a, there are a total of six classes in the RS scheme:

cD: the cluster contains a central dominant galaxy.
B (binary): the cluster contains a dominant pair of luminous galaxies.
L (line): three or more of the brightest galaxies are disposed in a straight line.
C (core): four or more galaxies form a cluster core.
F (flat): the galaxies are disposed in a flattened shape.
I (irregular): the galaxies form an irregular distribution.

Generally, the categories in all of these schemes can be viewed as a sequential line from regular to irregular clusters. Struble and Rood (1982) arranged the RS classes based on this hierarchical behaviour. The fork arrangement in Figure 2.1b shows clearly the evolutionary trend from irregular to cD clusters.

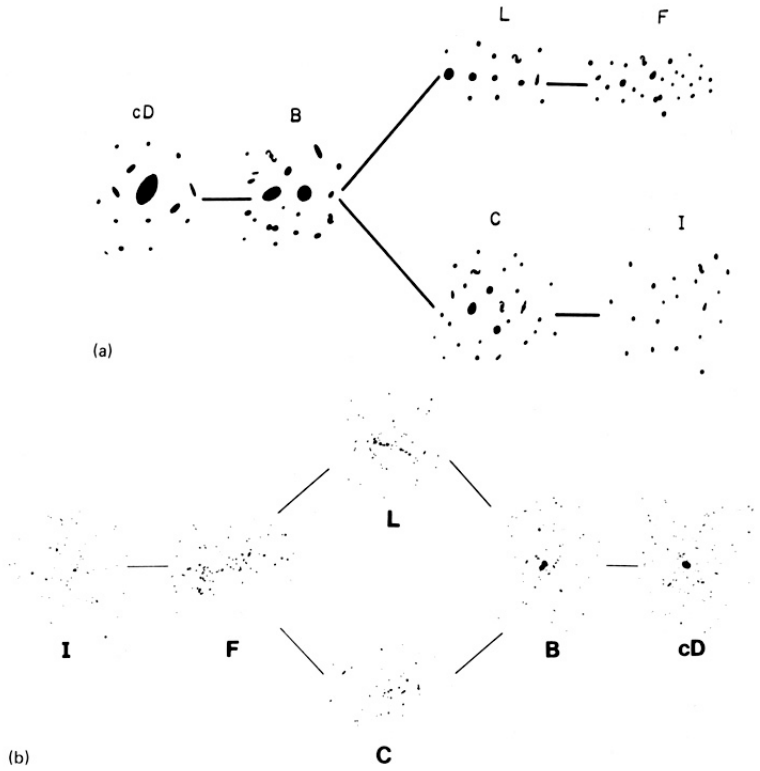

Figure 2.1: (a) The Rood-Sastry cluster classification scheme. (b) The revised Rood-Sastry classes. Taken from the book "X-ray Emission from Clusters of Galaxies" (Sarazin 1988).

To classify a cluster, not only the distribution of galaxies must be taken into account, but also their nature. Regular clusters tend to have a pronounced central concentration of galaxies, in which the vast majority are ellipticals or lenticulars. In the other hand, irregular clusters are generally spiral-rich and have low central concentration. The linear sequence of cluster classes relating to population profile suggests that this hierarchy has all to do with the dynamical status of the cluster. That is, irregular clusters exist in a perturbed state, which must be related to an early stage of structure formation. Given enough time, the system tends to get relaxed and increase its richness, forming cD, B, C and L clusters.

Although practical, the old classification schemes were too dependent on observational features (eg., galaxy distribution and its apparent properties) rather than on the underlying physical characteristics of the ICM. The unprecedented sensitivity and angular resolution delivered by the Chandra and XMM-Newton X-ray observatories (Weisskopf et al. 2002; Paerels and Kahn 2003), together with the advent of multi-wavelength observations, allowed for the development of a more physically-motivated framework. Today, clusters are primarily classified from their ICM properties, such as total mass, the presence of cool cores or dynamical disturbances, which correlate with their evolutionary stage and merger history.

A cool-core cluster is characterized by a dense, low-temperature central region and

a very pronounced surface brightness peak (usually coincident with the BCG), while a non-cool core cluster tipically has a roughly flat central temperature profile, high central entropy, high central cooling time, and a more disturbed X-ray morphology. Figure 2.2 shows the surface brightness distribution for a cool-core and a non-cool-core cluster. Approximately one-third of all galaxy clusters are classified as cool-core systems. The ICM in such clusters reaches temperatures of tens of millions of Kelvin, emitting X-rays primarily via thermal bremsstrahlung. Central gas densities are sufficiently high to enhance X-ray emissivity and trigger subsonic cooling flows toward the BCG, which, if left unchecked, would lead to runaway cooling, due to loss of pressure support, and consequently excessive star formation. For this reason, the earliest model assumed that clusters were spherical, isolated systems that would naturally tend to form cool cores (Fabian 1994). However, with the increased spatial resolution of Chandra and the high spectral resolution of XMM-Newton, observations detect much less cold gas and star formation than initially predicted, leading to the so-called "cooling flow problem" (Fabian 2003). Many sources of central heating were considered to explain the discrepancy between theory and observations, but most were showed to be neglible or simply not dominant (eg., heat flow from thermal conduction). The finding of several radio sources in the cores of galaxy clusters, since its discovery by Mills (1960) and van den Bergh (1961), suggested that the dominant heating source could be related to AGN feedback: energy injected by the central supermassive black hole through jets, shocks, or turbulence heats the surrounding gas, thereby regulating the cooling flow. This self-regulating mechanism may also enhance star formation in the BCG, provided the central gas reaches the right thermodynamic conditions for condensation.

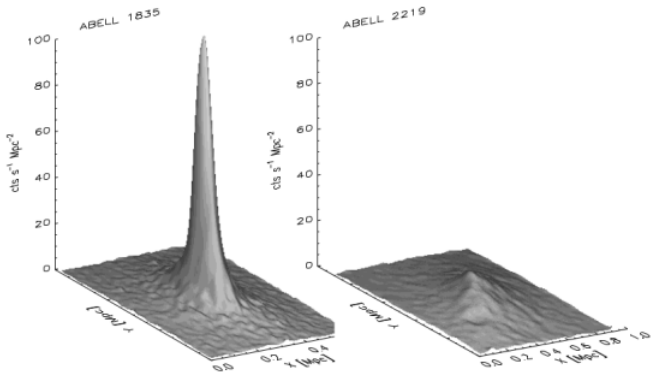

Figure 2.2: Comparison of the X-ray surface brightness distribution of a cool-core (left) and a non-cool-core (right) cluster. Source: Hlavacek-Larrondo et al. (2015).

As we are going to explore in the next section, the X-ray emission from the ICM is proportional to the squared gas density. Therefore, a high central cuspiness in the surface brightness is related to a high-density, low-entropy zone in the core of galaxy clusters. Subsequent studies have shown that the fraction of cool-core clusters remains

approximately constant up to $z \sim 1.4$, suggesting that cooling can efficiently sustain a low central entropy floor over several gigayears (Santos et al. 2008). In a recent work, Lehle et al. (2024) explored the properties of galaxy clusters from the cosmological simulation Ilustris-TNG (Nelson et al. 2019), finding that the fraction of cool-core and non-cool-core clusters can vary strongly with redshift and halo mass depending on the chosen classification criteria (eg., central cooling time, central entropy, slope of the density profile, concentration etc). In all considered criteria, the distribution of ICM properties appeared to be unimodal across the sample, suggesting that the presence or absence of a cool core does not define physically distinct classes, but rather represent two extreme cases of a continuous distribution of central ICM properties.

2.2 The intracluster medium

As previously mentioned, the majority of the baryonic content in galaxy clusters resides in the form of hot gas that permeates the space between galaxies. This highly ionized plasma reaches X-ray-emitting temperatures of millions of Kelvin as kinetic energy is converted into thermal energy through processes such as adiabatic compression and shock heating during the cluster's virialization (Kravtsov and Borgani 2012). These conditions give rise to a diffuse X-ray emission, with a continuum dominated by thermal bremsstrahlung (also known as free-free emission), which comes from the Coulomb interactions between free electrons and the electric fields of ionized atoms in the hot plasma. Since the gas is collisional and the gravitational potential is dominated by dark matter, this extended X-ray emission can be used to trace the cluster's total mass under (the assumption of hydrostatical equilibrium). It also allows the study of dynamical phenomena in the ICM, such as cooling flows, cold fronts, shock fronts, and even signatures of non-thermal processes in the cluster cores. We now proceed to discuss in more details the main physical and observational properties of the ICM.

2.2.1 Bremsstrahlung emission

The full description of the bremsstrahlung emission involves quantum effects, but the classical treatment tends to be a good enough approximation for our astrophysical context. Let us begin considering the interaction between a single electron and an ion.

Figure 2.3 shows the electron interacting with the Coulomb field of an ion positioned at $x = 0$, moving in a straight line until it suffers a slight deflection and reaches a fixed trajectory parallel to line OC. Let b be the minimum distance (impact parameter) between the electron and the ion, and v_e the velocity of the electron. It is easy to see that the electron experiences a force from the ion during a a short finite time interval. During this time, the electron is accelerated by the electric field E, acquiring a variable velocity,

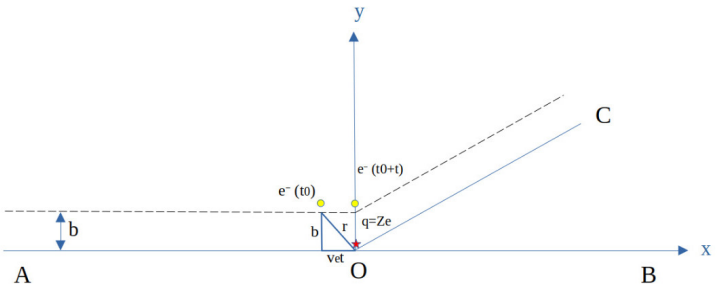

Figure 2.3: Electron interacting with the Coulomb field of an ion.

which causes the bremsstrahlung radiation. As a crude approximation, we consider that the acceleration is constant during the interaction time t, the distance r between the electron and the ion is

$$r = \left[b^2 + (v_e t)^2\right]^{1/2}. \tag{2.1}$$

Considering that the electron moves along the x-axis, we have

$$\cos\theta = \frac{v_e t}{r} \Rightarrow E_x = E\cos\theta = \frac{E v_e t}{r}, \tag{2.2}$$

$$\sin\theta = \frac{b}{r} \Rightarrow E_y = E\sin\theta = \frac{Eb}{r}. \tag{2.3}$$

The total acceleration experienced by the electron is

$$\vec{a} = \frac{e\vec{E}}{m_e}, \tag{2.4}$$

where m_e and e are the mass and the charge of the electron, respectively. The electric field produced by an ion with charge Ze is given by

$$\vec{E} = \frac{Ze\vec{r}}{4\pi\epsilon_0 r^3}. \tag{2.5}$$

Splitting the acceleration into components parallel and perpendicular to the trajectory (x and y directions, respectively), we get

$$a_x = -\frac{eE_x}{m_e} = \frac{Ze^2 v_e t}{4\pi\epsilon_0 m_e \left[b^2 + (v_e t)^2\right]^{3/2}}, \tag{2.6}$$

$$a_y = -\frac{eE_y}{m_e} = \frac{Ze^2 b}{4\pi\epsilon_0 m_e \left[b^2 + (v_e t)^2\right]^{3/2}}. \tag{2.7}$$

In the next steps, we want to relate the acceleration to the intensity spectrum, so we must first take the Fourier transform of the accelerations to obtain the spectral compo-

nents, that is

$$\hat{a}_x(\omega) = \int_{-\infty}^{\infty} \frac{Ze^2 v_e t}{4\pi\epsilon_0 m_e \left[b^2 + (v_e t)^2\right]^{3/2}} e^{i\omega t}\, dt, \tag{2.8}$$

$$\hat{a}_y(\omega) = \int_{-\infty}^{\infty} \frac{Ze^2 b}{4\pi\epsilon_0 m_e \left[b^2 + (v_e t)^2\right]^{3/2}} e^{i\omega t}\, dt. \tag{2.9}$$

Using $u = v_e t/b$, the integral becomes

$$\hat{a}_x(\omega) = \frac{Ze^2}{4\pi\epsilon_0 m_e v_e b} \int_{-\infty}^{\infty} \frac{u e^{i\omega b u/v_e}}{(1+u^2)^{3/2}}\, du, \tag{2.10}$$

$$\hat{a}_y(\omega) = \frac{Ze^2}{4\pi\epsilon_0 m_e v_e b} \int_{-\infty}^{\infty} \frac{e^{i\omega b u/v_e}}{(1+u^2)^{3/2}}\, du. \tag{2.11}$$

According to Larmor's formula, the power of the emitted radiation is proportional to the particle's accelaration. Considering we have the acceleration components in the frequency domain, the intensity spectrum is given by

$$I(\omega) = \frac{e^2}{6\pi^2\epsilon_0 c^3} \left(|\hat{a}_x(\omega)|^2 + |\hat{a}_y(\omega)|^2\right). \tag{2.12}$$

To solve the integral terms, we use the modified Bessel functions of the second kind K_n through the identity $\int_{-\infty}^{+\infty} e^{iuX}/(u^2+X^2)^k\ du = \sqrt{\pi}/\Gamma(k)\ (1/2X)^{k-1/2} K_{k-1/2}(X)$. In our case, $X = \omega b/v_e$. In the case of Equation 2.11, $k = 3/2$, leading to $2XK_1(X)$. For Equation 2.10, there is a multiplying u term in the integrand, which is just $\frac{1}{i}\frac{\partial}{\partial X}$ applied to the basic integral, so we can use the recurrence relation $\frac{d}{dX}[X^k K_k(X)] = -X^k K_{k-1}(X)$, leading to $2XK_0(X)$. Therefore, Equation 2.12 becomes

$$I(\omega) = \frac{Z^2 e^6 \omega^2}{96\pi^4 \epsilon_0^3 c^3 m_e^2 v_e^2 b^2} \left[K_0^2\left(\frac{\omega b}{v_e}\right) + K_1^2\left(\frac{\omega b}{v_e}\right)\right], \tag{2.13}$$

where $K_0(X)$ and $K_1(X)$ have the following limits

$$\begin{aligned}
K_0(X) &\to -\ln X, \quad \text{for } X \ll 1,\\
K_1(X) &\to \frac{1}{X},\\
K_0(X) &\to \sqrt{\frac{\pi}{2X}} e^{-X}, \quad \text{for } X \gg 1,\\
K_1(X) &\to \sqrt{\frac{\pi}{2X}} e^{-X}.
\end{aligned}$$

For small frequencies $X = \omega b/v_e \ll 1$, $I(\omega)$ is approximately constant: $I(\omega) = Z^2 e^6/(12\pi^3\epsilon_0^3 c^3 m_e^2 v_e^2 b^2) = \text{cte}$. For large frequencies, it decays exponentially. Therefore, $\omega = v_e/b$ is the characteristic frequency that sets the exponential cutoff for the

bremsstrahlung spectrum.

Let us now consider the interaction between the electron and a set of particles at thermal equilibrium. To compute the total spectrum, we must integrate over all impact parameters b. Considering a medium with a number density of ions n_i, the number of interactions (or encountered ions) for a given b as the electron moves a distance ds is $N = 2\pi n_i b\, ds\, db$. Therefore, the number of encounters per second is

$$\frac{dN}{dt} = 2\pi n_i \frac{ds}{dt}\, db = 2\pi n_i v_e b\, db. \tag{2.14}$$

Thus:

$$I_T(\omega, v_e) = \int_{b_{\min}}^{b_{\max}} I(\omega, v_e, b)\, 2\pi n_i v_e b\, db. \tag{2.15}$$

This gives:

$$I_T(\omega, v_e) = \frac{Z^2 e^6 n_i}{12\pi^3 \epsilon_0^3 c^3 m_e^2 v_e} \ln\left(\frac{b_{\max}}{b_{\min}}\right). \tag{2.16}$$

The choice for b_{max} and b_{min} depends on some previous knowledge on the regime of frequencies. A general choice would be $b_{max} = v_e/\omega$, which corresponds to the exponential cutoff limit, and $b_{min} = Ze^2/m_e v_e^2$ from conservation of energy. To find the emissivity of the thermal bremsstrahlung for a plasma of electrons, we average over a distribution of velocities $P(v_e)$ given by the Maxwell-Boltzmann statistics,

$$P(v_e) = 4\pi n_e \left(\frac{m_e}{2\pi k_B T}\right)^{3/2} v_e^2 e^{-m_e v_e^2/2k_B T}, \tag{2.17}$$

where n_e is the number density of electrons, k_B is the Boltzmann constant and T is the average temperature of the gas of electrons. The low-frequency bremsstrahlung emissivity is then

$$\epsilon(\nu) = \int_{v_{\min}}^{\infty} I_T(\nu, v_e) P(v_e)\, dv_e, \tag{2.18}$$

where $\nu = \omega/2\pi$. Substituting and evaluating, we arrive at

$$\epsilon(\nu, T) = \frac{Z^2 e^6 n_i n_e}{12\pi^3 \epsilon_0^3 c^3 m_e^2} \left(\frac{\pi m_e}{6 k_B T}\right)^{1/2} g(\nu, T) e^{-h\nu/k_B T}, \tag{2.19}$$

where we considered $m_e v_{min}/2 \sim h\nu$ (h being the Planck constant), and, as a good approximation, substituted $\ln(b_{max}/b_{min})$ for the so-called Gaunt factor $g(\nu, T)$, which depends on the band of frequencies of the emission. Naturally, some degree of self-absorption happens in a plasma in thermal equilibrium, as emitted photons are reabsorbed by free electrons. The thermal free-free absorption coefficient μ_{ff} (Equation 2.19 over a planckian) is a strong function of frequency and temperature. At high frequencies ($h\nu >> k_B T$), the exponential term vanishes and μ_{ff} becomes very small, making the plasma optically thin. At low frequencies ($h\nu << k_B T$), we can use the Rayleigh-Jeans approximation to

find that $\mu_{ff} \propto T^{-3/2} n_i n_e \nu^{-2}$, although still negligible in the X-ray regime of the ICM. Nevertheless, when modeling the observed X-ray spectrum of the ICM, photoelectric absorption by neutral hydrogen in the Milky Way significantly affects the soft portion of the spectrum, and therefore, one must include information on the foreground hydrogen column density N_H in order for the intrinsic emission to be recovered.

2.2.2 Number densities and mean molecular weight

As we just discussed, the emission in the ICM comes primarily from interactions between electrons and ions. The hot diffuse plasma is assumed to be in ionization equilibrium, since ionization and recombination timescales are shorter than any dynamical timescales in the cluster. The ionization state of the plasma is taken to be exclusively dependent on the electron temperature, as most of the electrons comes from the hydrogen (H) and helium (He) atoms. For solar abundances, neglecting heavier elements for simplicity, the H and He mass fractions are $X \approx 0.71$, $Y \approx 0.29$, respectively (Anders and Grevesse 1989). From this, we can write the number densities of each component as $n_H = \rho X / m_p$, $n_{He} = \rho Y / 4 m_p$, where ρ is the density of the gas, m_p is the proton mass. For a fully ionized plasma, only ions and electrons contribute to the total number density ($n = n_e + n_i$). Considering how much protons and electrons each component contributes, we can combine these equations to find the mean molecular weight μ. Each hydrogen atom provides one proton and one electron, while each helium atom provides one ion and two electrons, therefore

$$\mu \equiv \frac{\rho}{m_p(n_e + n_i)} = \frac{\rho}{m_p}[(n_H + 2n_{He}) + (n_H + n_{He})]^{-1} = \left(2X + \frac{3Y}{4}\right)^{-1} \approx 0.6. \quad (2.20)$$

It is also useful to find the ratio between the total number density and the electron density,

$$\frac{n}{n_e} = \frac{2n_H + 3n_{He}}{n_H + 2n_{He}} = \frac{2X + 3Y/4}{X + Y/2} \approx 1.92. \quad (2.21)$$

And finally, we calculate the ionization factor to relate the number densities between protons and electrons,

$$\frac{n_e}{n_p} = \frac{n_H + 2n_{He}}{n_H} = 1 + \frac{Y}{2X} \approx 1.2. \quad (2.22)$$

2.2.3 Thermodynamic properties

Given the observational challenges in fully characterizing the thermodynamic state of the ICM and the absence of a well-defined equation of state, it is practical to adopt

observables that scale with n_e, since the X-ray emission is highly sensitive to it. The first such quantity is the pseudo-entropy, defined as

$$K \equiv k_B T n_e^{-2/3}. \tag{2.23}$$

Then, we define the pseudo-pressure as

$$P \equiv n k_B T = 1.92 n_e k_B T, \tag{2.24}$$

where we used the factor calculated in 2.21. To quantify the timescale of radiative cooling, we define the so-called cooling time as the ratio between the thermal energy density, and the emissivity, giving

$$t_c \equiv \frac{u}{\epsilon} = \frac{(3/2) n k_B T}{n_e^2 \Lambda(T, Z)} = \frac{3P}{2 n_e^2 \Lambda(T, Z)}, \tag{2.25}$$

where $\Lambda(T, Z)$ is the so-called cooling function, which depends on the gas temperature T and metallicity Z. To evaluate how dominant radiative cooling in a certain region of the ICM, the cooling time is often compared to some dynamical timescale of the cluster. The most common choice is the free-fall time $t_{\rm ff}$, which is defined as the time required for a gas parcel to collapse under gravity in the absence of pressure support,

$$t_{\rm ff} = \sqrt{\frac{2r}{g}}, \tag{2.26}$$

where g is the gravitational acceleration at distance r. The ratio $t_{\rm ff}/t_c$ at each radius from the cluster's center gives us information on how prone that region is to thermal instabilities, as we are going to further discuss in Section 2.4.

2.2.4 Projection on the sky

The observed surface brightness $S(r)$ corresponds to the emissivity ϵ projected on the sky. As previously mentioned, The X-ray emission in galaxy clusters comes from the hot gas in the ICM, in which the dominant emission process is bremsstrahlung and, therefore, is proportional to the squared electron number density. The bolometric emissivity is then

$$\epsilon(r) = \Lambda(T, Z) n_e^2(r), \tag{2.27}$$

We want to be able to relate the emissivity (which depends on the density in the 3D space) to its projection on the sky, given by $S(r)$. We can do this with the Abel transform assuming spherical symmetry. Generally, $S(b)$ represents the projection of a circularly symmetric emission function, which is $\epsilon(r)$, along a set of parallel lines of sight at a distance b from the origin. In the schematic illustration of Figure 2.4, the observer

looks along a line parallel to the x axis, seeing the integral of the emission function along the line of sight.

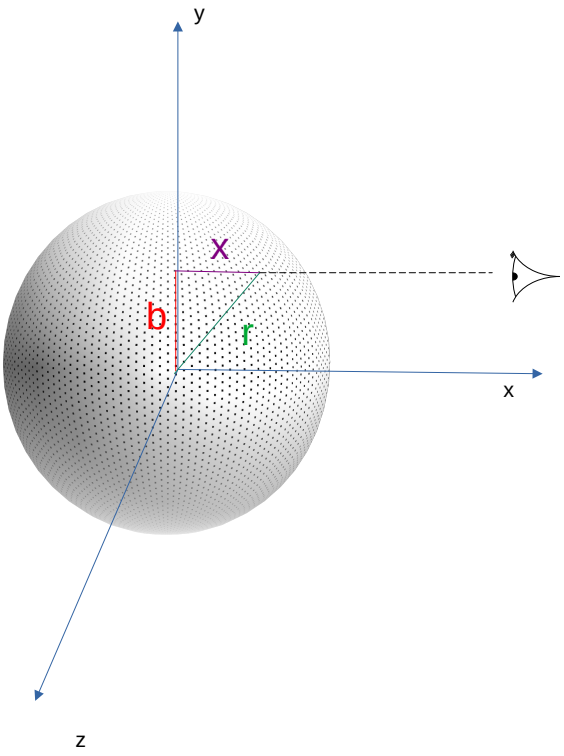

Figure 2.4: Schematic representation of the projection geometry for a spherically symmetric emissivity profile. b is the projected distance from the structure's center, x is the coordinate along the line of sight, while $r = \sqrt{b^2 + x^2}$ is the 3D radius.

For the optically thin hot ICM, the emission corresponds to the line of sight integral of the emissivity

$$S(b) = \int_{-\infty}^{+\infty} \epsilon(r)\, dx. \tag{2.28}$$

Making the substitutions $x = \sqrt{r^2 - b^2}$, $dx = r\, dr/\sqrt{r^2 - b^2}$ and considering the symmetry of the function, we get

$$S(b) = 2 \int_{b}^{+\infty} \frac{\epsilon(r) r}{\sqrt{r^2 - b^2}} dr. \tag{2.29}$$

We can conveniently fit the surface brightness using a beta-model, which assumes that the gas density distribution follows the King approximation to a self gravitating isothermal sphere. The density is then given by

$$n(r) \equiv n_0 \left[1 + \left(\frac{r}{r_c}\right)^2\right]^{-3\beta/2}, \tag{2.30}$$

where r_c is a scale radius, typically defining the cluster's core, n_0 is the correspondent core density and $\beta \equiv \mu m_p \sigma_r^2 / kT$ is a parameter that scales with the one-dimensional velocity dispersion of the member galaxies, σ_r, and with the gas temperature, kT. Relating 2.27, 2.29 and 2.30 gives

$$S(b) = 2n_0^2 \Lambda(T) \int_b^\infty \left[1 + \left(\frac{r}{r_c}\right)^2\right]^{-3\beta} \frac{r}{\sqrt{r^2 - b^2}} dr, \tag{2.31}$$

integrating, we get

$$S(b) = \sqrt{\pi} n_0^2 \Lambda(T) r_c \left[1 + \left(\frac{b}{r_c}\right)^2\right]^{0.5-3\beta} \frac{\Gamma(3\beta - 0.5)}{\Gamma(3\beta)}. \tag{2.32}$$

Since the beta model for the surface brightness is

$$S(b) = S_0 \left[1 + \left(\frac{b}{r_c}\right)^2\right]^{0.5-3\beta}, \tag{2.33}$$

where $\Gamma(x)$ represents the gamma function. 2.32 gives a way to directly compute the core density,

$$n_0 = \left[\frac{S_0}{\sqrt{\pi} r_c \Lambda(T)} \frac{\Gamma(3\beta)}{\Gamma(3\beta - 0.5)}\right]^{1/2}. \tag{2.34}$$

2.2.5 Hydrostatic mass

If the cluster of galaxies is relaxed, we can make equilibrium considerations to estimate its total mass. Starting from the Euler's equation,

$$\frac{D\mathbf{u}}{Dt} = \nabla\phi + \frac{\nabla P}{\rho} \tag{2.35}$$

where ρ is the gas density, $\mathbf{u}$ is the flow velocity vector, $D/Dt = \partial/\partial t + (\mathbf{u} \cdot \nabla)$ is the material derivative, P is the pressure in the gas and ϕ is the total gravitational potential. If the gas is in hydrostatic equilibrium, $\mathbf{u} = 0$ and 2.35 reduces to

$$-\nabla\phi = \frac{1}{\rho} \nabla P. \tag{2.36}$$

While the cluster evolves, its potential tends to become more isotropic with time (assuming the absence of recent great interactions with other structures), which allows us to consider the potential as spherically symmetric.

$$-\frac{d\phi}{dr} = \frac{1}{\rho}\frac{dP}{dr}. \tag{2.37}$$

Since the gas is very hot and rarefied, we can treat it as approximately an ideal gas, so that

$$P = \frac{NkT}{V} = nKT, \tag{2.38}$$

where n is the number density, which relates to the gas density by

$$\rho = \mu m_H n, \tag{2.39}$$

where μ is the average molecular weight and m_H is the hydrogen mass. So 2.38 becomes

$$P = \frac{\rho kT}{\mu m_H}. \tag{2.40}$$

In the gravitational side, the radial derivative of the potential is

$$\frac{d\phi}{dr} = \frac{GM(r)}{r^2}, \tag{2.41}$$

where G is the gravitational constant and $M(r)$ is the enclosed mass at a radius r. Combining 2.37, 2.40 and 2.41, we obtain

$$-\frac{GM(r)}{r^2} = \frac{k}{\rho\mu m_H}\frac{d(\rho T)}{dr}. \tag{2.42}$$

Isolating M(r) and opening the total derivative, we have

$$M(r) = -\frac{k}{G\mu m_H}\frac{r^2}{\rho}\left[\frac{\partial(\rho T)}{\partial\rho}\frac{d\rho}{dr} + \frac{\partial(\rho T)}{\partial T}\frac{dT}{dr}\right], \tag{2.43}$$

$$M(r) = -\frac{k}{G\mu m_H}\frac{r^2}{\rho}\left[T\frac{d\rho}{dr} + \rho\frac{dT}{dr}\right], \tag{2.44}$$

Multiplying everything by $\frac{\rho T}{\rho T}$,

$$M(r) = -\frac{kT}{G\mu m_H} r\left[\frac{r}{\rho}\frac{d\rho}{dr} + \frac{r}{T}\frac{dT}{dr}\right], \tag{2.45}$$

Remembering that $\frac{dln(f)}{dln(x)} = \frac{x}{f}\frac{df}{dx}$, we can express 2.45 as

$$M(r) = -\frac{kT}{G\mu m_H} r\left[\frac{dln(\rho)}{dln(r)} + \frac{dln(T)}{dln(r)}\right], \tag{2.46}$$

which gives us a good estimate of the total cluster mass for a given scale radius.

2.3 Dynamical Activity

Various types of phenomena can make the structure of the ICM deviate from hydrostatical equilibrium: the AGN located in the BCG often injects large amounts of energy in the cluster's core, offsetting cooling, increasing turbulence and generating populations of non-thermal electrons in the medium. As clusters evolve, they undergo major merges with other clusters or, more often, capture smaller galaxy groups. These interactions perturb the gas through tidal forces, producing observable features in the ICM in the form of discontinuities. In this section, we examine the physical properties behind these dynamical events and their associated observational signatures.

2.3.1 AGN Feedback

The majority of cool core clusters harbour radio sources bubble-like structures filled with relativistic plasma as a consequence of the AGN feedback (Dunn and Fabian 2006), which observationally appears as X-ray cavities at various distances from the BCG. The propagation and expansion of these buoyant bubbles is one way of injecting energy into the central regions of the cluster, since it displaces gas, creates pressure waves and do PdV work, gradually converting the bubble's internal energy into thermal energy in the ICM (effervescent model). Another heating mechanism is associated to the creation of adiabatic acoustic waves by the AGN activity, which heats the ambient gas through viscous and conductive dissipation (acoustic model). Iqbal et al. (2023) found that both models can produce reasonable ICM thermodynamic profiles for typical AGN jet powers. Figure 2.5 shows the example of X-ray cavities in the Hydra A galaxy cluster and the HCG 62 compact group. The Hydra A image contains extended radio lobes that permeates a large-scale portion of the system and exihbit signs of surrounding shocks due to the bubble expansion in the ICM. In the HGC 62 image we can clearly see the disturbed inner radio lobes filling the X-ray cavities, while the outer lobes lacking associated X-ray cavities.

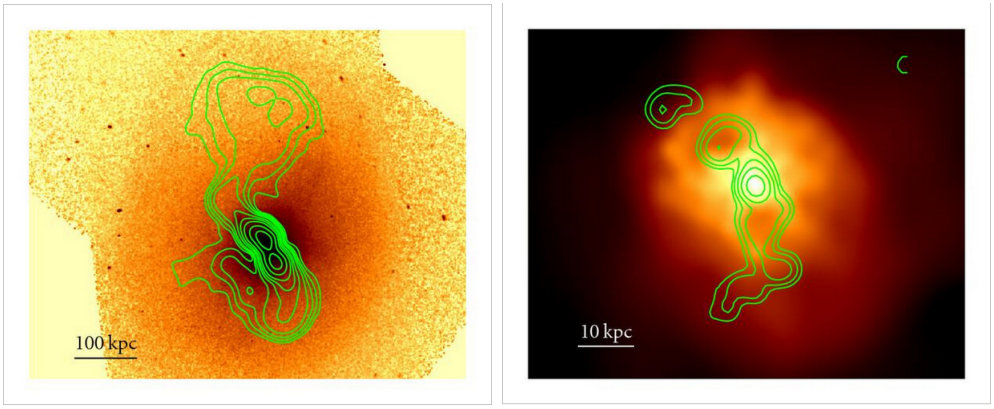

Figure 2.5: (left) 0.5-7.5 keV Chandra image of the galaxy cluster Hydra A (z=0.0538), green contours trace the 330 MHz radio emission. (right) 0.5-2 keV Chandra image of the compact group HCG 62 (z=0.0137) with 235 MHz GMRT contours. Source: Gitti et al. (2012).

The AGN energy input to the ICM can be estimated by calculating the energy that would be required to create the observed bubble (Dunn and Fabian 2006). Assuming that the expansion rate is low, then this corresponds to the bubble's internal energy plus the work done by the expanding material,

$$E_b = \frac{\gamma}{\gamma - 1} pV, \tag{2.47}$$

where γ is the mean adiabatic index of the fluid in the bubble ($\gamma = 4/3$ for a relativistic fluid), V is the bubble's volume and p is the thermal pressure of the surrounding gas in the ICM. Assumptions about the 3-dimensional shape of the bubble must be made. These shapes are generally parametrized with semimajor axes along and across the jet direction (R_I and R_w, respectivelly), thus the volume is given by

$$V = \frac{4\pi}{3} R_I {R_w}^2. \tag{2.48}$$

The age of the outburst that generated the bubble can be obtained by considering the timescale for a buoyancy propagation

$$t_{buoy} = R/c_s, \tag{2.49}$$

being c_s the medium speed of sound,

$$c_s = \sqrt{\frac{\gamma * k_b T}{\mu m_H}}, \tag{2.50}$$

where now we have $\gamma* = 5/3$ for a non-relativistic gas, since no strong shocks are observed in the surrounding gas, so it is assumed that the bubble is not expanding much faster than the local speed of sound. With these quantities, it is possible to estimate

the power of the bubble by simply dividing the estimated mean AGN power (given by Equation 2.47) by the outburst age (given by Equation 2.49)

$$P_{bubble} = \frac{4PV}{t_{buoy}}. \tag{2.51}$$

Dunn and Fabian (2006) showed there's a slight correlation between the bubble power and the cooling luminosity (Figure 2.6). The authors conclude that the clusters that fall above the $L_{cool} = P_{bubble}$ line host an AGN capable of inject sufficient energy into the ICM to offset all of the X-ray cooling.

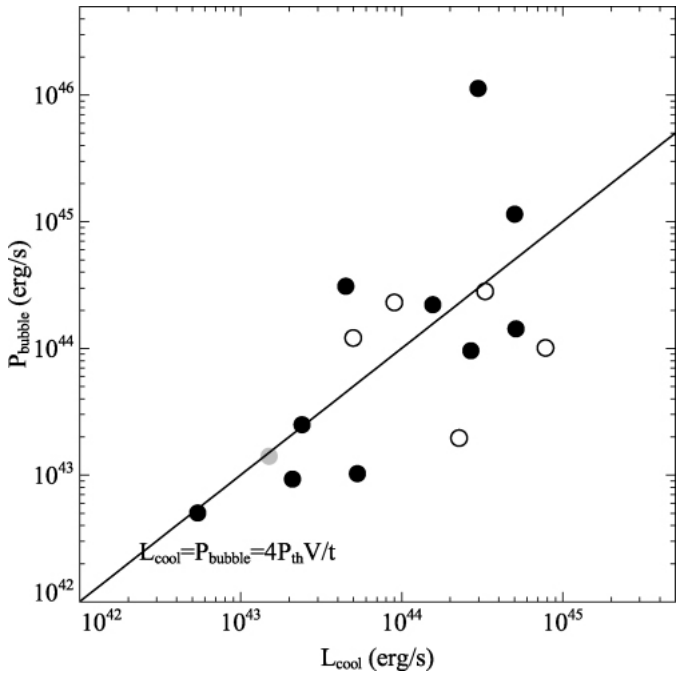

Figure 2.6: P_{bubble} vs L_{cool} plot for the sample analyzed in Dunn and Fabian (2006). Open circles correspond to clusters with bubbles without associated GHz emission.

2.3.2 Cold Fronts

Cold fronts are contact discontinuities in the gas produced by the motion of cooler, denser gas through a surrounding hotter atmosphere. They were first observed in the clusters Abell 2142 (Markevitch et al. 2000) and Abell 3667 (Vikhlinin et al. 2001). Their X-ray images are shown in Figure 2.7. The most notable feature is the clear sharp surface brightness edges in specific directions, marking the orientation of the cold fronts.

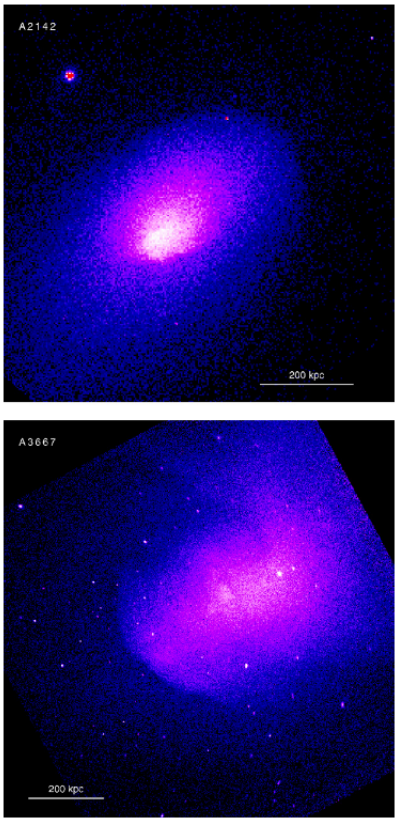

Figure 2.7: Upper: Chandra X-ray image of Abell 2142, two surface brightness edges are visible, an outer one to the northwest (contrast between blue and black), and an inner one to the south (contrast between purple and blue). Bottom: Chandra X-ray image of Abell 3667, with a very clear edge to the southeast. Source: Markevitch and Vikhlinin (2007)

A leading explanation for the existence of such features is that the cloud of denser gas represents the remnant of the cool cores from two subclusters that underwent a merger. At some moment after the point of minimum separation, the denser core regions would propagate through the surrounding shocked gas generated by the collision, therefore producing the observed discontinuities perpendicular to the direction of propagation. Sometimes, if the merger is supersonic a shock front is observed ahead (upstream) of the cold front, elevating the gas temperatures between the shock and cold fronts. While many cold fronts are successfully explained by this scenario (e.g., 1E 0657–5, A168), their presence in numerous non-merging clusters indicates that mergers are not the sole origin of these discontinuities. The additional mechanism for formation of cold fronts is related to perturbations (for instance, a minor, off-axis merger) that displaces the dense gas in a cool core from the deep gravitational potential, making it to oscillate around the cluster's center (ZuHone et al. 2013). This sloshing motion generates prominent spiral-shaped structures in the surface brightness distribution. Unlike merger-driven cold fronts, which arise from supersonic gas motions, sloshing produces cold fronts through subsonic gas displacements, often forming pairs in opposing directions. Spectral modeling from spatially resolved X-ray data allow

one to obtain important physical information to identify and characterize the nature of a cold front. Figure 2.8 show various profiles from a spatial sector that includes a surface brightness edge in the image of Abell 1795. First, we see from panel (a) a subtle discontinuity in the surface brightness profile, while the modeled X-ray temperature in panel (b) shows a sudden jump of temperature just beyond the edge, which is followed by a correspondent density jump in panel (c). Nevertheless, panel (d) shows that there is approximate pressure equilibrium across the discontinuity, which is a strong indication that the cold front is produced by sloshing-driven subsonic displacements of gas. Even though pressure is nearly continuous across the interface, the different slopes of the total mass profile in panel (e) indicates that, while the gas beyond the front is approximately at hydrostatic equilibrium, the gas inside the edge is not, since such discontinuity in the enclosed mass is unphysical.

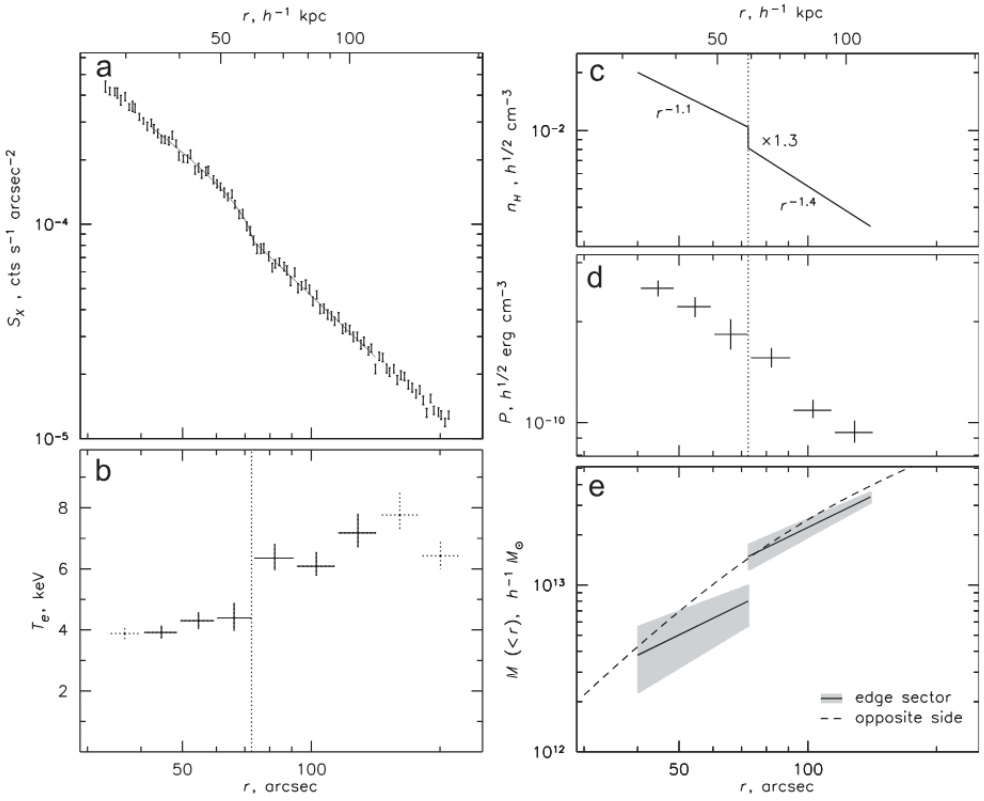

Figure 2.8: Profiles of a sector encompassing a cold front in the cluster A1795. (a) X-ray surface brightness. (b) Deprojected gas temperature profile. (c) Best fit density model, showing a jump of x1.3 at the discontinuity and change of slope. (d) Pseudo-pressure profile. (e) Enclosed total mass profile assuming hydrostatic equilibrium. Source: Markevitch et al. (2001).

Figure 2.9 shows a schematic representation of a body of denser gas surrounded by a uniform stationary flow. Zone 1 is where the gas stream is still undisturbed. At zone 0 (stagnation point), there is stagnation of the flow, that is, the velocity component along the axis of symmetry is zero, but the gas is then reaccelerated tangentially to the sides,

entangled by the magnetic field lines. Zone 2 marks the regions where a bowshock is expected to form from adiabatic compression of the gas.

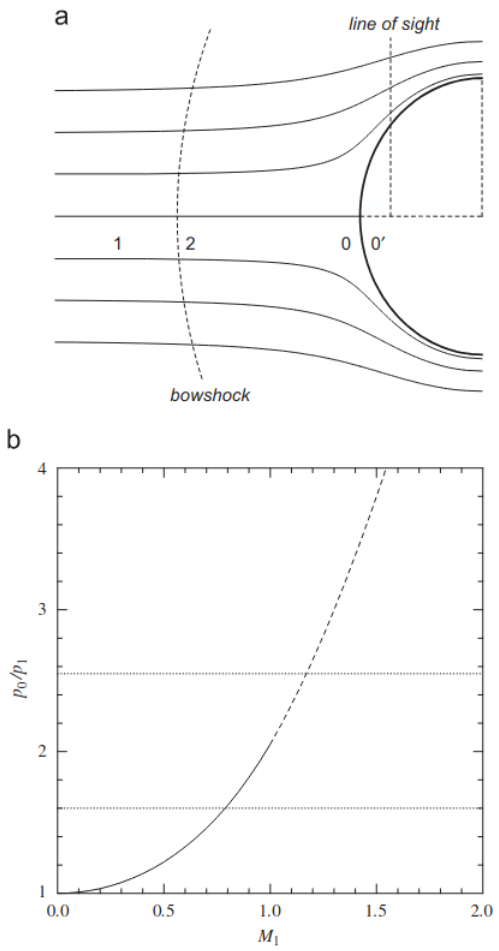

Figure 2.9: (a) Geometry of a flow after a spheroidal cold front. Zone 0 is the region near the stagnation point, zone 1 is in the undisturbed free stream, while zone 2 is the region past a potential bowshock and zone 0' is inside the front. (b) Ratio between pressures in zones 0 and 1 versus the Mach number in the free stream. Source: Vikhlinin et al. (2001).

As shown in Figure 2.8, the pressure increases as one goes from zone 1 to zone 0, while between zones 0 and 0', thermal pressure is approximately constant. The ratio of thermal pressures at zone 0 (stagnation point) and zone 1 free stream P_0/P_1 is proportional to the velocity of the gas motions. Therefore, one can use the following relation (Landau and Lifshitz 1959) to find the Mach number $\mathcal{M}$ (linear velocity over the medium sound speed) associated to the gas motion in the subsonic regime.

$$\mathcal{M} = \sqrt{\frac{2}{\gamma - 1}\left[\left(\frac{P_0}{P_1}\right)^{\frac{\gamma-1}{\gamma}} - 1\right]}, \tag{2.52}$$

where $\gamma = 5/3$ is the adiabatic index of the gas.

2.3.3 Shock Fronts

X-ray images of dynamically active galaxy clusters often reveal sharp discontinuities in the ICM, marked by abrupt jumps in density, temperature, and pressure across the edge. These features characterize the presence of the so-called shock fronts, and are typically created by supersonic motions of the gas, mainly due to mergers or AGN-induced jets and bubbles. Naturally, the shocked gas is hotter, denser and at higher pressure compared to the pre-shock region. Figure 2.10 shows the shock front in the merging cluster Abell 520, as well as the radial behaviour of temperature, surface brightness and density profiles across a narrow sector that includes the observed edge (Markevitch et al. 2005).

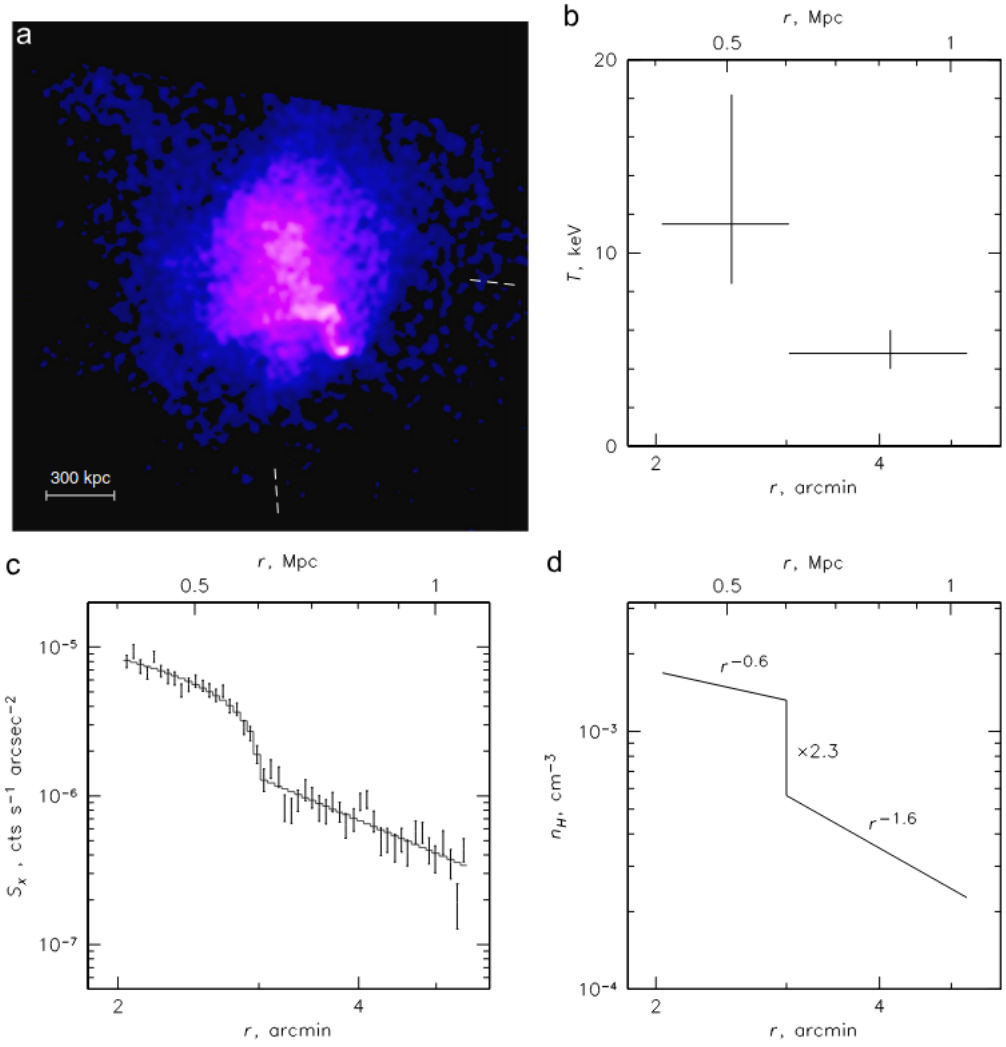

Figure 2.10: (a) Chandra X-ray image of Abell 520, containing a shock front to the southwest (bottom right). (b) Projected temperature profile across the shock. (c) Surface brightness profile across the shock. (d) Modeled density profile, with a x2.3 jump across the edge. Source: Markevitch et al. (2005).

2.4 The Cooling-Feedback cycle

Strong evidence supports the so called cooling–feedback model, in which radiative cooling and feedback from the central supermassive black hole (SMBH) mutually influence and constrain each other in a self-regulating manner (Dunn and Fabian 2006; Main et al. 2017; Calzadilla et al. 2024). Cavagnolo et al. (2009) noted the existence of a central entropy threshold in a statistically complete sample of clusters ($z < 0.3$) below which the star formation rate in the BCG is enhanced. Recently, Calzadilla et al. (2023) applied a multi-wavelength study to a Sunyaev-Zeldovich (SZ) selected sample of galaxy clusters ($0.3 < z < 1.7$) to show that this threshold persists throughout the redshift range of their sample, although only marginal evidence has been found for a evolution in the threshold. They also evaluate if this threshold can separate different populations based on the radio emission.

The authors characterized the thermodynamical properties of the ICM through the X-ray spectral analysis of the hot gas in the central region (under 10 kpc of the cluster's center), which allowed them to calculate the central entropy $K_{10\,kpc}$. To evaluate whether the ICM cooling is fueling star formation in the BCG, they performed a spectral energy distribution (SED) fitting using optical and IR spectroscopic data (GMOS and FORS2). The stellar continuum was modeled and subtracted and a linear Gaussian model was used to look for the presence of [O$_{\rm II}$] emission. The [O$_{\rm II}$] emission line luminosity is an indirect measure of the star formation rate, as it relates with the necessary photons produced by young stars to ionize the interstellar medium (Kennicutt 1998).

The radio analysis was intended to investigate the connection between ICM cooling and the synchrotron radiation produced by AGN jets, which are powered by SMBH accretion in the BCG. The radio observations (ATCA and RACS) were used to do a crossmatch and separate the objects in groups of radio detection/non-detection. The k-corrected 1.4 GHz rest-frame radio powers of the detection objects were calculated.

By dividing their sample in redshift bins, the paper evaluated the connection between $K_{10\,kpc}$, $L_{[\rm O_{II}]}$ and $L_{1.4\,\rm GHz}$. Figure 2.11 shows the $K_{10\,kpc}$ vs $L_{\rm H\alpha}$ or $L_{[\rm O_{II}]}$ plot in the different redshift bins. The left two panels are from the ACCEPT sample (for which there was Hα data available) (Cavagnolo et al. 2009). It is evident that the threshold significantly separate the regimes of detection and non-detection of [O$_{\rm II}$] (the separation is even better for the Hα data as it offers a more direct measure of the star formation).

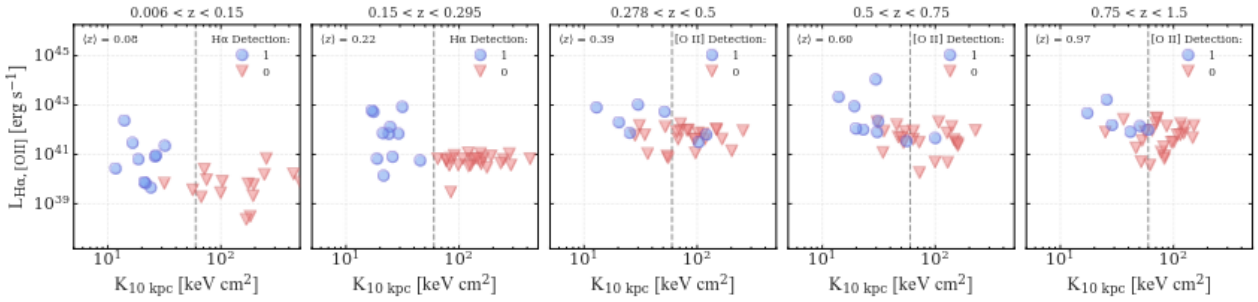

Figure 2.11: ($K_{10\,kpc}$) vs Hα or [O$_{\rm II}$] emission line luminosity separated by redshift bins. Vertical line marks the considered threshold of $K_{10\,kpc} = 60$ keV cm^2. Source: Calzadilla et al. (2023).

Figure 2.12 shows the central entropy $K_{10\,kpc}$ vs 1.4 GHz rest luminosity of the central radio source (νL_ν) plot in different redshift bins. In this case it is not possible to identify a correlation in the redshift range of the detection group (0.28-1.5). The absence of a clear radio dichotomy at higher redshifts associated with the central entropy could be either due to an evolution of the threshold, meaning that in early times cooling-feedback cycle was not tightly-regulated or it could also be explained by a competing source of AGN fueling, for instance mergers and interactions).

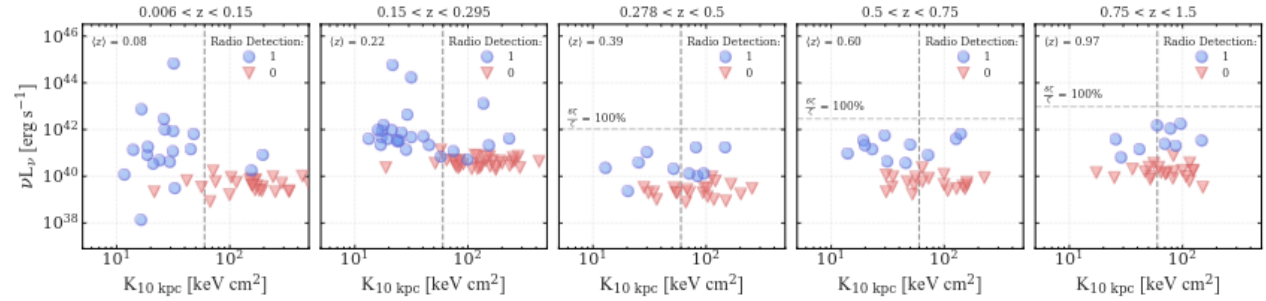

Figure 2.12: ($K_{10\,kpc}$) vs (νL_ν) separated by redshift bins. Source: Calzadilla et al. (2023).

To further explore qualitative aspects of the physical relations between AGN feedback, ICM cooling and star formation in the BCG, we will briefly present the framework developed by Voit et al. (2017) for feedback-regulated precipitation in cluster cores. Generally, the first cycle is preceded by a period of unopposed, highly homogeneous cooling, promoting thermal instabilities that will lead to condensation of the central low-entropy gas and eventually the first outburst event. Over the next few hundred Myr, the energy injected in the ICM will inflate bubbles, increase the central entropy and uplift cold gas to larger radii. At this phase, heating and gas mixing creates a roughly isentropic core, while the outer region tends to maintain a power-law of $\mathrm{d}\ln(K)/\mathrm{d}\ln(\mathrm{r}) \approx 1$. This scheme is showed in Figure 2.13. In the isentropic zone, buoyancy damping is ineffective, allowing efficient condensation to boost star formation and feed the SMBH. In the power-law region,

buoyancy suppress thermal instabilities, preventing large-scale condensation. However, cold patches adiabatically uplifted by the outflows are prone to condense and eventually fall back to the center, ensuring a steadier fuel to the SMBH. Therefore, once this two-phase structure is established, a stable self-regulated cycle persists for a prolonged period, maintaining a minimum $t_{\rm cool}/t_{\rm ff} \approx 10$ in the isentropic core.

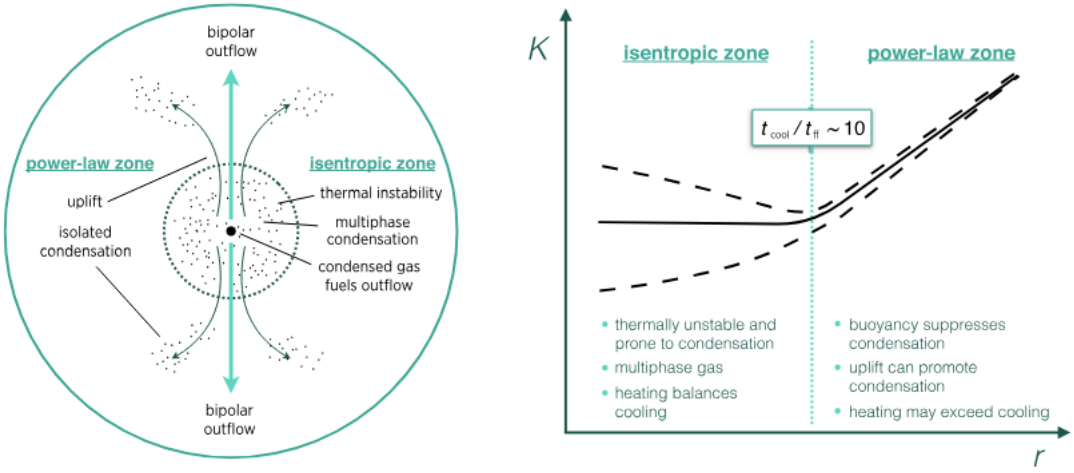

Figure 2.13: (left) Schematic representation of the two-phase entropy structure in a cluster's core. (right) Correspondent entropy profile with the isentropic and power-law zones. Source: Voit et al. (2017).

Once the cold gas reservoir is depleted, the AGN shuts down and $t_{\rm cool}/t_{\rm ff}$ continuously falls until the conditions for runaway cooling are met again, promoting precipitation in a period of $\sim t_{\rm cool}$ and restarting the loop. Naturally, the subsequent cycles are not identical to the first one, since there are residual inhomogeneities that increase the efficiency of condensation. Therefore, the second outburst leads to a larger reservoir of cold gas and a higher $t_{\rm cool}/t_{\rm ff}$ floor, making the self-regulated cycle stable for up to multiple Gyr. Figure 2.14 shows the time evolution of various quantities in the idealized hydrodynamical simulation of a cluster's core done by Li et al. (2015), which includes radiative cooling, AGN feedback, star formation and stellar feedback. First, it is important to acknowledge the highly idealized nature of this simulated core, as it is not the result of a cosmological hydrodynamical simulation. Consequently, certain properties may appear overly symmetric or lack the complexity typically observed in more realistic cluster environments. With this said, the qualitative behaviour of the parameters shown in Figure 2.14 is still a great representation of the presented feedback-regulated precipitation model. The top panel, shows that the local minima of $\min(t_{\rm cool}/t_{\rm ff})$ happens just prior to each outburst event, which, as discussed earlier, is favored by unopposed cooling, that brings material to the vicinity of the SMBH. After the outflows, the buildup of cold gas, and consequently the star formation rate in the BCG, rapidly peaks in a few dozen Myr. On the other hand, the timescale for $\min(t_{\rm cool}/t_{\rm ff})$ to stabilize is considerably larger, since the energy injected by outflows and the generate turbulence must gradually reheat and redistribute the gas,

increasing both the local cooling time and the effective entropy of the core before the system can approach equilibrium again, which also means to restore the well-structured isentropic and power-law zones.

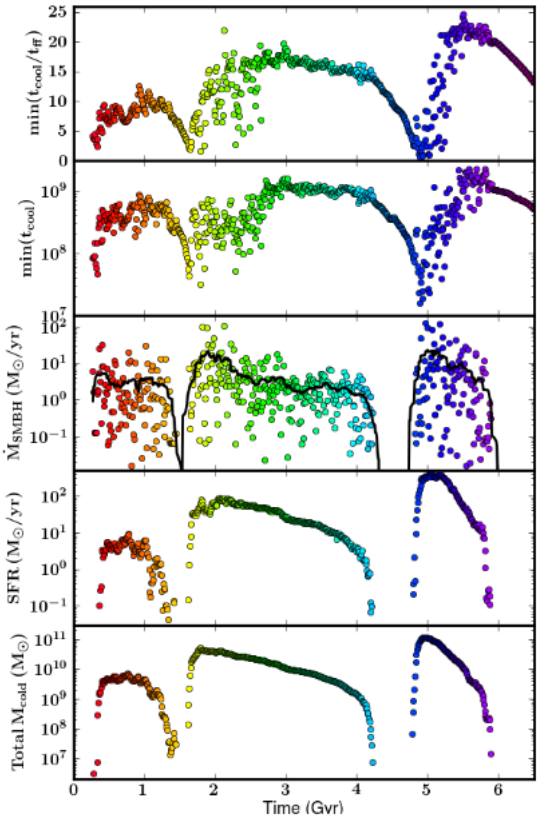

Figure 2.14: Time evolution of the minimum value of $t_{\rm cool}/t_{\rm ff}$, minimum cooling time $t_{\rm cool}$, SMBH accretion rate, star formation rate and total amount of cold gas (temperature below 10^5 K), respectively from upper to bottom panel. Each point is sparsed by 10 Myr; the color gradient indicates the passage of time. Source: Li et al. (2015)

Figure 2.15 shows the pseudo-entropy (Equation 2.23) distribution at each radius across multiple snapshots of the second cycle. From $t = 1.44$ Gyr to $t = 1.59$ Gyr, the AGN feedback shuts down after the cold fuel runs out, which in turn makes the central entropy and cooling time gradually decrease. The resulting flattening of the entropy gradient, dK/dr, creates favorable conditions for condensation to occur approximately at the boundary between the isentropic and the power-law zones, which eventually triggers the second outburst at $t = 1.64$ Gyr. The shades of orange across different radii represent the scatter of the entropy. We can see that the outflows introduce significant entropy inhomogeneities, that is, at each radius, a larger fraction of the gas deviates from the median entropy value. The upper scatter is generally associated to the high-entropy outflows, while the lower scatter is associated to the multiphase gas uplifted to larger radii.

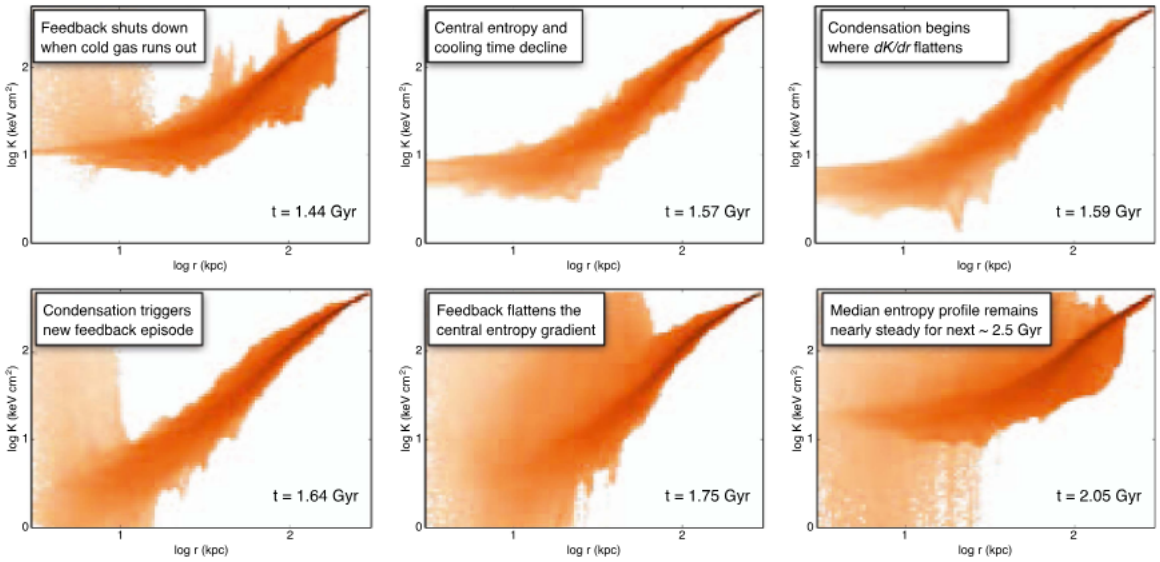

Figure 2.15: Snapshots of the pseudo-entropy distribution during the second cooling-feedback cycle in the cluster's core simulation of Li et al. (2015). Source: Voit et al. (2017).

2.5 Cosmology with galaxy clusters

The formation of groups and clusters of galaxies is closely related to the cosmological history of the universe. Table 2.2 shows the characteristic redshifts, temperatures, and times for fundamental events in early cosmic history. The early universe ($z > 3440$) was dominated by radiation, consisting of a hot plasma of ionized particles. As the universe expanded, the conditions of thermal equilibrium allowed the formation of Hydrogen and Helium nuclei. During the epoch of recombination, the universe was matter dominated, but the number density of free electrons dropped quickly as they were being captured to form neutral atoms, leading to a fast decrease of the ionization fraction. This process was succeeded by a photon decoupling, since the high energy free electrons were not around to scatter the light. From this point in time, these photons were free to travel in all directions, giving origin to the cosmic background radiation (Ryden 2016).

Table 2.2: Events in the early universe.

Event	Redshift	Temperature (K)	Time (Myr)
Radiation-matter equality	3570	$\sim$ 9700	0.047
Recombination	1370	$\sim$ 3700	0.24
Decoupling	1100	$\sim$ 3000	0.35
Last scattering	1100	$\sim$ 3000	0.35

Notes: Adapted from the book "Introduction to Cosmology" (Ryden 2016).

At the time of this last scattering, the energy density of dark matter was about 5 times

that of baryonic matter. Thus, the contribution to the gravitational potential in the universe was mostly from non-baryonic dark matter, which had not a perfectly homogeneous spatial distribution. These inhomogeneities provoke a position-varying gravitational potential. Consider a photon located in a potential well right after the last scatterring. Its signal will be redshifted, since the photon loses energy to escape from the well. In the same way, a photon positioned in a potential hill would gain energy from gravity and thus be blueshifted. This is the so-called Sachs-Wolfe effect (Sachs and Wolfe 1967), and one can see evidence of this dynamics through the temperature fluctuations in the Cosmic Microwave Background (CMB) radiation we observe today (Planck Collaboration et al. 2020b), as shown in Figure 2.16. After the removal of the Doppler dipole effect (created by the peculiar velocity of the Local Group), we see that CMB has a nearly isotropic spectrum, with temperature variations at large angular scales being about 30-100 μK across the sky. These fluctuations are very small considering CMB has an average temperature of 2.725 K, indicating that the early universe was quite smooth (Fixsen 2009).

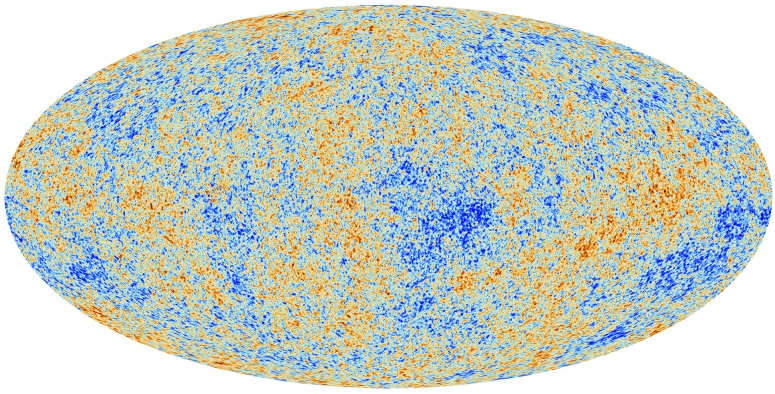

Figure 2.16: The anisotropies of the Cosmic microwave background (CMB) as observed by Planck Planck Collaboration et al. (2020a).

The small anisotropies in the early universe were propagated along with inflation, in a way that gravity amplificated the accumulation of matter in overdensed regions, leading further to the formation of galaxies and clusters. In other words, the small scale perturbations evolved to form the large structures we observe in today's universe. The present distribution of galaxies, groups and clusters in cosmological scales forms what is known as the *cosmic web*, disposed as multiple filaments separated by voids. The standard model of cosmology, called ΛCDM, has been extremely successful in explaining the growth of cosmic structure. The greek letter Λ comes from the term in Einstein's equation that describes the vacuum energy of free space, which is related to the accelerating expansion that gave origin to the initial density fluctuations. CDM stands for *Cold Dark Matter*, which is assumed to be a non-baryonic collisionless form of matter. A hot dark matter would be composed of ultrarelativistic travelling particles (maybe some type of neutrino), but wouldn't produce the observed clump patterns in cosmic structure. The theory have been successively tested by comparing cosmological simulations with observational data.

Figure 2.17 shows a comparison between the observed structure distribution and the one produced by the Millenium simulation (Springel et al. 2005). Both distributions share the same statistical properties. We can see in the upper small slice the Coma Wall (one of the largest superstrucutures known), note that there is also a similar wall formed by the mock galaxies. The capacity of the ΛCDM model to reproduce the observed universe in numerical simulations is really astonishing.

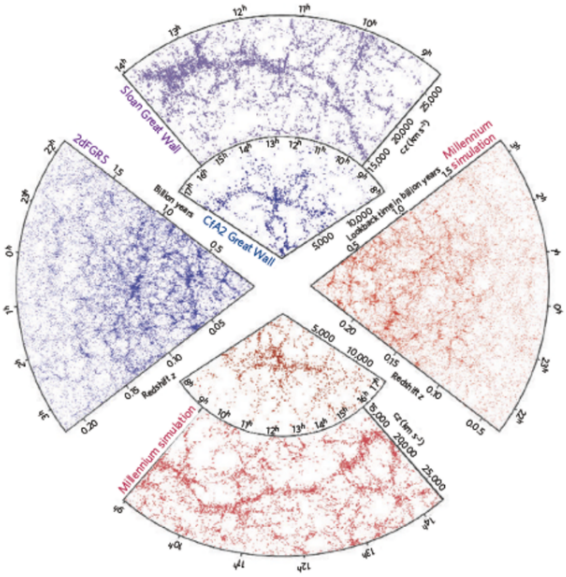

Figure 2.17: The galaxy distribution obtained from spectroscopic redshift surveys and from mock catalogues constructed from cosmological simulations. Source: Springel et al. (2006).

In the ΛCDM cosmological model, the shape of the matter power spectrum predicts a bottom-up formation scenario, where smaller structures form first and progressively merge into larger ones. On megaparsec scales, matter is distributed in a highly inhomogeneous web of clumps and voids. Galaxy clusters tend to form at the nodes of this cosmic web and are valuable tracers of the universe's large-scale structure formation history. One of the most important phenomena produced by the interaction between matter and radiation in the universe is the Sunyaev-Zel'dovich (SZ) effect, it arises from CMB photons suffering inverse-Compton scattering by free electrons in the hot ICM gas (Sunyaev and Zeldovich 1972; Sunyaev and Zeldovich 1980). Observationally, the blackbody spectrum of the CMB in the direction of the cluster is distorted, with an intensity decrement/increment at frequencies below/above $\sim$ 217 Ghz. Because the SZ spectral distortion depends on the integrated pressure along the line of sight, the surface brightness of the SZ signal is nearly independent of distance, with the selection function mainly limited by the cluster's mass, making it a powerful probe for the detection of massive high-redshift galaxy clusters (Carlstrom et al. 2002; Staniszewski et al. 2009).

The study of cluster properties provides crucial constraints on cosmological parameters, particularly the matter density of the Universe, and the non-linear regime of the

large-scale structure formation. For example, the abundance of clusters as a function of their mass, dN/dM, is sensitive to the matter density, Ω_m, and to the amplitude of matter fluctuations on a scale of $8\,h^{-1}\,\mathrm{Mpc}$, namely σ_8 (Press and Schechter 1974; Bahcall and Cen 1993). The distribution of clusters in redshift space, dN/dz, carries information on the dark energy equation-of-state parameter, w_0, through its dependence on the growth factor, D_z and the cosmological volume element dV/dz (Haiman et al. 2001). Additionally, due to the dominance of gravitational effects, it is expected that the gas mass fraction, $f_{\rm gas} = M_{\rm gas}/M_{\rm tot}$, in massive virialized clusters $\gtrsim r_{2500}$ resembles the cosmic baryon fraction, Ω_b/Ω_m (White et al. 1993; Sasaki 1996; Allen et al. 2002), and that it is fairly independent of redshift and halo mass, as predicted by the semi-analytical model of Tozzi and Norman (2001). The $f_{\rm gas}$ method has been used, in combination with external priors, to place constraints on Ω_m, Ω_Λ, and w (Allen et al. 2002; Ettori et al. 2009; Mantz et al. 2014; Mantz et al. 2022), providing independent evidence for cosmic acceleration.

The primary limitation of cluster counts and the $f_{\rm gas}$ method as cosmological probes is the accurate determination of cluster masses. Generally, estimating the total halo mass requires the use of observable proxies, such as the X-ray emission from the ICM, the weak lensing (WL) shear, or the SZ effect signal. The X-ray-derived mass typically relies on the assumptions of spherical symmetry and hydrostatic equilibrium (HSE) between the thermal gas and the gravitational potential, introducing a bias due to non-thermal pressure support from bulk motions, active galactic nuclei (AGN) feedback and turbulence, which can underestimate the total mass by tens of percent depending on the dynamical state of the gravitating material (Nagai et al. 2007; Lau et al. 2009). Many studies indicate that the hydrostatic mass bias is significantly reduced for derived masses at r_{2500}. This is supported by Mahdavi et al. (2008), who found excellent agreement between weak lensing and X-ray masses at this radius ($M_X/M_L = 1.03 \pm 0.07$) in a uniform sample of 18 clusters, being also consistent with the results of earlier works with hydrodynamical simulations (Evrard et al. 1996; Rasia et al. 2006). Moreover, several analytical corrections and calibrations have been proposed to systematically account for non-thermal components and recover true halo masses (Rasia et al. 2004; Nelson et al. 2012; von der Linden et al. 2014). However, this scenario becomes significantly more complex for dynamically active systems (e.g., those experiencing recent or ongoing merger events). Nelson et al. (2014) demonstrated through the analysis of 62 clusters from a high-resolution cosmological simulation that the hydrostatic bias in current/post-merger clusters can vary strongly with radius, becoming either highly positive or negative depending on the position of the infalling structure and making general mass correction schemes impractical. Additionally, an irreducible bias arises from gas acceleration components, which becomes non-negligible in unrelaxed systems, particularly in the high-redshift regime where mergers are more frequent. Even though the WL method is generally considered to be independent of dynamical assumptions,

since its signal is proportional to the projected potential of the system, breaking the mass-sheet degeneracy still requires the adoption of a density analytical profile, which can be unsuitable for merging clusters (Lee et al. 2023). Additionally, the SZ-derived masses also inherit dependence on the cluster's dynamical state through their calibration with X-ray observables.

Precise dynamical state classification is critical for cosmological applications, as only relaxed clusters provide sufficiently unbiased halo mass estimates. In the absence of high-quality spectroscopic data, the dynamical state of clusters may be inferred from the morphological regularity of the ICM X-ray emission. The pioneering work of Allen et al. (2002), which established some of the first cosmological constraints from $f_{\rm gas}$ measurements, selected relatively relaxed systems based on the sharpness of X-ray surface brightness peaks, isophote shapes, and isophote centroid variations, in addition to optical morphologies and gravitational lensing data, when available. Further studies Allen et al. (2004) and Allen et al. (2008) extended the samples to X-ray luminous clusters in the redshift range $\sim 0.05 < z <\sim 1$ - refining the selection criteria to include central cooling times and several other proxies for high-redshift systems with intermediate features. Many other works employed X-ray morphological parameters to trace substructures/inhomogenities in galaxy clusters (Jeltema et al. 2005; Hashimoto et al. 2007; Parekh et al. 2015; Zenteno et al. 2020; Yuan and Han 2020). This is a natural step, since the morphology parameters are directly calculated from the X-ray imaging, without requiring spectral modeling to derive the physical properties of the ICM. This supports an automated approach to classify the increasing number of intermediate and high-redshift clusters currently detected via SZ and X-ray techniques prior to the upcoming powerful spectro-imagers such as AXIS (https://axis.umd.edu/) (Russell et al. 2024) and NewAthena (https://www.cosmos.esa.int/web/athena) in the next decade, and also by the current large scale surveys such as J-PAS (www.j-pas.org/) and LSST (www.lsst.org/). In the following chapter, we are going to present the currently available observations of SPT2215 and the main results found by previous works.

Chapter 3

SPT2215

SPT2215 was first discovered in radio as one of the most massive known clusters at $z > 1$ through the SPTpol Extended Cluster Survey (SPT-ECS) (Bleem et al. 2020) using the SPTpol receiver of the 10 m South Pole Telescope. SPT-ECS detected several clusters from their thermal SZ signal as high-significance decrements in the 150 GHz and 95 GHz SPT maps. Some relevant multiwavelength follow-up observations of SPT2215 has been made since its discovery, such as ten Chandra X-ray observations totaling 204.5 ks of exposure time, as detailed in Table 4.1; Hubble Space Telescope (HST) observations through the WFC3 imaging in the F110W (984 s of exposure) and F200LP (817 s of exposure) filters, sampling the rest-frame emission in the ranges 4170-6480 and 925-4600 Å, respectively; and a detection of a weak 887 MHz radio source approximately at the cluster's center, taken with the Australian Square Kilometre Array Pathfinder (ASKAP). Images of these main observations are shown in Figure 3.1.

The pivotal work on SPT2215's physical properties was done by Calzadilla et al. (2023). They presented a detailed multiwavelengh analysis, providing evidence for a regular X-ray morphology, highly efficient central cooling and a remarkably high star formation rate in the BCG, as revealed by the performed SED fitting. The X-ray analysis was applied to three out of the ten currently available Chandra observations (OBS-IDs: 22653, 24614 and 24615; PI: Mcdonald) taken with the ACIS-I instrument and totaling 72.26 ks. For spatially-resolved spectroscopic analysis of the X-ray data, they extracted spectra from fine (to compute the emission measurement) and coarse (to compute the electron temperature) annular regions and fitted them with a *phabs*apec* spectral model for a collisionally ionized, optically thin hot plasma affected by photoelectric absorption [1]. The emission measure profile was fitted with the projected analytical model of Vikhlinin et al. (2006) (Equation 3 of their paper). The 3-dimensional ICM temperature was obtained by fitting the *apec* temperature from the coarse bins with the para-

[1]Details on the parameters describing *phabs* and *apec* models can be find on https://heasarc.gsfc.nasa.gov/xanadu/xspec/manual/XSmodelPhabs.html and https://heasarc.gsfc.nasa.gov/xanadu/xspec/manual/node134.html, respectively.

metric model of Vikhlinin et al. (2006) (Equation 6), which also includes the cooling time profile as a broken power law (Equation 4). Table 3.1 summarizes important estimated properties of SPT2215 from various sources. Figure 3.2 shows the constructed thermodynamic profiles from their analysis. The found 3D temperature, entropy and cooling time profiles are consistent with the properties of a strong cool core cluster, that is, continuous inward decrease of temperature, low central entropy ($K < 30$ keV cm^2) and low central cooling time ($t_{\rm cool} = 1$ Gyr). The work estimate a maximum mass cooling rate of $\dot{M}_{\rm cool} \equiv M_{\rm gas}(r < r_{\rm cool})/t_{\rm cool}(r = r_{\rm cool}) = 1900 \pm 400\ M_\odot\ {\rm yr}^{-1}$, where $r_{\rm cool} = 116 \pm 15$ kpc was chosen as the radius where the $t_{\rm cool} = 3$ Gyr. Such cooling rate is extremely high and compared to only a few other clusters. Therefore, the high star formation rate (SFR) implied by the SED fitting is not unexpected, since such core conditions must propitiate the condensation of the central cooling multiphase gas, fueling star formation in the BCG, as previously discussed in Section 2.4. The X-ray data was not sufficiently deep to detect cavities, but they performed a k-correction (assuming a spectral index of $\alpha = -0.7$ to find the correspondent 1.4 Ghz radio luminosity from the 0.8 GHz ASKAP flux as $9.2 \cdot 10^{40}$ erg s^{-1}. Then, they used the 1.4 GHz radio luminosity versus cavity power scaling relation from Cavagnolo et al. (2010) to estimate $\log(P_{\rm cav}/10^{42}\ {\rm erg\ s^{-1}}) = 2.6 \pm 0.3$ (stat.) ± 0.8 (int. scatter). Considering the estimated cooling luminosity, this cavity power leads to a $P_{\rm cav}/L_{\rm cool} = -1 \pm 0.8$, indicating that, even for upper bound of the $P_{\rm cav}$, radiative cooling is outweighing AGN heating.

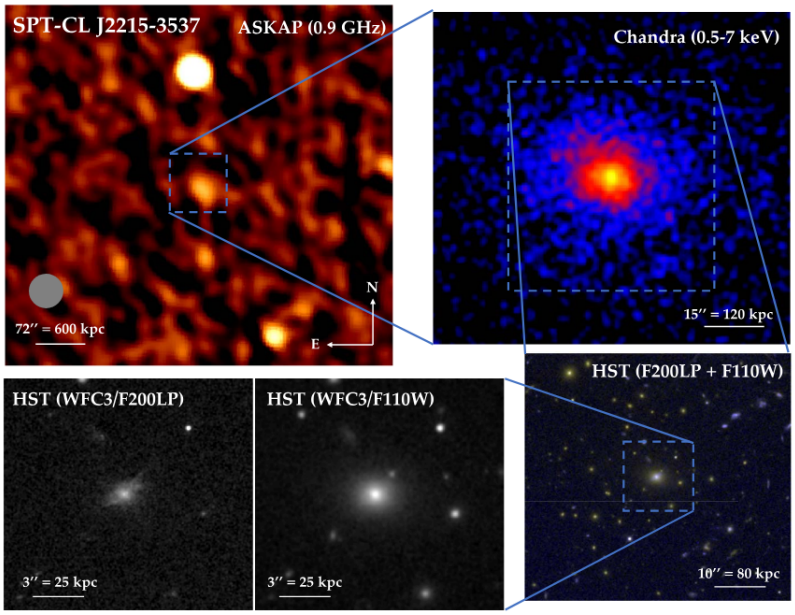

Figure 3.1: Multiwavelengh observations of SPT2215. Top left: ASKAP 887 MHz radio image. Top right: 0.5-7 keV Chandra X-ray image. Bottom left: HST observations of SPT2215's BCG in the F200LP and F110W filters. Bottom right: two-band F200LP+F110W composite image of the cluster. Source: Calzadilla et al. (2023).

Table 3.1: Properties of SPT2215.

Property	Value
M_{500c} (SPT)	$(7.32^{+0.81}_{-0.86}) \times 10^{14}\ M_\odot$
M_{2500c} (cosmo)	$(2.40 \pm 0.35) \times 10^{14}\ M_\odot$
$M_{\rm BCG}$	$(5.9 \pm 0.6) \times 10^{11}\ M_\odot$
$\rm SFR_{BCG}$	$(320^{+230}_{-140}\ M_\odot\ \rm yr^{-1})$
$L_{\rm cool}$	$(3.7 \pm 0.1) \times 10^{45}\ \rm erg\ s^{-1}$
$\max(\dot{M}_{\rm cool})$	$1900 \pm 400\ M_\odot\ \rm yr^{-1}$
z	1.16

Notes: Line 1: SZ-derived enclosed mass at r_{500c} (Bleem et al. 2020). Line 2: reference cosmology enclosed mass at r_{2500c} from Mantz et al. (2022). Lines 3, 4, 5 and 6: BCG mass, star formation rate, cooling luminosity and maximum mass cooling rate, respectively, from Calzadilla et al. (2023). Line 7: cluster's redshift from Bleem et al. (2020).

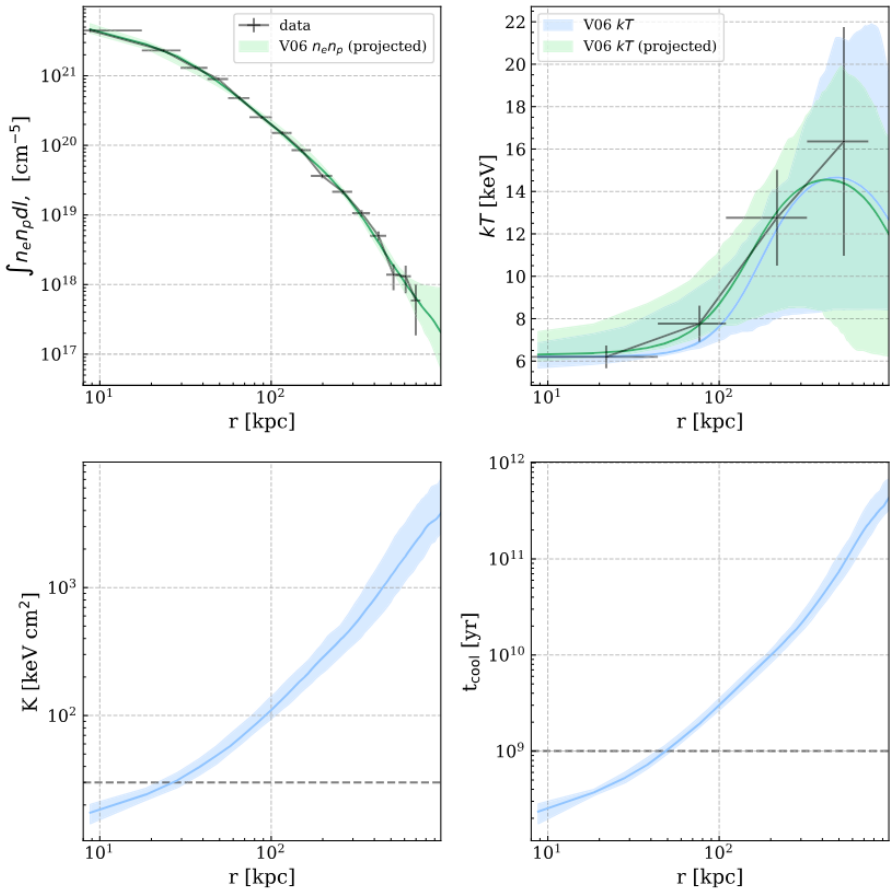

Figure 3.2: SPT2215 thermodynamic profiles from Calzadilla et al. (2023). Top left: emission measure profile. Top right: projected and 3D temperature profile. Bottom left: 3D pseudo-entropy profile, horizontal dashed line marks the entropy threshold $K = 30$ keV cm. Bottom right: 3D cooling time, horizontal dashed line marks $t_{\rm cool} = 1$ Gyr.

Before the work done by Calzadilla et al. (2023), Mantz et al. (2022) had already classified SPT2215 as a dynamically relaxed cluster, including it in their extended sample of massive relaxed clusters suitable for $f_{\rm gas}$ cosmology. The employed dynamical classification was based on the Symmetry–Peakiness–Alignment (SPA) criteria, a set of X-ray morphological parameters, designed to be applicable to large datasets spanning a wide range of redshifts, masses, and data qualities (Mantz et al. 2022). Broadly speaking, the peakiness parameter measures how centrally sharp the surface brightness distribution is, aiming to probe the presence of a bright, cool core, commonly associated to dynamically relaxed systems (Fabian 1994). The other two statistics are calculated from a set of fitted elliptical isophotes: the allignment is sensitive to shifts in the center of emission at larger scales, that is, how the isophote centers agree with each other, while the symmetry incorporates how the center of each ellipse deviates from the global center [2]. Figure 3.3 shows that SPT2215 is strongly located in regions of the SPA parameter spaces mostly associated to dynamically relaxed clusters, which is surprising for a cluster at such high redshift, indicating a rapid, early evolution towards virialization.

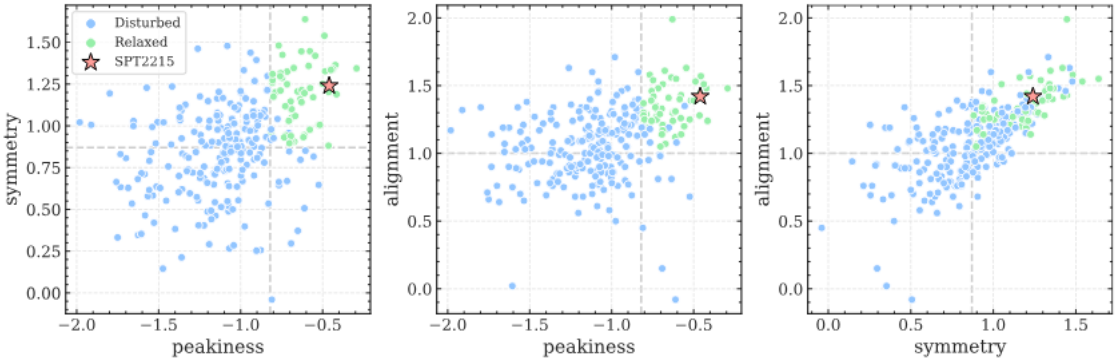

Figure 3.3: Parameter spaces of SPA criteria for the cluster samples of Mantz et al. (2015) and Mantz et al. (2022). SPT2215 is highlighted. Source: Calzadilla et al. (2023).

[2] See explanation of equations 5, 6 and 7 of Mantz et al. (2015) for details.

Chapter 4

Methodology

4.1 Data Reduction

All relevant quantities were calculated considering a standard flat ΛCDM cosmology, with $H_0 = 70\,\mathrm{km\,s^{-1}Mpc^{-1}}$, $\Omega_m = 0.3$, and $\Omega_\Lambda = 0.7$. Unless otherwise noted, all quoted uncertainties represent 1σ confidence intervals and, when needed, are propagated using the partial derivatives method considering the covariance matrices given by the fits. The science products were obtained in the usual way using the X-ray Data Analysis Software (Ciao 4.17). We used all ten archived Chandra observations available: three were taken with ACIS-I (OBS-ID: 22653, 24614, 24615; PI: McDonald), and seven with ACIS-S (OBS-ID: 25468, 25902, 25903, 25904, 26244, 26372, 27614; PI: Mantz), as showed in Table 4.1.

Table 4.1: Raw information of all available archived Chandra observations of SPT-CLJ2215-3537

Obs ID	**Instrument**	**Exp. (ks)**	**Avg. Rate (ct/s)**	**Evt. Count**	**PI**
22653	ACIS-I	34.62	3.03	104753	McDonald
24614	ACIS-I	28.69	3.81	109165	McDonald
24615	ACIS-I	8.95	3.86	34558	McDonald
25468	ACIS-S	22.26	11.61	258407	Mantz
25902	ACIS-S	28.24	8.55	241532	Mantz
25903	ACIS-S	9.93	9.05	89829	Mantz
25904	ACIS-S	30.71	6.78	208116	Mantz
26244	ACIS-S	23.24	11.64	270635	Mantz
26372	ACIS-S	7.96	7.30	58089	Mantz
27614	ACIS-S	9.93	9.23	91676	Mantz

Notes: Column (1): Chandra Observation ID. (2): Instrument used. (3): Total exposure time in kiloseconds. (4): Average count rate. (5): Total event count. (6): Principal Investigator. Include all used CCDs in each observation.

The individual observations were downloaded and reprocessed using up-to-date cal-

ibration data from CALDB version 4.11.6 with additional background cleaning for the VFAINT telemetry mode. The reprocessed events files were filtered to the 0.5-7 keV band and the ACIS-I3 or ACIS-S3 chips were selected according to the observation. The exposure maps were created with the *fluximage* script using source characteristic spectral weights. Point sources were removed using the *wavedetect* tool followed by an additional eye check. Bad time intervals were identified through the source lightcurves in order to eliminate flares and create cleaned event files. The total filtered exposure time was 188.12 ks (around 92% of the total exposure).

4.2 X-Ray Spectral Analysis

4.2.1 Radial Thermodynamic Profiles

Annuli regions around the BCG position ($\alpha = 22^{\mathrm{h}}15^{\mathrm{m}}03.^{\mathrm{s}}9306, \quad \delta = -35°37'17.''885$) were selected. The correspondent Blank-Sky files were used to account for the background contribution. The spectra of all reprojected observations were extracted using *specextract* and then simultaneously fitted with a *phabs*apec* model using Xspec version 12.14.1 (Arnaud 1996). The abundances were fixed at $0.3\,Z_{\odot}$, temperatures were tied to each other and the remaining parameters (the normalizations) were kept independent. The hydrogen column was fixed at $nH = 1.01 \cdot 10^{20}$ cm^{-2} according to the HI4PI survey (HI4PI Collaboration et al. 2016). The deprojection of thermodynamic quantities was performed using the onion-peeling method under the assumption of spherical symmetry in concentric shells, similarly to the recipe presented in Ghizzardi et al. (2004). The electron number density n_e was derived from the deprojected normalization parameter N of the spectral model,

$$n_e = 10^7 D_A (1+z) \sqrt{\frac{4\pi N}{0.83V}}, \tag{4.1}$$

where $D_A = 1701.686$ Mpc is the angular diameter distance, $z = 1.16$ is the redshift, V is the considered shell volume, and 0.83 term comes from the ionization factor $0.83 n_e = n_p$. We additionally fit the surface brightness with a one-dimensional beta model, assuming the cooling function $\Lambda(k_B T, Z)$ parameterized by Tozzi and Norman (2001). This allows us to obtain an analytical curve for the electron number density, given by 2.30, where core radius r_c, the beta parameter β and the central surface brightness S_0 come directly from the fit. The central density is calculated using 2.34. With the temperature T and the electron number density n_e profiles, we can easily compute the pseudo-pressure and pseudo-entropy, which are, respectively, given by 2.24 and 2.23, respectively. Finally, we can calculate the cooling time with 2.25.

Figure 4.1 shows the deprojected electron density profile both from the spectral mod-

eling and from the β-model fit. The electron density exhibits a pronounced decline at $r_{\rm sharp} = 159 \pm 5$ kpc. In Figure 4.2 we show the correspondent radial profiles of the main 3D thermodynamic quantities, with the values organized in Table 4.2. The feature in $r_{\rm sharp}$ is further corroborated in the thermodynamic profiles, where we observe a steep rise in both temperature and entropy beyond the discontinuity, while the pressure remains nearly constant. All projected radial profiles consistently point toward a common feature: a contact discontinuity located at a projected radius of approximately 160 kpc. The presented picture is consistent with the physical conditions expected for a cold front. Interestingly, the estimated cooling radius, $r_{\rm cool} = 147 \pm 10$ kpc, is very close to the location of the discontinuity. Another feature worth mentioning is the flat central temperature profile for regions below $r_{\rm cool}$. Although SPT2215 manifest clear properties of a well developed cool core (eg., centrally peaked surface brightness, $K_0 < 30$ keV·cm^2, $t_{\rm cool,0} < 1$ Gyr), its temperature profile deviates from the classical cool core behavior, lacking the expected continuous decline toward the cluster center.

4.2.2 Projected Thermodynamic Maps

In order to easily identify directions of interest and probe potential anisotropies in the physical properties of the ICM, we constructed maps of the projected thermodynamic parameters. To do so, we first applied a Weighted Voronoi Tesselations (WVT) algorithm to partition the field of view, ensuring a nearly constant S/N. The basic Voronoi Tesselations algorithm for spatial adaptative binning is described in details in Cappellari and Copin (2003). Several applications of the WVT method to X-ray data are presented in Diehl and Statler (2006), as well as its advantages over other well-used algorithms such as the Quadtree. Then, the spectrum of each region/bin is extracted and fitted with Xspec using the *phabs*apec* model as before. The WVT algorithm naturally minimizes the sharpness of bin edges, but they are still discontinuous. To improve the visualization, we applied Universal Kriging interpolation using the PyKrige Python package[1], which allows spatial smoothing while accounting for the underlying trends in the data.

Figure 4.3 shows our maps for the projected thermodynamic quantities, with correspondent values organized in Table 4.3. It is important to note that because of the low S/N regime, these maps should be read qualitatively. The temperature map shows some interesting features. First, it appears that the coldest region is displaced from the BCG center by roughly 5 arcsec (~ 50 kpc) to the southeast. We fit the spectra of a joint set of these peripheral cold clumps, indicated in Figure 4.3 as white ellipses, and find a statistical significance of 1.8σ that these regions are indeed colder than the center. The second

[1]The package documentation is available on http://pykrige.readthedocs.io/. The temperature and entropy maps used a spherical variogram model with linear drift terms, while the pressure map used a hole-effect variogram model, as the standard ones were unable to adequately capture the spatial structure of the data.

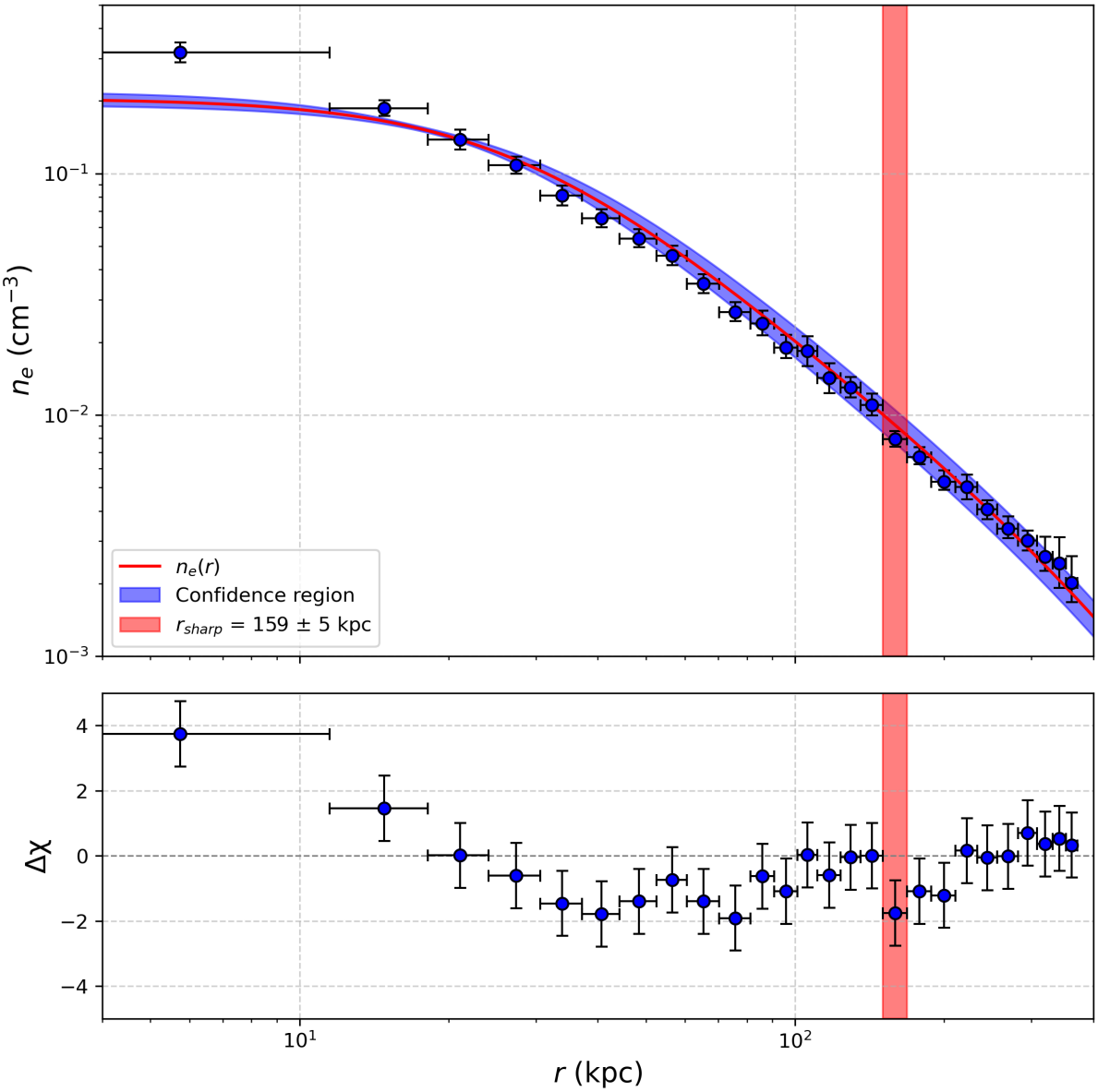

Figure 4.1: Top: Deprojected electron density profile. Bottom: residual between the data and the model.

Notes: The blue dots were obtained from Equation 4.1, while the red curve corresponds to the β-model applied to the surface brightness profile, whose optimal parameters are inserted in Equation 2.30. The sharp decline observed in both the density profile and the residual around $r_{\text{sharp}} \approx 160$ kpc is associated to two symmetric cold fronts, indicating a localized discontinuity.

feature is the apparent sudden temperature increase in the southeast and northwest directions approximately around r_{cool}, confirming the orientation of the discontinuities. On the other hand, the entropy map exhibits a smoother distribution in the core, with its lowest value aligned with the cluster's center. The pressure map suggests the presence of possible central substructures, with a higher pressure tail towards the NE direction.

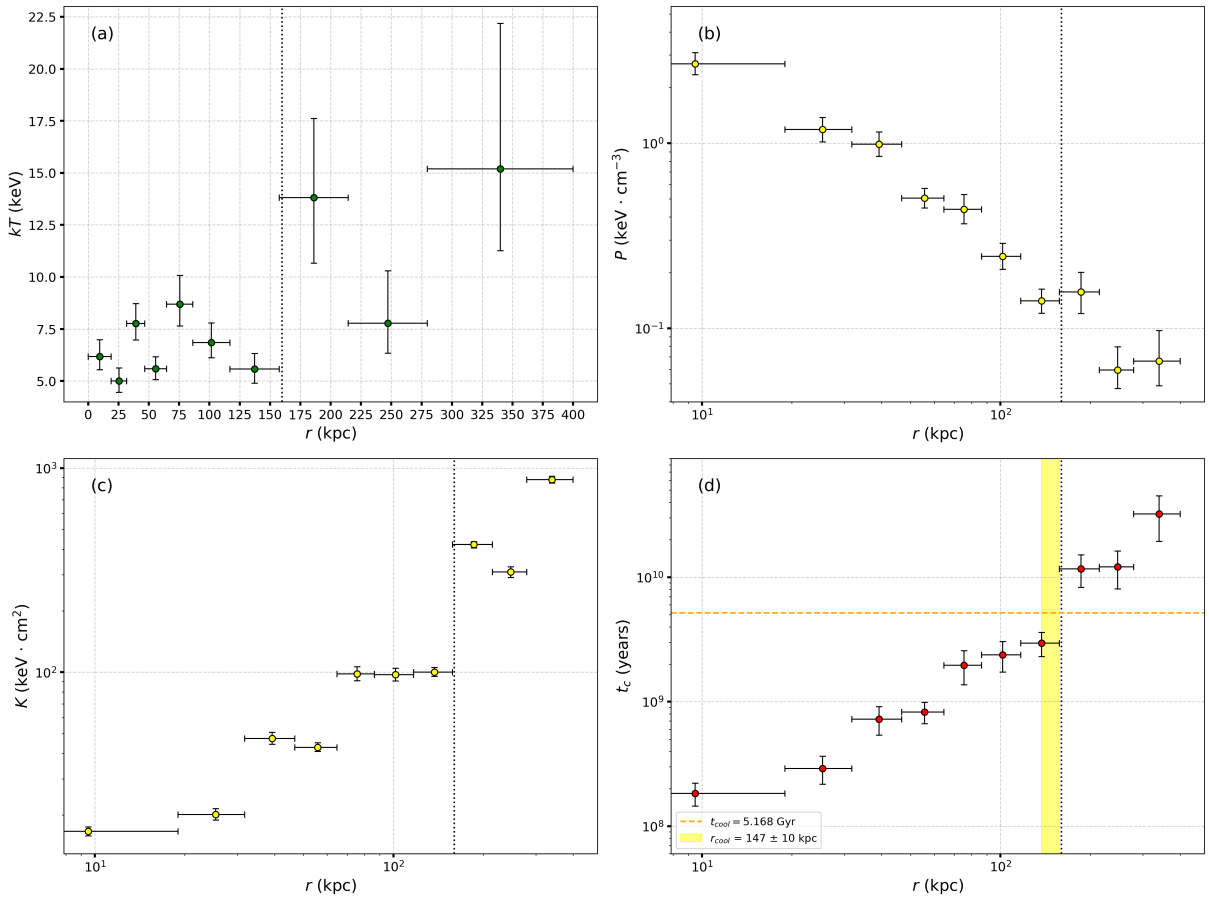

Figure 4.2: Radial profiles of various 3D thermodynamic quantities: (a) Temperature (kT), (b) Pressure (P), (c) Entropy (K), and (d) Cooling Time (t_c). The shaded region in (d) indicates the cooling radius r_{cool}. The dotted vertical line in all panels mark $r = 160$ kpc to indicate the approximate projected radius of the observed discontinuity.

4.2.3 Directional Thermodynamic Profiles

Based on the spatial features revealed in the thermodynamic maps, we defined concentric annular regions along four specific directions: northwest (NW), northeast (NE), southeast (SE), and southwest (SW), as indicated in Figure 4.4. We then applied the same procedure described in Section 4.2.1 to derive directional thermodynamic profiles. The results, presented in Figure 4.5, are consistent with the trends observed in the thermodynamic maps, revealing anisotropies in the central regions. While the SE-NW axis shows a relatively smooth temperature decline to the center, the temperature profile in the SW-NE axis has clear temperature dips and entropy flattening at $r \approx 180$ kpc. The geometry of the opposed dipolar discontinuities seen in the temperature map of Figure 4.3 is consistent with cold fronts viewed close to the plane of the sky. This makes it unlikely that the observed flattening of these profiles are due to projection effects. We discuss the possible origin of this feature in Section 5.4. Notably, at the radial bin corresponding to the identified discontinuity at $r_{\rm sharp} \approx 160$ kpc, the profiles along the SE–NW axis exhibit similar behavior, characterized by coincident temperature and entropy enhancements as well as a

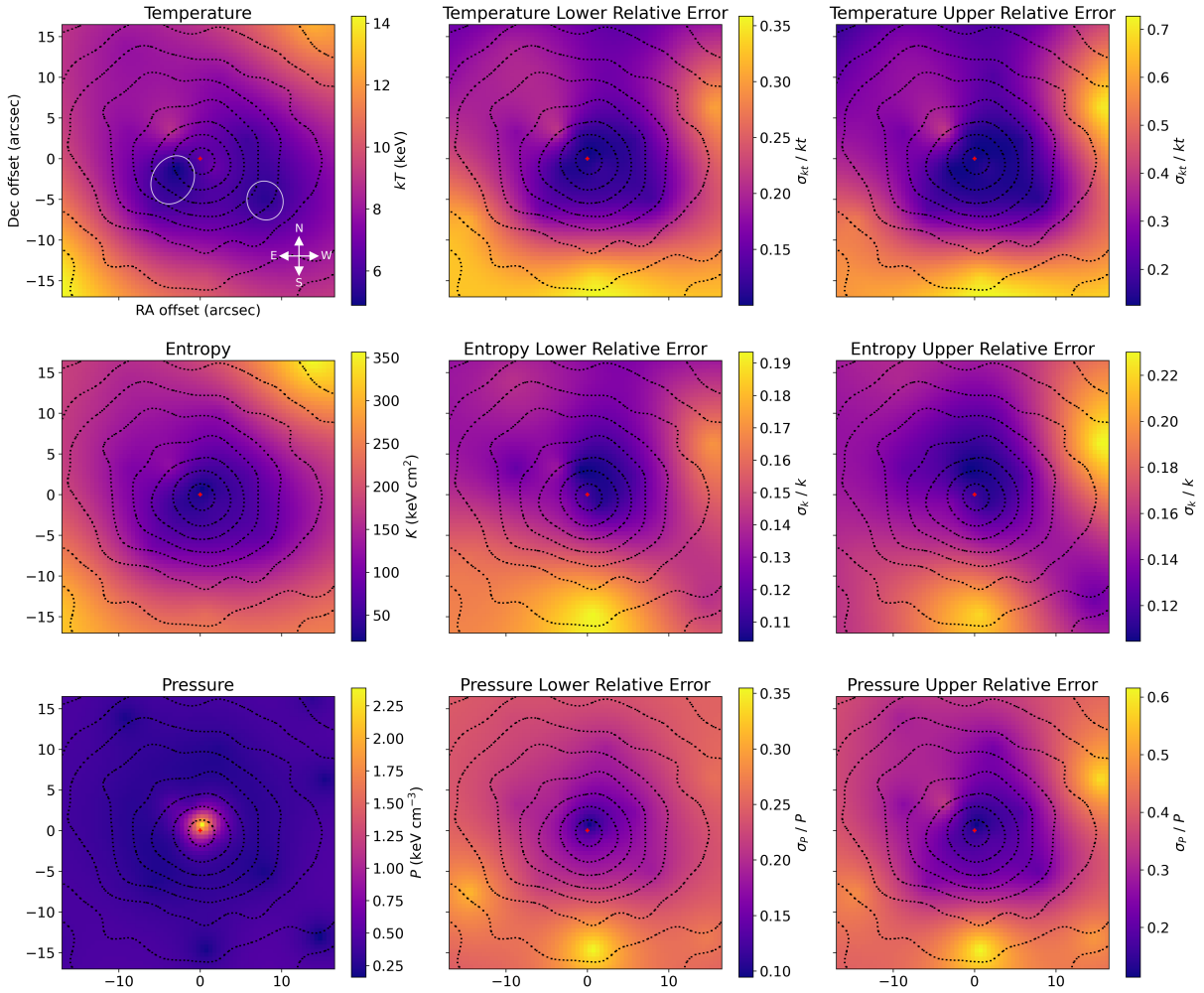

Figure 4.3: Projected thermodynamic maps (temperature, pseudo-entropy, and pseudo-pressure) derived using WVT adaptive binning followed by kriging interpolation, along with the corresponding lower and upper residual error maps. White ellipses in the temperature map indicate the approximate locations of colder clumps. The red cross marks the position of the BCG. Coordinates are shown as offsets from the BCG in arcseconds (1 arcsec = 8.25 kpc).

flat pressure profile. These features confirm the presence of two aligned cold fronts along this axis.

4.3 X-Ray Imaging Analysis

To visually inspect the ICM anisotropies hinted by the thermodynamic maps, we reproject the observations to a common tangent point and create a merged, exposure-corrected image. Again, we use the correspondent blanksky files to subtract the scaled backgrounds from the science images.

Table 4.2: Global Cluster Properties from Coarse Binning

(1) $r \pm \Delta r$ (kpc)	(2) kT (keV)	(3) P (keV cm^{-3})	(4) K (keV cm^2)	(5) t_c (10^8 yr)	(6) $\chi^2_{\rm red}$
9.5 ± 9.5	$6.18^{+0.80}_{-0.64}$	$2.69^{+0.40}_{-0.34}$	$16.61^{+0.84}_{-0.82}$	1.83 ± 0.38	0.81
25.4 ± 6.4	$5.00^{+0.62}_{-0.54}$	$1.19^{+0.40}_{-0.17}$	$20.11^{+1.36}_{-1.27}$	2.91 ± 0.74	0.69
39.2 ± 7.5	$7.77^{+0.96}_{-0.80}$	$0.99^{+0.16}_{-0.14}$	$47.37^{+3.34}_{-3.06}$	7.25 ± 1.87	0.79
55.7 ± 9.0	$5.59^{+0.57}_{-0.53}$	$0.51^{+0.06}_{-0.06}$	$42.89^{+2.18}_{-2.01}$	8.25 ± 1.61	0.72
75.5 ± 10.4	$8.69^{+1.38}_{-1.05}$	$0.44^{+0.09}_{-0.07}$	$98.16^{+8.08}_{-7.42}$	19.62 ± 5.99	0.76
101.6 ± 13.1	$6.85^{+0.94}_{-0.73}$	$0.24^{+0.04}_{-0.04}$	$97.42^{+7.10}_{-6.80}$	23.81 ± 6.52	0.77
137.2 ± 18.7	$5.57^{+0.75}_{-0.68}$	$0.14^{+0.02}_{-0.02}$	$100.07^{+5.30}_{-4.84}$	29.50 ± 6.44	0.78
186.0 ± 27.4	$13.82^{+3.79}_{-3.16}$	$0.16^{+0.04}_{-0.04}$	$422.34^{+14.30}_{-15.91}$	116.77 ± 33.93	0.87
247.1 ± 33.5	$7.77^{+2.52}_{-1.44}$	$0.06^{+0.02}_{-0.01}$	$309.64^{+18.38}_{-18.74}$	121.07 ± 40.73	0.92
339.8 ± 58.1	$15.20^{+6.98}_{-3.94}$	$0.07^{+0.03}_{-0.02}$	$878.24^{+32.58}_{-33.80}$	321.72 ± 128.2	0.94

Notes: Radial profiles of global thermodynamic properties derived from spectral modeling. (1) Radius; (2) Temperature; (3) Pseudo-pressure; (4) Pseudo-entropy; (5) Cooling time; (6) Reduced χ^2 of spectral fit.

4.3.1 Residual map

We start by adaptatively smoothing the merged image using the Ciao tool *dmimgadapt* with a gaussian kernel, demanding 16 counts per kernel and a minimum and maximum scale of, respectively, 0.5 and 15 pixels. Then, we proceed to model the radial distribution of the surface brightness with an elliptical 2D double-β model, where each component is defined by

$$S(x_i, y_i) = S(r) = A\left[1 + \left(\frac{r}{r_c}\right)^2\right]^{-\beta} + C, \tag{4.2}$$

where

$$r(x_i, y_i) = \frac{\sqrt{x^2(1-e)^2 + y^2}}{1-e}, \tag{4.3}$$

and

$$\begin{aligned} x &= (x_i - x_0)\cos\theta + (y_i - y_0)\sin\theta, \\ y &= (y_i - y_0)\cos\theta - (x_i - x_0)\sin\theta. \end{aligned} \tag{4.4}$$

Here, (x_0,y_0) is the centroid of the cluster, e is the ellipticity and θ is the orientation of the major axis relative to the north in the anti-clockwise direction (position angle). The initial values of the cluster shape parameters were calculated using the method of moments of inertia of Plionis et al. (1991). The first two moments would give us the position of the centroid, but we rather prefere to compute it with Equation 4.2. The other moments are

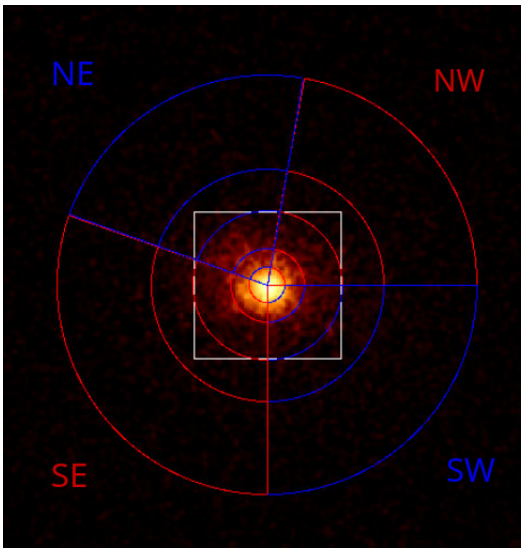

Figure 4.4: Directional sectors and central region used in the analysis. The $17'' \times 17''$ white box marks the area of the thermodynamic maps. Sectors: NE (80°–160°), SE (160°–270°), NW (0°–80°), SW (270°–360°).

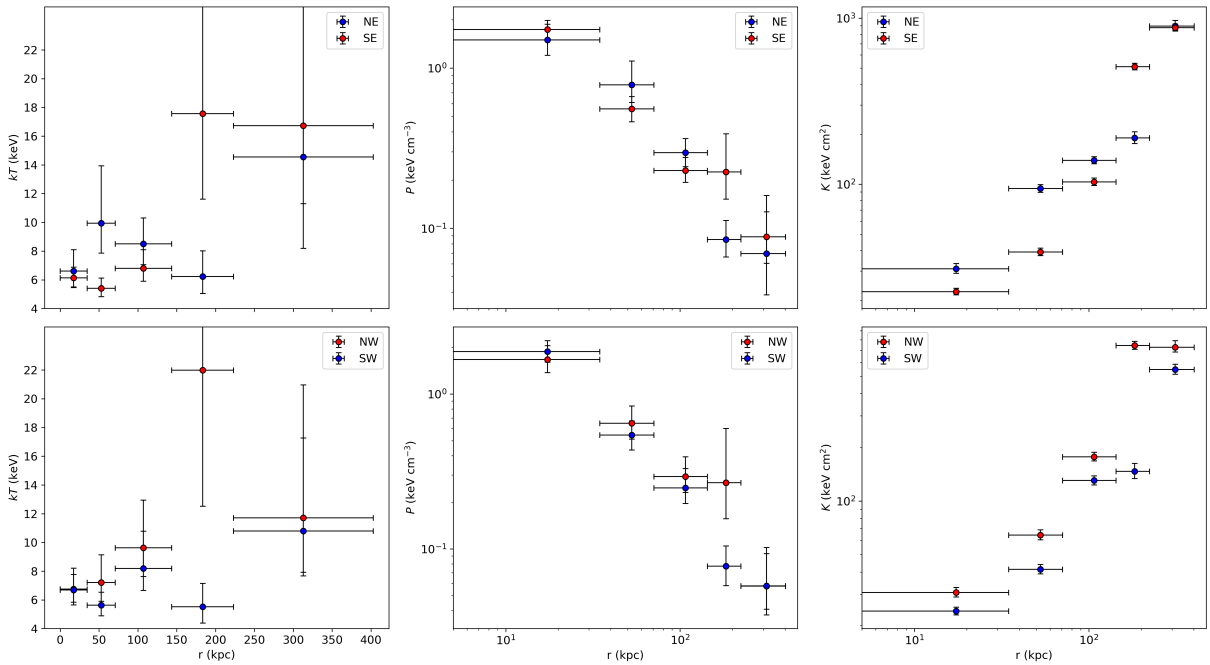

Figure 4.5: Directional projected thermodynamic profiles extracted from sector-shaped annuli. The upper panels compare the NE and SE directions, while the lower panels show the NW versus SW directions.

$$I_{11} = \sum_{i=1}^{N} \rho_i (b_i^2 - x_i^2), \tag{4.5}$$

$$I_{22} = \sum_{i=1}^{N} \rho_i (b_i^2 - y_i^2), \tag{4.6}$$

$$I_{12} = I_{21} = -\sum_{i=1}^{N} \rho_i x_i y_i, \tag{4.7}$$

Table 4.3: Directional cluster properties

Dir.	$r \pm \Delta r$ (kpc)	kT (keV)	P (keV cm^{-3})	K (keV cm^2)	$\chi^2_{\rm red}$
NE	17.4 ± 17.4	$6.61^{+1.49}_{-1.16}$	$1.50^{+0.38}_{-0.30}$	$31.00^{+2.31}_{-1.93}$	0.94
NE	52.8 ± 18.1	$9.94^{+3.99}_{-2.08}$	$0.78^{+0.32}_{-0.18}$	$94.18^{+5.26}_{-4.82}$	0.75
NE	107.2 ± 36.3	$8.50^{+1.80}_{-1.45}$	$0.30^{+0.07}_{-0.05}$	$139.09^{+7.24}_{-6.17}$	0.81
NE	183.4 ± 43.6	$6.23^{+1.79}_{-1.18}$	$0.09^{+0.03}_{-0.02}$	$190.18^{+16.62}_{-14.80}$	0.72
NE	313.0 ± 99.3	$14.55^{+11.83}_{-6.36}$	$0.07^{+0.06}_{-0.03}$	$895.58^{+70.76}_{-53.51}$	0.92
SE	17.4 ± 17.4	$6.14^{+0.75}_{-0.63}$	$1.74^{+0.25}_{-0.22}$	$22.57^{+2.31}_{-1.93}$	0.70
SE	52.8 ± 18.1	$5.41^{+0.72}_{-0.58}$	$0.56^{+0.11}_{-0.10}$	$39.09^{+2.13}_{-1.97}$	0.75
SE	107.2 ± 36.3	$6.80^{+1.30}_{-0.89}$	$0.23^{+0.05}_{-0.04}$	$103.38^{+5.45}_{-5.34}$	0.79
SE	183.4 ± 43.6	$17.56^{+13.27}_{-5.94}$	$0.23^{+0.04}_{-0.04}$	$508.97^{+25.37}_{-21.77}$	0.77
SE	313.0 ± 99.3	$16.73^{+14.16}_{-5.43}$	$0.09^{+0.04}_{-0.02}$	$875.74^{+44.61}_{-40.46}$	0.86
NW	17.4 ± 17.4	$6.75^{+1.45}_{-1.10}$	$1.67^{+0.38}_{-0.30}$	$30.72^{+2.06}_{-1.80}$	0.87
NW	52.8 ± 18.1	$7.21^{+1.92}_{-1.31}$	$0.65^{+0.11}_{-0.09}$	$64.46^{+4.47}_{-3.92}$	0.70
NW	107.2 ± 36.3	$9.62^{+3.32}_{-2.00}$	$0.29^{+0.10}_{-0.06}$	$176.90^{+10.53}_{-9.40}$	0.75
NW	183.4 ± 43.6	$21.98^{+28.48}_{-9.47}$	$0.27^{+0.33}_{-0.11}$	$745.28^{+39.20}_{-37.50}$	0.69
NW	313.0 ± 99.3	$11.72^{+9.24}_{-4.05}$	$0.06^{+0.04}_{-0.02}$	$727.54^{+64.57}_{-44.37}$	0.91
SW	17.4 ± 17.4	$6.69^{+1.08}_{-0.85}$	$1.88^{+0.33}_{-0.27}$	$24.12^{+1.24}_{-1.15}$	0.77
SW	52.8 ± 18.1	$5.63^{+0.90}_{-0.74}$	$0.54^{+0.13}_{-0.11}$	$41.34^{+2.63}_{-2.32}$	0.80
SW	107.2 ± 36.3	$8.18^{+2.60}_{-1.53}$	$0.25^{+0.08}_{-0.05}$	$130.28^{+8.02}_{-7.42}$	0.69
SW	183.4 ± 43.6	$5.52^{+1.63}_{-1.13}$	$0.08^{+0.03}_{-0.02}$	$146.56^{+16.03}_{-12.99}$	0.85
SW	313.0 ± 99.3	$10.80^{+6.47}_{-2.88}$	$0.06^{+0.04}_{-0.02}$	$546.30^{+38.18}_{-33.34}$	0.99

Notes: Azimuthal variations in thermodynamic properties. (1) Direction sector; (2) Radius; (3) Temperature; (4) Pseudo-pressure; (5) Pseudo-entropy; (6) Reduced χ^2 of spectral fit.

where

$$b_i = \sqrt{x_i^2 + y_i^2}. \tag{4.8}$$

The parameter ρ_i represents a generic density function, in our case it's the brightness distribution in the pixel grid. I_{11} and I_{22} are equivalent to the variances along the x and y axes, while $I_{12} = I_{21}$ represents the covariance between the axes. The inertial tensor is then

$$I = \begin{bmatrix} I_{11} & I_{12} \\ I_{21} & I_{22} \end{bmatrix}. \tag{4.9}$$

Diagonalizating it,

$$\det(I - \lambda^2 M) = 0, \tag{4.10}$$

where M is the 2x2 identity matrix. The eigenvalues gives us the ellipticity ϵ,

$$\epsilon = 1 - \frac{\lambda_2}{\lambda_1} \quad \text{for} \quad \lambda_1 > \lambda_2, \tag{4.11}$$

while the corresponding eigenvectors provide the cluster's orientation. The position angle is given by

$$\theta = \cot^{-1}\left(-\frac{I_{22} - \lambda_1^2}{I_{12}}\right) + \frac{\pi}{2}. \tag{4.12}$$

We then apply a Levenberg-Marquardt fitting to refine the near-optimal solutions and properly estimate the uncertanties. The best fit parameters for the surface brightness model are presented in Table 4.4. Then, we calculate the normalized residual with (Data − Model)/Data. The residual map in Figure 4.6 exhibits a relatively low overall amplitude (± 0.25), but reveals a pronounced dipolar pattern within 15 arcseconds of the BCG. The directional variation in enhanced emission across the cluster radii suggests that this anisotropy is unlikely to be caused by projection effects from a triaxial structure. Instead, it likely arises from a non-symmetric distribution of cold gas, possibly driven by core sloshing. Indeed, the directional surface brightness profiles normalized by the azimuthally averaged brightness shows the oscillatory behavior characteristic of spiral-shaped cold gas structures near the cluster core. These features have been detected in X-ray imaging (Clarke et al. 2004), temperature maps (Fabian et al. 2005) and even in chemical enrichment distributions (Dupke et al. 2007), being also naturally reproduced in simulations (Ascasibar and Markevitch 2006).

Another finding from the β-model subtraction is a statistically significant extended depression (residual < -0.5 and local brightness dimming $\sim 25\%$). If this is a jet-driven X-ray cavity, we estimate from the projected elliptical shape a volume of $(2.07 \pm 1.10) \times 10^5$ kpc^3. From the spatially resolved thermodynamic information (using the relations presented in Section 2.3.1), we estimate that the necessary energy to inflate such bubble is $(2.73 \pm 1.86) \times 10^{60}$ erg. Considering that the projected distance between the BCG and the cavity's outermost edge is ~ 255 kpc, we calculate a sound-crossing time of 188 ± 22 Myr. Therefore, our final estimative for the jet power responsible for this possible cavity is $\log_{10}(P_{\rm cav}/10^{42}{\rm erg\ s^{-1}}) = 2.66 \pm 0.23$, consistent with the value reported by Calzadilla et al. (2023) using the $P_{\rm cav}$-$L_{\rm cool}$ scaling relation (Cavagnolo et al. 2010). Figure 4.7 shows the merged image, highlighting the position and orientation of the considered cavity. In Section 5.2, we further discuss the feasibility of such a bubble given its observed characteristics, as well as its implications for the cluster's dynamical history.

Table 4.4: Double Elliptical β-Model Fit Optimal Parameters

Parameter	Value	Units
β_1	0.545 ± 0.018	–
r_{c1}	4.9 ± 1.1	pixels
e_1	$(1.00 \pm 0.70) \times 10^{-2}$	–
β_2	0.912 ± 0.116	–
r_{c2}	30.3 ± 4.1	pixels
e_2	0.314 ± 0.029	–
θ	2.912 ± 0.016	radians
f	0.928 ± 0.030	–
A_1	$(4.58 \pm 0.20) \times 10^{-7}$	cnt s^{-1} cm^{-2}
C	$(1.38 \pm 1.14) \times 10^{-10}$	cnt s^{-1} cm^{-2}

Notes: Best-fit parameters for the 2D double-β model. The model consists of inner (1) and outer (2) components with ellipticities e, position angle θ, and flux fraction f, such that $A_2 = A_1(1 - f)$.

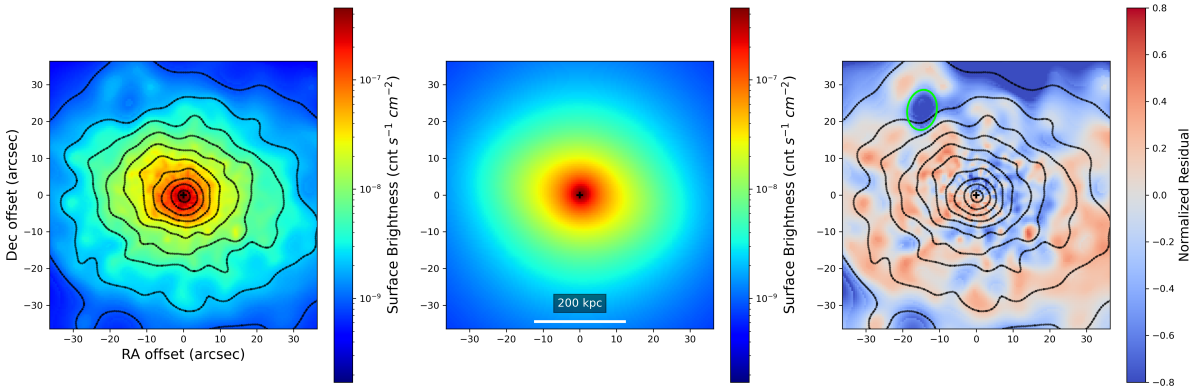

Figure 4.6: Left: Adaptively smoothed X-ray surface brightness map with overlaid contours. Middle: Best-fit double two-dimensional β-model (Equation 4.2); the optimal parameters are listed in Table 4.4. Right: Normalized residual map with the surface brightness contours. The green ellipse, centered at $\alpha = 22^{\rm h}15^{\rm m}05.^{\rm s}1467$, $\delta = -35°36'54.''829$, with semi-axes of 5.5 ± 1 and 4.0 ± 1 arcseconds and a position angle of 350°, encloses the X-ray cavity candidate. The black cross marks the position of the BCG. Coordinates are shown as offsets from the BCG in arcseconds (1 arcsec = 8.25 kpc).

4.3.2 Morphological Parameters

As previously mentioned, the first indication of the dynamical regularity of SPT2215 arose from the evaluation of its X-ray morphological features. Here, we take advantage of our increased image statistics to compute traditional metrics: concentration (c), centroid shift (ω), and the third-order power ratio (P_3/P_0), as well as the morphology index δ introduced by Yuan and Han (2020).

The concentration parameter c quantifies the surface brightness peak strength relative

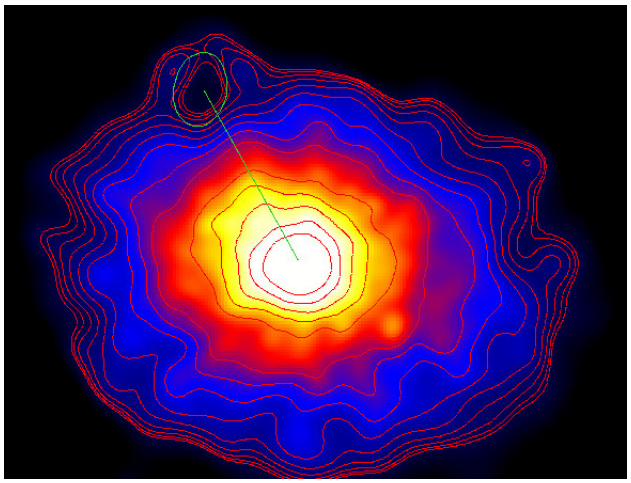

Figure 4.7: Merged adaptively smoothed 0.5-7 keV X-ray image, with green ellipse and line highlighting the position and orientation of the cavity candidate.

to the overall distribution and is mainly employed to identify the presence of cool cores. Here, we use the definition of c as the ratio of the integrated X-ray fluxes under the core radius and the outer radius apertures. We choose $r_{\rm in}$ = 100 kpc and $r_{\rm out}$ = 500 kpc for consistency with Yuan et al. (2022), therefore

$$c = \frac{S_{100\,kpc}}{S_{500\,kpc}} = \frac{\sum\limits_{R<100\,kpc} s_i(x_i, y_i)}{\sum\limits_{R<500\,kpc} s_i(x_i, y_i)}. \tag{4.13}$$

Following Poole et al. (2006), the centroid shift is defined as the standard deviation of the projected separation between the X-ray brightness peak and the model fitted center. These separations are computed along a series of n = 20 decreasing apertures starting from r_{out} = 500 kpc. Thus,

$$\omega = \frac{1}{r_{out}} \left[\frac{1}{n-1} \sum_i (\Delta_i - \langle\Delta\rangle)^2 \right]^{1/2}, \tag{4.14}$$

where Δ_i is the separation between the brightness peak and the fitted center in the ith aperture, and $\langle\Delta\rangle$ is the mean separation value. Here, the center for each apperture is fitted with a single 2D β-model. This metric is sensitive to deviations from symmetry across multiple spatial scales, though for highly peaked surface brightness distributions, it can be dominated by the core contribution, as it is going to be further discussed in Section 5.4.

Finishing the set of traditional morphological parameters, we compute the third-order power ratio P_3/P_0. It is particularly sensitive to substructures and departures from mirror symmetry (Jeltema et al. 2005). The powers are derived from the multipole expansion of the X-ray surface brightness within $r_{\rm out}$ (Buote and Tsai 1995; Buote and Tsai 1996). Thus, we have:

$$
\begin{aligned}
P_0 &= [a_0 \ln (r_{\rm out})]^2, \\
P_m &= \frac{1}{2m^2 r_{\rm out}^{2m}} (a_m^2 + b_m^2) \quad \text{for } m > 0,
\end{aligned}
\tag{4.15}
$$

with the multipole coefficients given by

$$
\begin{aligned}
a_m(r_{\rm out}) &= \int_{r<r_{\rm out}} s(x,y)\, r^m \cos(m\phi)\, dxdy, \\
b_m(r_{\rm out}) &= \int_{r<r_{\rm out}} s(x,y)\, r^m \sin(m\phi)\, dxdy.
\end{aligned}
\tag{4.16}
$$

where r and ϕ are the polar coordinates centered on the X-ray centroid.

The morphology index δ for SPT2215 was previosly calculated in Yuan et al. (2022) using one single observation (obsID= 24614), giving $\delta = 0.10 \pm 0.01$. Here, we check if this result holds for our merged image. The morphology index is defined as the distance to the line that best separates the dynamical state of a sample of 115 well studied clusters in the $\kappa - \alpha$ space:

$$
\delta = 0.68 \log_{10}(\alpha) + 0.73\kappa + 0.21. \tag{4.17}
$$

Here, the assymetric factor α and κ are independent parameters given by

$$
\alpha = \frac{\sum\limits_{x_i,y_i} [s_i(x_i,y_i) - s_i(x_i',y_i')]^2}{\sum\limits_{x_i,y_i} s_i^2(x_i,y_i)}, \tag{4.18}
$$

where $s_i(x_i', y_i')$ is the flux at the symmetry pixel of (x_i, y_i) with respect to the center, and

$$
\kappa = \frac{1+e}{\beta}, \tag{4.19}
$$

where e and β have the same meaning as before and are extracted from a single elliptical β-model fit. To ensure consistency with the empirical formula for δ, we adopt the same aperture and smoothing parameters used in Yuan and Han (2020) when computing α and κ. We obtain $\log_{10}(c) = -0.33$, $\log_{10}\omega = -2.57$, $\log_{10}(P_3/P_0) = -6.58$, $\log_{10}(\alpha) = -0.88$, $\kappa = 0.57$, and $\delta = 0.028$. These values are in good agreement to those reported in Yuan et al. (2022), as showed in Figure 4.8, suggesting that their convergence is not strongly limited by data quality or exposure time. We further discuss in Section 5.4 the numerical correlations among the considered metrics, as well as potential decouplings from the underlying physical phenomenology they are meant to trace.

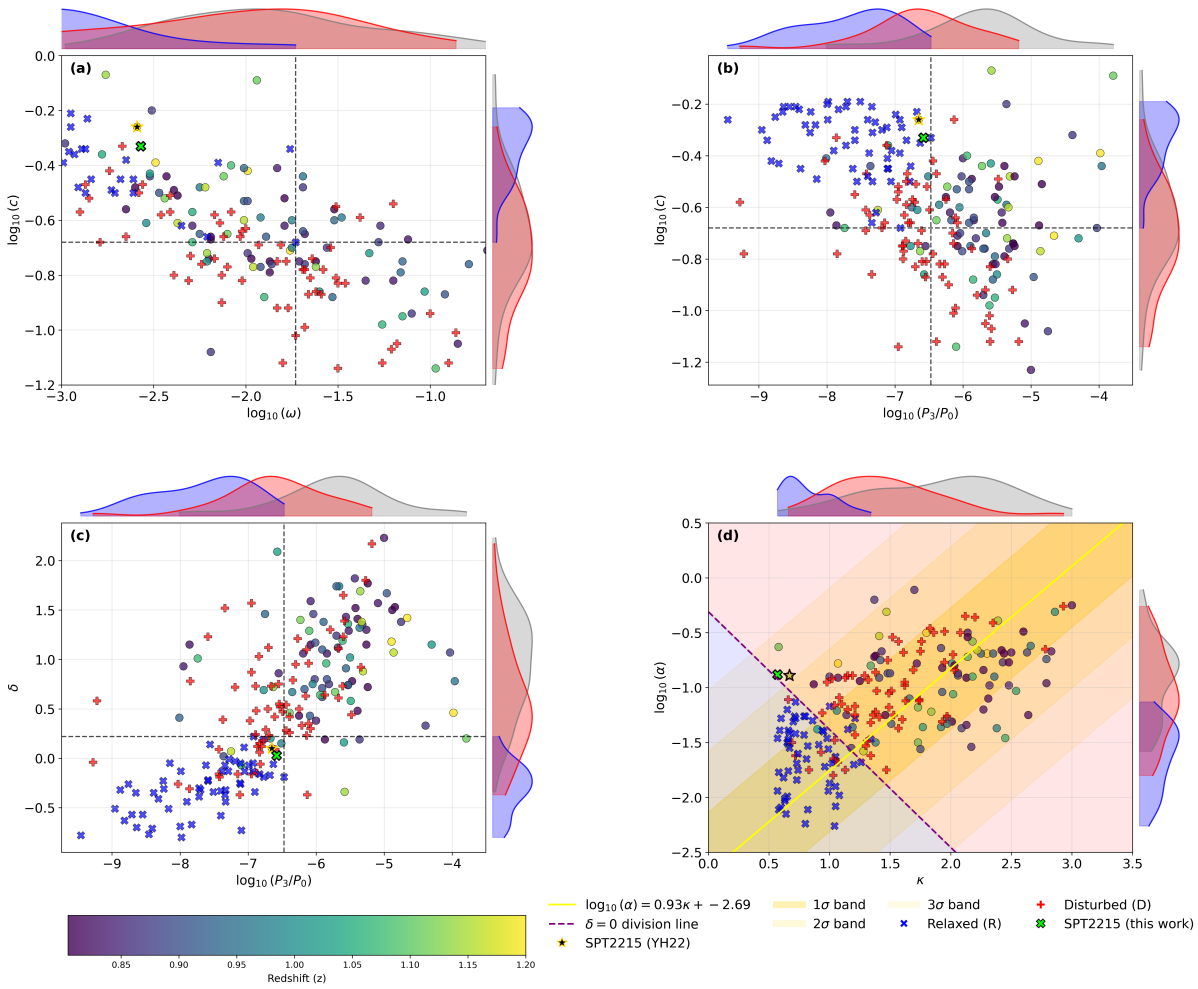

Figure 4.8: Parameter spaces of the morphological parameters considered in this work. Blue X's and red crosses represent the relaxed and disturbed clusters from the test sample of Yuan and Han (2020), respectively, which have independent dynamical classifications. Circles indicate the selected high-redshift subsample ($0.8 < z < 1.2$) from Yuan et al. (2022). The blue, red, and grey shaded regions on the outside of the plotting frames illustrate the distribution of relaxed, disturbed, and high-redshift clusters, respectively, in the parameter spaces. Dashed black lines mark the threshold values limiting the region occupied by relaxed clusters.

Chapter 5

Discussion

5.1 Core Sloshing

The thermodynamic characterization of SPT2215's ICM presented in this work reveals notable anisotropies. We detect what appears to be contact discontinuities along the SE–NW direction, approximately located at the estimated cooling radius, $r_{cool} = 147 \pm 10$ kpc. The observed sharp increase in temperature and entropy within the corresponding radial bin, accompanied by an approximately constant pressure, are well-established signatures of cold fronts. In Figure 4.5, the SE-NE temperature and entropy profiles is consistent with a core oscillation within the boundaries of $r_{\rm cool}$, where, below r_{cool}, the gas in the SE direction is considerably colder than in the NE. This mismatch then inverts just beyond r_{cool}, with the entropy profiles converging in the 210-410 kpc bin. This radial behaviour aligns with the central emission excess distribution seen in the residual map of Figure 4.6, which shows clear spiral patterns along multiple scales.

Spatial resolution limits the detection of cold fronts in clusters as distant as SPT2215. Even with the combined observations analyzed in this work, we do not detect them solely from the surface brightness. Nevertheless, the scenario supported by our spectral modeling is not unexpected, as many cool-core clusters contain signatures of cold fronts. The hydrodynamic simulations of mergers done by Ascasibar and Markevitch (2006) revealed that core sloshing can induce such discontinuities given a sufficiently steep entropy profile. When fitting the azimuthaly-averaged entropy profile with a power law, we get a slope of 1.12 ± 0.12, as predicted by self-similar evolution models (Tozzi and Norman 2001; Voit et al. 2005; Cavagnolo et al. 2009). Restricting the fit for the $[0.01\text{-}0.08]r_{180}$ range, we find a slope of 1.25 ± 0.18, in agreement with the mean scaled entropy profile slope of cold front clusters, $\alpha[(0.01\text{-}0.08)r_{180}] = 1.22 \pm 0.01$, reported by Ghizzardi et al. (2010). Given the steep entropy profile, a past off-axis interaction with a gas-poor substructure could have significantly perturbed the low-entropy gas

in the cluster's core, giving rise to sloshing cold fronts approximately at the cooling radius.

It is worth noting the coincident SE-NW orientation of the extended blue filaments in the BCG, as observed by the Hubble Space Telescope (HST) imaging in the F200LP filter (see bottom-right panel of Figure 3.1). It is plausible that sloshing-driven shear motions, alligned with draped magnetic fields, enable anisotropic thermal conduction that creates a preferential channel for the inflow cool of gas. A minimum local cooling time over the free-fall time $t_{\rm cool}/t_{\rm ff}$ below ~ 10 indicate conditions favorable for thermal instability and efficient multiphase condensation in the circumgalactic medium (Voit et al. 2015). We use Equation 2.26 to obtain a crude estimative of $t_{ff}(R)$, assuming hydrostatic equilibrium. We find a $\min(t_{\rm cool}/t_{\rm ff}) \approx 8$ at $r \approx 25$ kpc, indicating that the resulting condensation is fueling the intense starburst in the BCG (Calzadilla et al. 2023), and producing the observed filamentary structure preferentially along the sloshing axis.

5.2 Ghost Bubble Candidate

Let us now discuss the plausibility of the possible X-ray cavity revealed by our imaging analysis. The majority of cool core clusters harbour radio sources and bubble-like structures, filled with relativistic electrons, produced by AGN jets, likely triggered by accretion of cold gas onto the central supermassive black hole, as discussed in Section 2.4. The propagation of these bubbles is an efficient way of injecting energy into the central regions of the cluster, since it creates pressure waves that are viscously dissipated throughout the ICM. The ASKAP weak radio detection at 0.9 Ghz surrounding SPT2215's BCG indicates ongoing AGN feedback. We do not expect Ghz emission from a bubble with such high age ($t \approx 190$ Myr), making it a ghost bubble (X-ray cavity with no associated radio emission) candidate. The central radio emission is elongated along the same axis as the cavity's position relative to the cluster center, further supporting the hypothesis that this feature is indeed associated to the AGN duty cycle (as expected from collimated jets launched along a bipolar axis). Another supporting piece of evidence is the arc-shaped enhanced emission in the direction of the bubble propagation, seen in the residual map of Figure 4.6, which may result from compressed or turbulent gas driven by the bubble's expansion through the ICM.

Considering the observed cavity properties, we calculate a jet power that is consistent with the value obtained from the $P_{\rm cav}$-$L_{\rm cool}$ relation (Cavagnolo et al. 2010) reported by Calzadilla et al. (2023), but with a significant uncertainty improvement - $\log_{10}(P_{\rm cav}/10^{42}{\rm erg\ s^{-1}}) = 2.66 \pm 0.23$ against $\log_{10}(P_{\rm cav}/10^{42}{\rm erg\ s^{-1}}) = 2.6 \pm 0.3$ (stat) $\pm$

0.8 (int. scatter). Naturally, there are hard limits on the cavity's measurable features conditioned to spatial resolution and growth limit. In our case, the cavity's dimensions exceed the detection threshold for the considered redshift, while the high mean temperature of the surrounding ICM places it below the expected growth limit. From a sample of 148 cavities present in 69 targets, Shin et al. (2016) found a linear correlation between the cavity area and its projected distance expressed by $\log_{10}(A) = (1.94 \pm 0.04)\log_{10}(D) + 0.02 \pm 0.05$. Given $A \approx 4700 \pm 1400$ kpc^2 and $D \approx 230$ kpc, we find a deviation of $\Delta \log_{10}(A) \approx -0.93$ from the considered correlation, which corresponds to nearly 3σ. For this projected distance, the cavity's size should be about an order of magnitude larger. This could be seen as a main caveat of this observed feature as a real structure. On the other hand, it is worth to consider that the sample of clusters used by Shin et al. (2016) did not include any ghost bubbles. The growth conditions in high-redshift clusters can differ significantly due to evolving ICM properties (e.g., magnetic pressure, viscosity, thermal conduction), which may affect the morphology of highly evolved bubbles and cause deviations from general scaling relations (Bourne and Yang 2023).

5.3 Cooling-Feedback Cycle

Strong evidence supports the so called cooling–feedback model, in which radiative cooling and feedback from the central SMBH mutually influence and constrain each other in a self-regulating manner (Dunn and Fabian 2006; Main et al. 2017; Calzadilla et al. 2024)). Following the feedback-regulated precipitation framework developed by Voit et al. (2017) for cluster cores, we can attempt to qualitatively assess the current phase of SPT2215. In order to so, we consider three independent probes: the time since the AGN restarted, the minimum value of $t_{\rm cool}/t_{\rm ff}$ and the star formation rate in the BCG. If we take the cavity age calculated in Section 4.3.1 ($t_{\rm cav} \approx 190 \pm 20$ Myr) as a lower limit for the time since the last outburst, then SPT2215 would be likely in the early phase of progression towards a long-lasting self-regulated cycle. The found $\min(t_{\rm cool}/t_{\rm ff}) \approx 8$ is under the threshold for thermal instability, indicating that the isentropic region out to $r \approx 25$ kpc is still not completely formed. Considering that a steep central entropy gradient can only develop following the formation of a stable hot halo, a process expected to occur no earlier than $z \sim$ 2-2.5 for massive systems (Overzier 2016), a cluster observed at $z = 1.16$ would have at most ∼1.9-2.6 Gyr to be under a cooling-feedback loop. Therefore, it is reasonable to conclude that SPT2215 is, at most, about to enter the second long-lasting self-regulated cycle. The idealized simulation of a cluster core done by Li et al. (2015) (see Figure 2 of their paper) showed that the onset of star formation in the BCG can occur rapidly after the outburst event, leading to a drastic increase in the local buildup of cold gas. On the other hand, the response of $\min(t_{\rm cool}/t_{\rm ff})$ to the outflows happens in a considerably longer timescale. This delay arises from the fact that, before a stable isentropic core can develop,

the bulk low-entropy gas needs to be removed or reprocessed via turbulence, mixing and condensation. Approximately 190 Myr after the second outburst, the star formation rate would have enough time to be already stabilized around its peak, explaining the massive starburst in the BCG esimated by Calzadilla et al. (2023), SFR$= 320^{+230}_{-140} M_{\odot}\mathrm{yr}^{-1}$. The thermodynamic profiles along the supposed bipolar outflow axis (SW–NE) show notable deviations compared to the SE–NW direction, including a central temperature bump in the NE direction (Figure 4.5) and entropy flattening at intermediate scales (Figure 4.2). These asymmetries likely reflect enhanced inhomogeneities and turbulence induced by the recent AGN activity. In particular, uplift and mixing along the outflow axis can lead to transient entropy irregularities and deviations from hydrostatic equilibrium. As the system evolves toward a fully precipitation-regulated state, buoyancy and turbulent damping are expected to progressively erase these features, leading to a more symmetric and smoother thermodynamic structure.

5.4 Limitations of the Morphology-based Classification

The use of morphological parameters as proxies for cluster relaxation is based on the principle that the 2D projection of the emission reliably traces dynamical phenomena. Given X-ray observables and the underlying intrinsic state, the morphological measures serve as estimators of the true dynamical state. The mapping is non-injective, that is, distinct intrinsic states may produce similar 2D features as a result of projection or fundamentally different physical conditions, which is why classifications based on single measures must be taken with caution. Instead, the set of morphological parameters populate a multidimensional space where certain regions are empirically associated to relaxed and perturbed clusters. Thresholds are typically determined using a sample of clusters with independently confirmed dynamical states, or derived numerically from mock images of simulated clusters.

Let us now explore potential caveats of the presented framework and how it relates to the current classification of SPT2215. First, thresholds are naturally set to maximize the purity of relaxed/perturbed subsamples, which inevitable tends to misclassify systems with intermediate dynamical stages. This effect is likely to be more prevalent for high-redshift clusters due to the expected higher merger rate. Second, a fixed threshold assumes either that (1) the correlation between the 2D observable and a given 3D property associated to the dynamical state does not have a significant mass- or redshift-dependent evolution, or (2) the functional form of this evolution is known a priori, such that the parameter can be appropriately rescaled. This matter was addressed by Cao et al. (2021) (hereafter CBV21) using Mock-X (Barnes et al. 2021) to generate synthetic X-ray images of clusters from the IllustrisTNG, BAHAMAS and MACSIS cosmological hydrodynamical

simulations. They evaluated various aspects of the established morphological measures, including how they are correlated to each other and to 3D theoretical parameters extracted from the simulated halos. Regarding redshift evolution, although many specific considerations can be made about the impact of subgrid physics and numerical resolution on the observed trends for each simulation, CBV21 found that generally all morphological parameters exhibit some level of redshift evolution. This result highlights the critical importance of correctly modeling the functional form of this dependence.

Figure 4.8 shows the distribution of clusters in the relevant parameter spaces for three subsamples: relaxed (R), disturbed (D) and "high-redshift" ($0.8 < z < 1.2$) clusters. We may give special attention to parameters that are somehow dependent on the cluster's central emission cuspiness: more readily, the concentration index (c), and indirectly, the centroid shift (ω). First, we notice from Figure 4.8 that, with the exception of c and ω, all other parameters tend to produce a displaced distribution towards the unrelaxed end for the high-redshift subsample. Additionally, $c \times \omega$ gives the highest contamination for a relaxed region among all parameter spaces. We shall briefly discuss the origin of this trend. To begin, we must acknowledge a degree of numerical degeneracy between c and ω, since a centrally peaked brightness distribution can supress the measured centroid displacements across all apertures, weighting the centroid more strongly toward the core. SPT2215 is expected to be heavily affected by this effect, as it can be seen in Figure 5.1 from its highly peaked surface brightness distribution in the 3D space.

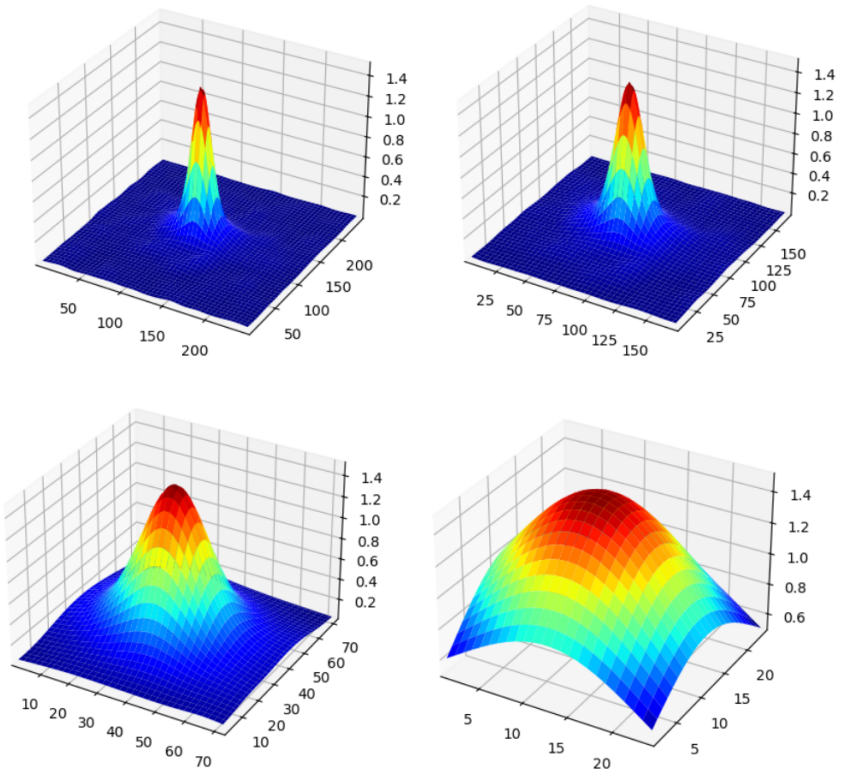

Figure 5.1: SPT2215's 3D brightness map with different apertures.

Naturally, if one has to use a single morphological parameter to classify the dynamical state of a test sample, this feature can be seen as a strength, since it somehow captures two different aspects of the emission distribution: the central cuspiness, indicating the presence of a structured cool core, and assymetries, quantifying the presence of substructures. For large samples, it can be effective in distinguishing highly dynamically disturbed clusters from very relaxed ones. For instance, Maughan et al. (2008) used a core-excised ω as a single relaxation proxy for a sample of 115 clusters in the range $0.1 < z < 1.3$, finding a clear absence of highly relaxed clusters at $z > 0.5$. We argue that this degeneracy becomes particularly problematic for high-redshift clusters when the core contribution is included. We suggest that the low purity for $c \times \omega$ seen in Figure 4.8(a) is caused by a combination of this degeneracy and a poorly modeled redshift dependence of c.

The surface brightness peakiness (p) from SPA is a more refined version of c, since it is measured under a same scaled surface brightness level by assuming a self-similar model, and it includes a $(1 + z)$ term, which results in a nearly constant fraction of peaked clusters across redshift. The other two statistics are the symmetry (s) and the alignment (a) as defined in Mantz et al. (2015). For SPT2215, the SPA measurements are $s = 1.24 \pm 0.15$, $p = -0.46 \pm 0.04$ and $a = 1.42 \pm 0.16$ (Calzadilla et al. 2023). Upon visual inspection of Figure 2 of their paper, we notice that the $a \times s$ space yields a

lower purity compared to $s \times p$ and $a \times p$, suggesting that p carries a greater weight in distinguishing the dynamical state. CBV21 points out that the redshift evolution of p, even with the $(1+z)$ term, is too strong, producing larger subsamples of relaxed clusters with increasing redshift. By fitting the morphological parameters with a $(1+z)^{-\beta}$ factor, they found $\beta(s) = 0.59 \pm 0.18$, $\beta(p) = 3.42 \pm 0.49$ and $\beta(a) = 1.38 \pm 0.21$. Applying these corrections to the original SPA measurements, we get $s_z = 1.04 \pm 0.16$, $p_z = -1.60 \pm 0.17$ and $a_z = 0.96 \pm 0.17$. For the sake of comparison, if we keep the original relaxation thresholds ($s > 0.87$, $p > -0.82$ and $a > 1.00$), then s marginally passes the criterion, p strongly fails and a remains in the borderline. Therefore, once the redshift evolution is accounted for, we find a scenario that is much more consistent with an intermediate dynamical state, which matches the near-zero morphology index $\delta = 0.028$ and the more central $\log_{10}(P_3/P_0) = -6.58$ value (although more consistent with the disturbed subsample distribution in this case).

5.5 Physical Interpretation of Cuspiness Enhancement

It seems that, at high-redshift, a centrally peaked emission is not as strong an indicator of a virialized state as it is in the local universe. The most straightforward reason would be that a surviving post-merger cool core under a high merger rate regime, can retain a high peakiness, even when the cluster remains dynamically disturbed. But we argue this can also be the contribution of competing physical processes, particularly related to a not yet fully regulated AGN feedback cycle at earlier cosmic times, as pointed by Calzadilla et al. (2024). Our combined analysis, together with the interpretation given in Section 5.4, supports the idea that SPT2215 is experiencing extreme thermal imbalance during the period between an outburst event and the development of a two-phase entropy structure, which can be creating a cooling-dominated regime that amplifies the surface brightness cuspiness while not necessarily reflecting strong virialization. Thus, what we might be seeing in SPT2215 is a short transient state in which feedback has been recently triggered and has not yet had sufficient time to offset the overwhelming cooling, which in turn dominates the central X-ray emission and bias morphological criteria towards relaxation.

Chapter 6

Summary and Conclusions

6.1 Summary

We present a detailed revision of the dynamical state of the high-redshift galaxy cluster SPT-CL J2215-3537, based on a comprehensive X-ray analysis of all currently available Chandra observations, and provide a discussion on the use of morphological statistics to assess relaxation in the high-redshift regime. Our results and conclusions can be summarized as follows:

1. The thermodynamic characterization of SPT2215 reveals significant anisotropies, including off-center clumps of colder gas toward the eastern direction and features consistent with cold front signatures near the cooling radius along the SE–NW axis. The β-model-subtracted residual show a central dipolar pattern along the SE–NW direction and arc-shaped surface brightness excess across different scales, both features consistent with a core sloshing scenario.

2. We propose that a past off-axis merger with a gas-poor structure triggered core sloshing. The steep entropy profile in the core would allow the resulting oscillatory, subsonic gas motions to generate the observed cold fronts near the edges of the cool core. These bulk motions may also create a preferential channel for the inflow of low-entropy gas, potentially enhancing star formation along the SE–NW axis.

3. The residual map reveals a candidate ghost bubble located approximately 230 kpc to the NW. Although the observed features of the cavity deviate significantly from known empirical relations, the derived $P_{\rm cav}$ is consistent with the previous estimative from the $P_{\rm cav}$-$L_{\rm cool}$ scaling relation, indicating that radiative cooling is currently outweighing AGN feedback.

4. The main properties of SPT2215's core can be well explained by the precipitation-regulated framework developed by Voit et al. (2015). Our combined analysis indi-

cates that SPT2215 is currently in the early phase of progression towards a long-lasting self-regulated. At present, condensation appears to be mostly confined to the inner regions ($\sim 25 \pm 6$ kpc) and the entropy distribution at each radius is still inhomogeneous out to $\sim 180 \pm 40$ kpc along the SW-NE axis.

5. We compute traditional morphological parameters for our merged X-ray image and find a morphology index $\delta = 0.028$ and power ratio $\log_{10}(P_3/P_0) = -6.58$ consistent with a mildly disturbed system, but a concentration $\log_{10}(c) = -0.33$ and centroid shift $\log_{10}(\omega) = -2.57$ characteristic of highly relaxed systems. We discuss evidence suggesting that these values are biased due to a strong redshift-evolution of morphological measures associated to the central emission cuspiness. We reevaluate the SPA criteria, which had previously classified SPT2215 as dynamically relaxed, noticing that the peakiness statistic carries a greater weight in placing the system in the relaxed locus of the parameter space. When applying the redshift dependences indicated by CBV21, we find new SPA measurements ($s_z = 1.04 \pm 0.16$, $p_z = -1.60 \pm 0.17$ and $a_z = 0.96 \pm 0.17$), which are now consistent with an intermediate dynamical state.

6. We propose that the strong redshift-dependence of the peakiness and concentration parameters is related to an undeveloped cooling-feedback cycle at high-redshift. The complex non-gravitational processes in galaxy clusters would then lead to a non-self-similar evolution of parameters tracing core brightness structure. In other words, a peaked cluster at high-redshift does not imply a virialized dynamical state as strongly as it does at low redshift due to the increased prevalence of transient or rapidly evolving core conditions at earlier cosmic times. Of course, this hypothesis must be tested statistically rather than based on a single system. We intend to pursue this in a forthcoming analysis (Bessa et al., in prep).

Our joint analysis indicates that SPT2215 is a mildly disturbed high-redshift cluster hosting a structured but thermodynamically complex cool core. This scenario suggests that the accuracy of the cluster's total mass estimate will ultimately be limited by systematics associated with the HSE assumption, rather than by the quality of current or future X-ray data. Nevertheless, we reiterate the relevance of follow-up observations of SPT2215, since this system represents an ideal case for understanding the cooling-feedback cycle and out-of-equilibrium conditions in the cores of high-redshift galaxy clusters. Particularly, an observation with the future Advanced X-ray Imaging Satellite (AXIS) (Russell et al. 2024) would allow for enough statistics to generate thermodynamic maps with significantly enhanced spatial resolution and coverage, probing potential new features such as gas motions beyond the cold fronts, abundance distributions, fainter X-ray cavities and more. Additionally, the intermediate dynamical state could be independently confirmed

with the James Webb Space Telescope through measurements of $f_{\rm ICL}$ in a set of bands that best probe the intracluster light excess, corresponding to the rest-frame wavelength interval 5200–8500 Å (Jiménez-Teja et al. 2018).

Bibliography

Allen, S. W., R. W. Schmidt, and A. C. Fabian (Aug. 2002). "Cosmological constraints from the X-ray gas mass fraction in relaxed lensing clusters observed with Chandra". In: Mon. Not, Roy. Astron. Soc. 334.2, pp. L11–L15. DOI: 10.1046/j.1365-8711.2002.05601.x. arXiv: astro-ph/0205007 [astro-ph].

Allen, S. W. et al. (Sept. 2004). "Constraints on dark energy from Chandra observations of the largest relaxed galaxy clusters". In: Mon. Not, Roy. Astron. Soc. 353.2, pp. 457–467. DOI: 10.1111/j.1365-2966.2004.08080.x. arXiv: astro-ph/0405340 [astro-ph].

Allen, S. W. et al. (Jan. 2008). "Improved constraints on dark energy from Chandra X-ray observations of the largest relaxed galaxy clusters". In: Mon. Not, Roy. Astron. Soc. 383.3, pp. 879–896. DOI: 10.1111/j.1365-2966.2007.12610.x. arXiv: 0706.0033 [astro-ph].

Anders, E. and N. Grevesse (Jan. 1989). "Abundances of the elements: Meteoritic and solar". In: Geochim. Cosmochim. Acta 53.1, pp. 197–214. DOI: 10.1016/0016-7037(89)90286-X.

Arnaud, K. A. (Jan. 1996). "XSPEC: The First Ten Years". In: *Astronomical Data Analysis Software and Systems V*. Ed. by George H. Jacoby and Jeannette Barnes. Vol. 101. Astronomical Society of the Pacific Conference Series, p. 17.

Ascasibar, Yago and Maxim Markevitch (Oct. 2006). "The Origin of Cold Fronts in the Cores of Relaxed Galaxy Clusters". In: Astrophys. J. 650.1, pp. 102–127. DOI: 10.1086/506508. arXiv: astro-ph/0603246 [astro-ph].

Bahcall, Neta A. and Renyue Cen (Apr. 1993). "The Mass Function of Clusters of Galaxies". In: Astrophys. J. Lett. 407, p. L49. DOI: 10.1086/186803.

Barnes, David J. et al. (Sept. 2021). "Characterizing hydrostatic mass bias with MOCK-X". In: Mon. Not, Roy. Astron. Soc. 506.2, pp. 2533–2550. DOI: 10.1093/mnras/stab1276. arXiv: 2001.11508 [astro-ph.CO].

Bautz, L. P. and W. W. Morgan (Dec. 1970). "On the Classification of the Forms of Clusters of Galaxies". In: Astrophys. J. Lett. 162, p. L149. DOI: 10.1086/180643.

Bleem, L. E. et al. (Mar. 2020). "The SPTpol Extended Cluster Survey". In: Astrophys. J. Suppl. 247.1, 25, p. 25. DOI: 10.3847/1538-4365/ab6993. arXiv: 1910.04121 [astro-ph.CO].

Bourne, Martin A. and Hsiang-Yi Karen Yang (June 2023). "Recent Progress in Modeling the Macro- and Micro-Physics of Radio Jet Feedback in Galaxy Clusters". In: *Galaxies* 11.3, 73, p. 73. DOI: 10.3390/galaxies11030073. arXiv: 2305.00019 [astro-ph.HE].

Buote, David A. and John C. Tsai (Oct. 1995). "Quantifying the Morphologies and Dynamical Evolution of Galaxy Clusters. I. The Method". In: Astrophys. J. 452, p. 522. DOI: 10.1086/176326. arXiv: astro-ph/9502002 [astro-ph].

— (Feb. 1996). "Quantifying the Morphologies and Dynamical Evolution of Galaxy Clusters. II. Application to a Sample of ROSAT Clusters". In: Astrophys. J. 458, p. 27. DOI: 10.1086/176790. arXiv: astro-ph/9504046 [astro-ph].

Calzadilla, Michael S. et al. (Apr. 2023). "SPT-CL J2215-3537: A Massive Starburst at the Center of the Most Distant Relaxed Galaxy Cluster". In: Astrophys. J. 947.2, 44, p. 44. DOI: 10.3847/1538-4357/acc6c2. arXiv: 2303.10185 [astro-ph.GA].

Calzadilla, Michael S. et al. (Dec. 2024). "The SPT-Chandra BCG Spectroscopic Survey. I. Evolution of the Entropy Threshold for ICM Cooling and AGN Feedback in Galaxy Clusters over the Last 10 Gyr". In: Astrophys. J. 976.2, 169, p. 169. DOI: 10.3847/1538-4357/ad8916. arXiv: 2311.00396 [astro-ph.GA].

Cao, Kaili, David J. Barnes, and Mark Vogelsberger (May 2021). "Studying galaxy cluster morphological metrics with MOCK-X". In: Mon. Not, Roy. Astron. Soc. 503.3, pp. 3394–3413. DOI: 10.1093/mnras/stab605. arXiv: 2006.10752 [astro-ph.CO].

Cappellari, Michele and Yannick Copin (June 2003). "Adaptive spatial binning of integral-field spectroscopic data using Voronoi tessellations". In: Mon. Not, Roy. Astron. Soc. 342.2, pp. 345–354. DOI: 10.1046/j.1365-8711.2003.06541.x. arXiv: astro-ph/0302262 [astro-ph].

Carlstrom, John E., Gilbert P. Holder, and Erik D. Reese (Jan. 2002). "Cosmology with the Sunyaev-Zel'dovich Effect". In: Ann. Rev. Astron. Astrohys. 40, pp. 643–680. DOI: 10.1146/annurev.astro.40.060401.093803. arXiv: astro-ph/0208192 [astro-ph].

Cavagnolo, K. W. et al. (Sept. 2010). "A Relationship Between AGN Jet Power and Radio Power". In: Astrophys. J. 720.2, pp. 1066–1072. DOI: 10.1088/0004-637X/720/2/1066. arXiv: 1006.5699 [astro-ph.CO].

Cavagnolo, Kenneth W. et al. (May 2009). "Intracluster Medium Entropy Profiles for a Chandra Archival Sample of Galaxy Clusters". In: Astrophys. J. Suppl. 182.1, pp. 12–32. DOI: 10.1088/0067-0049/182/1/12. arXiv: 0902.1802 [astro-ph.CO].

Clarke, T. E., Elizabeth L. Blanton, and Craig L. Sarazin (Nov. 2004). "The Complex Cooling Core of A2029: Radio and X-Ray Interactions". In: Astrophys. J. 616.1, pp. 178–191. DOI: 10.1086/424911. arXiv: astro-ph/0408068 [astro-ph].

Diehl, Steven and Thomas S. Statler (May 2006). "Adaptive binning of X-ray data with weighted Voronoi tessellations". In: Mon. Not, Roy. Astron. Soc. 368.2, pp. 497–510. DOI: 10.1111/j.1365-2966.2006.10125.x. arXiv: astro-ph/0512074 [astro-ph].

Dunn, R. J. H. and A. C. Fabian (Dec. 2006). "Investigating AGN heating in a sample of nearby clusters". In: Mon. Not, Roy. Astron. Soc. 373.3, pp. 959–971. DOI: 10.1111/j.1365-2966.2006.11080.x. arXiv: astro-ph/0609537 [astro-ph].

Dupke, Renato, Raymond E. White III, and Joel N. Bregman (Dec. 2007). "Different Methods of Forming Cold Fronts in Nonmerging Clusters". In: Astrophys. J. 671.1, pp. 181–189. DOI: 10.1086/522194. arXiv: 0707.4001 [astro-ph].

Ettori, S. et al. (July 2009). "The cluster gas mass fraction as a cosmological probe: a revised study". In: Astron. Astrophys. 501.1, pp. 61–73. DOI: 10.1051/0004-6361/200810878. arXiv: 0904.2740 [astro-ph.CO].

Evrard, August E., Christopher A. Metzler, and Julio F. Navarro (Oct. 1996). "Mass Estimates of X-Ray Clusters". In: Astrophys. J. 469, p. 494. DOI: 10.1086/177798. arXiv: astro-ph/9510058 [astro-ph].

Fabian, A. C. (Jan. 1994). "Cooling Flows in Clusters of Galaxies". In: Ann. Rev. Astron. Astrohys. 32, pp. 277–318. DOI: 10.1146/annurev.aa.32.090194.001425.

— (June 2003). "Cluster cores and cooling flows". In: *Revista Mexicana de Astronomia y Astrofisica Conference Series*. Ed. by Vladimir Avila-Reese et al. Vol. 17. Revista Mexicana de Astronomia y Astrofisica Conference Series, pp. 303–313. DOI: 10.48550/arXiv.astro-ph/0210150. arXiv: astro-ph/0210150 [astro-ph].

Fabian, A. C. et al. (June 2005). "A deep Chandra observation of the Centaurus cluster: bubbles, filaments and edges". In: Mon. Not, Roy. Astron. Soc. 360.1, pp. L20–L24. DOI: 10.1111/j.1745-3933.2005.00037.x. arXiv: astro-ph/0503154 [astro-ph].

Fixsen, D. J. (Dec. 2009). "The Temperature of the Cosmic Microwave Background". In: Astrophys. J. 707.2, pp. 916–920. DOI: 10.1088/0004-637X/707/2/916. arXiv: 0911.1955 [astro-ph.CO].

Ghizzardi, S., M. Rossetti, and S. Molendi (June 2010). "Cold fronts in galaxy clusters". In: Astron. Astrophys. 516, A32, A32. DOI: 10.1051/0004-6361/200912496. arXiv: 1003.1051 [astro-ph.CO].

Ghizzardi, Simona et al. (July 2004). "Radiative Cooling and Heating and Thermal Conduction in M87". In: Astrophys. J. 609.2, pp. 638–651. DOI: 10.1086/421314. arXiv: astro-ph/0404060 [astro-ph].

Gitti, Myriam, Fabrizio Brighenti, and Brian R. McNamara (Jan. 2012). "Evidence for AGN Feedback in Galaxy Clusters and Groups". In: *Advances in Astronomy* 2012, 950641, p. 950641. DOI: 10.1155/2012/950641. arXiv: 1109.3334 [astro-ph.CO].

Haiman, Zoltán, Joseph J. Mohr, and Gilbert P. Holder (June 2001). "Constraints on Cosmological Parameters from Future Galaxy Cluster Surveys". In: Astrophys. J. 553.2, pp. 545–561. DOI: 10.1086/320939. arXiv: astro-ph/0002336 [astro-ph].

Hashimoto, Yasuhiro et al. (May 2007). "Robust quantitative measures of cluster X-ray morphology, and comparisons between cluster characteristics". In: Astron. Astrophys.

467.2, pp. 485–499. DOI: 10.1051/0004-6361:20065125. arXiv: astro-ph/0611804 [astro-ph].

HI4PI Collaboration et al. (Oct. 2016). "HI4PI: A full-sky H I survey based on EBHIS and GASS". In: Astron. Astrophys. 594, A116, A116. DOI: 10.1051/0004-6361/201629178. arXiv: 1610.06175 [astro-ph.GA].

Hlavacek-Larrondo, J et al. (2015). "X-Ray Cavities in a Sample of 83 SPT-selected Clusters of Galaxies: Tracing the Evolution of AGN Feedback in Clusters of Galaxies out to z= 1.2". In: *The Astrophysical Journal* 805.1, p. 35.

Iqbal, Asif et al. (Jan. 2023). "Heating of the intracluster medium by buoyant bubbles and sound waves". In: Mon. Not, Roy. Astron. Soc. 518.2, pp. 2735–2745. DOI: 10.1093/mnras/stac3197. arXiv: 2203.13340 [astro-ph.CO].

Jeltema, Tesla E. et al. (May 2005). "The Evolution of Structure in X-Ray Clusters of Galaxies". In: Astrophys. J. 624.2, pp. 606–629. DOI: 10.1086/428940. arXiv: astro-ph/0501360 [astro-ph].

Jiménez-Teja, Y. et al. (Aug. 2023). "Dissecting the RELICS cluster SPT-CLJ0615-5746 through intracluster light: Confirmation of the multiple merging state of the cluster formation". In: Astron. Astrophys. 676, A39, A39. DOI: 10.1051/0004-6361/202346580. arXiv: 2305.10860 [astro-ph.GA].

Jiménez-Teja, Yolanda et al. (Apr. 2018). "Unveiling the Dynamical State of Massive Clusters through the ICL Fraction". In: Astrophys. J. 857.2, 79, p. 79. DOI: 10.3847/1538-4357/aab70f. arXiv: 1803.04981 [astro-ph.GA].

Kennicutt Jr., Robert C. (Jan. 1998). "Star Formation in Galaxies Along the Hubble Sequence". In: Ann. Rev. Astron. Astrohys. 36, pp. 189–232. DOI: 10.1146/annurev.astro.36.1.189. arXiv: astro-ph/9807187 [astro-ph].

Kravtsov, Andrey V. and Stefano Borgani (Sept. 2012). "Formation of Galaxy Clusters". In: Ann. Rev. Astron. Astrohys. 50, pp. 353–409. DOI: 10.1146/annurev-astro-081811-125502. arXiv: 1205.5556 [astro-ph.CO].

Landau, Lev Davidovich and E. M. Lifshitz (1959). *Fluid mechanics*.

Lau, Erwin T., Andrey V. Kravtsov, and Daisuke Nagai (Nov. 2009). "Residual Gas Motions in the Intracluster Medium and Bias in Hydrostatic Measurements of Mass Profiles of Clusters". In: Astrophys. J. 705.2, pp. 1129–1138. DOI: 10.1088/0004-637X/705/2/1129. arXiv: 0903.4895 [astro-ph.CO].

Lee, Wonki et al. (Mar. 2023). "Weak-lensing Mass Bias in Merging Galaxy Clusters". In: Astrophys. J. 945.1, 71, p. 71. DOI: 10.3847/1538-4357/acb76b. arXiv: 2211.03892 [astro-ph.CO].

Lehle, Katrin et al. (July 2024). "The heart of galaxy clusters: Demographics and physical properties of cool-core and non-cool-core halos in the TNG-Cluster simulation". In: Astron. Astrophys. 687, A129, A129. DOI: 10.1051/0004-6361/202348609. arXiv: 2311.06333 [astro-ph.GA].

Li, Yuan et al. (Oct. 2015). "Cooling, AGN Feedback, and Star Formation in Simulated Cool-core Galaxy Clusters". In: Astrophys. J. 811.2, 73, p. 73. DOI: 10.1088/0004-637X/811/2/73. arXiv: 1503.02660 [astro-ph.GA].

Mahdavi, A. et al. (Mar. 2008). "Evidence for non-hydrostatic gas from the cluster X-ray to lensing mass ratio". In: Mon. Not, Roy. Astron. Soc. 384.4, pp. 1567–1574. DOI: 10.1111/j.1365-2966.2007.12796.x. arXiv: 0710.4132 [astro-ph].

Main, R. A. et al. (Feb. 2017). "A relationship between halo mass, cooling, active galactic nuclei heating and the co-evolution of massive black holes". In: Mon. Not, Roy. Astron. Soc. 464.4, pp. 4360–4382. DOI: 10.1093/mnras/stw2644. arXiv: 1510.07046 [astro-ph.GA].

Mantz, A. B. et al. (May 2014). "Cosmology and astrophysics from relaxed galaxy clusters - II. Cosmological constraints". In: Mon. Not, Roy. Astron. Soc. 440.3, pp. 2077–2098. DOI: 10.1093/mnras/stu368. arXiv: 1402.6212 [astro-ph.CO].

Mantz, Adam B. et al. (May 2015). "Cosmology and astrophysics from relaxed galaxy clusters - I. Sample selection". In: Mon. Not, Roy. Astron. Soc. 449.1, pp. 199–219. DOI: 10.1093/mnras/stv219. arXiv: 1502.06020 [astro-ph.CO].

Mantz, Adam B. et al. (Feb. 2022). "Cosmological constraints from gas mass fractions of massive, relaxed galaxy clusters". In: Mon. Not, Roy. Astron. Soc. 510.1, pp. 131–145. DOI: 10.1093/mnras/stab3390. arXiv: 2111.09343 [astro-ph.CO].

Markevitch, M., A. Vikhlinin, and P. Mazzotta (Dec. 2001). "Nonhydrostatic Gas in the Core of the Relaxed Galaxy Cluster A1795". In: Astrophys. J. Lett. 562.2, pp. L153–L156. DOI: 10.1086/337973. arXiv: astro-ph/0108520 [astro-ph].

Markevitch, M. et al. (Oct. 2000). "Chandra Observation of Abell 2142: Survival of Dense Subcluster Cores in a Merger". In: Astrophys. J. 541.2, pp. 542–549. DOI: 10.1086/309470. arXiv: astro-ph/0001269 [astro-ph].

Markevitch, Maxim and Alexey Vikhlinin (May 2007). "Shocks and cold fronts in galaxy clusters". In: Phys. Rep. 443.1, pp. 1–53. DOI: 10.1016/j.physrep.2007.01.001. arXiv: astro-ph/0701821 [astro-ph].

Markevitch, Maxim et al. (2005). "Bow shock and radio halo in the merging cluster A520". In: *The Astrophysical Journal* 627.2, p. 733.

Maughan, B. J. et al. (Jan. 2008). "Images, Structural Properties, and Metal Abundances of Galaxy Clusters Observed with Chandra ACIS-I at $0.1 < z < 1.3$". In: Astrophys. J. Suppl. 174.1, pp. 117–135. DOI: 10.1086/521225. arXiv: astro-ph/0703156 [astro-ph].

Mills, B. Y. (Sept. 1960). "On the Identification of Extragalactic Radio Sources". In: *Australian Journal of Physics* 13, p. 550. DOI: 10.1071/PH600550.

Nagai, Daisuke, Alexey Vikhlinin, and Andrey V. Kravtsov (Jan. 2007). "Testing X-Ray Measurements of Galaxy Clusters with Cosmological Simulations". In: Astrophys. J. 655.1, pp. 98–108. DOI: 10.1086/509868. arXiv: astro-ph/0609247 [astro-ph].

Nelson, Dylan et al. (May 2019). "The IllustrisTNG simulations: public data release". In: *Computational Astrophysics and Cosmology* 6.1, 2, p. 2. DOI: 10.1186/s40668-019-0028-x. arXiv: 1812.05609 [astro-ph.GA].

Nelson, Kaylea, Erwin T. Lau, and Daisuke Nagai (Sept. 2014). "Hydrodynamic Simulation of Non-thermal Pressure Profiles of Galaxy Clusters". In: Astrophys. J. 792.1, 25, p. 25. DOI: 10.1088/0004-637X/792/1/25. arXiv: 1404.4636 [astro-ph.CO].

Nelson, Kaylea et al. (June 2012). "Evolution of the Merger-induced Hydrostatic Mass Bias in Galaxy Clusters". In: Astrophys. J. 751.2, 121, p. 121. DOI: 10.1088/0004-637X/751/2/121. arXiv: 1112.3659 [astro-ph.CO].

Overzier, Roderik A. (Nov. 2016). "The realm of the galaxy protoclusters. A review". In: Astron. Astrophys. Rev. 24.1, 14, p. 14. DOI: 10.1007/s00159-016-0100-3. arXiv: 1610.05201 [astro-ph.GA].

Paerels, Frederik B. S. and Steven M. Kahn (Jan. 2003). "High-Resolution X-Ray Spectroscopy with CHANDRA and XMM-NEWTON". In: Ann. Rev. Astron. Astrohys. 41, pp. 291–342. DOI: 10.1146/annurev.astro.41.071601.165952.

Parekh, Viral et al. (Mar. 2015). "Morphology parameters: substructure identification in X-ray galaxy clusters". In: Astron. Astrophys. 575, A127, A127. DOI: 10.1051/0004-6361/201424123. arXiv: 1411.6525 [astro-ph.CO].

Planck Collaboration et al. (Sept. 2020a). "Planck 2018 results. I. Overview and the cosmological legacy of Planck". In: Astron. Astrophys. 641, A1, A1. DOI: 10.1051/0004-6361/201833880. arXiv: 1807.06205 [astro-ph.CO].

Planck Collaboration et al. (Sept. 2020b). "Planck 2018 results. VII. Isotropy and statistics of the CMB". In: Astron. Astrophys. 641, A7, A7. DOI: 10.1051/0004-6361/201935201. arXiv: 1906.02552 [astro-ph.CO].

Plionis, Manolis, John D. Barrow, and Carlos S. Frenk (Apr. 1991). "Projected and intrinsic shapes of galaxy clusters." In: Mon. Not, Roy. Astron. Soc. 249, p. 662. DOI: 10.1093/mnras/249.4.662.

Poole, Gregory B. et al. (Dec. 2006). "The impact of mergers on relaxed X-ray clusters - I. Dynamical evolution and emergent transient structures". In: Mon. Not, Roy. Astron. Soc. 373.3, pp. 881–905. DOI: 10.1111/j.1365-2966.2006.10916.x. arXiv: astro-ph/0608560 [astro-ph].

Press, William H. and Paul Schechter (Feb. 1974). "Formation of Galaxies and Clusters of Galaxies by Self-Similar Gravitational Condensation". In: Astrophys. J. 187, pp. 425–438. DOI: 10.1086/152650.

Rasia, E. et al. (July 2006). "Systematics in the X-ray cluster mass estimators". In: Mon. Not, Roy. Astron. Soc. 369.4, pp. 2013–2024. DOI: 10.1111/j.1365-2966.2006.10466.x. arXiv: astro-ph/0602434 [astro-ph].

Rasia, Elena, Giuseppe Tormen, and Lauro Moscardini (June 2004). "A dynamical model for the distribution of dark matter and gas in galaxy clusters". In: Mon. Not, Roy.

Astron. Soc. 351.1, pp. 237–252. DOI: 10.1111/j.1365-2966.2004.07775.x. arXiv: astro-ph/0309405 [astro-ph].

Rood, Herbert J. and Gummuluru N. Sastry (June 1971). ""Tuning Fork" Classification of Rich Clusters of Galaxies". In: Publ. Astron. Soc. Pacific 83.493, p. 313. DOI: 10.1086/129128.

Russell, Helen R. et al. (June 2024). "The Evolution of Galaxies and Clusters at High Spatial Resolution with Advanced X-ray Imaging Satellite (AXIS)". In: *Universe* 10.7, 273, p. 273. DOI: 10.3390/universe10070273. arXiv: 2311.07661 [astro-ph.IM].

Ryden, Barbara (2016). *Introduction to Cosmology*. Provided by the SAO/NASA Astrophysics Data System. Cambridge University Press. URL: https://ui.adsabs.harvard.edu/abs/2016inco.book.....R.

Sachs, R. K. and A. M. Wolfe (Jan. 1967). "Perturbations of a Cosmological Model and Angular Variations of the Microwave Background". In: Astrophys. J. 147, p. 73. DOI: 10.1086/148982.

Santos, J. S. et al. (May 2008). "Searching for cool core clusters at high redshift". In: Astron. Astrophys. 483.1, pp. 35–47. DOI: 10.1051/0004-6361:20078815. arXiv: 0802.1445 [astro-ph].

Sarazin, Craig L. (1988). *X-ray Emission from Clusters of Galaxies*. Provided by the SAO/NASA Astrophysics Data System. Cambridge University Press. URL: https://ui.adsabs.harvard.edu/abs/1988xrec.book.....S.

Sasaki, Shin (Dec. 1996). "A New Method to Estimate Cosmological Parameters Using the Baryon Fraction of Clusters of Galaxies". In: Publ. Astron. Soc. Japan 48, pp. L119–L122. DOI: 10.1093/pasj/48.6.L119. arXiv: astro-ph/9611033 [astro-ph].

Seward, Frederick D. and Philip A. Charles (2010). *Exploring the X-ray Universe*.

Shin, Jaejin, Jong-Hak Woo, and John S. Mulchaey (Dec. 2016). "A Systematic Search for X-Ray Cavities in Galaxy Clusters, Groups, and Elliptical Galaxies". In: Astrophys. J. Suppl. 227.2, 31, p. 31. DOI: 10.3847/1538-4365/227/2/31. arXiv: 1610.03487 [astro-ph.CO].

Springel, Volker, Carlos S. Frenk, and Simon D. M. White (Apr. 2006). "The large-scale structure of the Universe". In: Nature 440.7088, pp. 1137–1144. DOI: 10.1038/nature04805. arXiv: astro-ph/0604561 [astro-ph].

Springel, Volker et al. (June 2005). "Simulations of the formation, evolution and clustering of galaxies and quasars". In: Nature 435.7042, pp. 629–636. DOI: 10.1038/nature03597. arXiv: astro-ph/0504097 [astro-ph].

Staniszewski, Z. et al. (Aug. 2009). "Galaxy Clusters Discovered with a Sunyaev-Zel'dovich Effect Survey". In: Astrophys. J. 701.1, pp. 32–41. DOI: 10.1088/0004-637X/701/1/32. arXiv: 0810.1578 [astro-ph].

Struble, M. F. and H. J. Rood (Jan. 1982). "Morphological classification (revised RS) of Abell clusters in D<4 and an analysis of observed correlations." In: Astron. J. 87, pp. 7–46. DOI: 10.1086/113081.

Sunyaev, R. A. and Ia. B. Zeldovich (Jan. 1980). "Microwave background radiation as a probe of the contemporary structure and history of the universe". In: Ann. Rev. Astron. Astrohys. 18, pp. 537–560. DOI: 10.1146/annurev.aa.18.090180.002541.

Sunyaev, R. A. and Ya. B. Zeldovich (Nov. 1972). "The Observations of Relic Radiation as a Test of the Nature of X-Ray Radiation from the Clusters of Galaxies". In: *Comments on Astrophysics and Space Physics* 4, p. 173.

Tozzi, Paolo and Colin Norman (Jan. 2001). "The Evolution of X-Ray Clusters and the Entropy of the Intracluster Medium". In: Astrophys. J. 546.1, pp. 63–84. DOI: 10.1086/318237. arXiv: astro-ph/0003289 [astro-ph].

van den Bergh, Sidney (Nov. 1961). "Radio Sources and Clusters of Galaxies." In: Astrophys. J. 134, p. 970. DOI: 10.1086/147224.

Vikhlinin, A., M. Markevitch, and S. S. Murray (Apr. 2001). "A Moving Cold Front in the Intergalactic Medium of A3667". In: Astrophys. J. 551.1, pp. 160–171. DOI: 10.1086/320078. arXiv: astro-ph/0008496 [astro-ph].

Vikhlinin, A. et al. (Apr. 2006). "Chandra Sample of Nearby Relaxed Galaxy Clusters: Mass, Gas Fraction, and Mass-Temperature Relation". In: Astrophys. J. 640.2, pp. 691–709. DOI: 10.1086/500288. arXiv: astro-ph/0507092 [astro-ph].

Voit, G. M. et al. (Mar. 2015). "Regulation of star formation in giant galaxies by precipitation, feedback and conduction". In: Nature 519.7542, pp. 203–206. DOI: 10.1038/nature14167. arXiv: 1409.1598 [astro-ph.GA].

Voit, G. Mark, Scott T. Kay, and Greg L. Bryan (Dec. 2005). "The baseline intracluster entropy profile from gravitational structure formation". In: Mon. Not, Roy. Astron. Soc. 364.3, pp. 909–916. DOI: 10.1111/j.1365-2966.2005.09621.x. arXiv: astro-ph/0511252 [astro-ph].

Voit, G. Mark et al. (Aug. 2017). "A Global Model for Circumgalactic and Cluster-core Precipitation". In: Astrophys. J. 845.1, 80, p. 80. DOI: 10.3847/1538-4357/aa7d04. arXiv: 1607.02212 [astro-ph.GA].

von der Linden, Anja et al. (Sept. 2014). "Robust weak-lensing mass calibration of Planck galaxy clusters". In: Mon. Not, Roy. Astron. Soc. 443.3, pp. 1973–1978. DOI: 10.1093/mnras/stu1423. arXiv: 1402.2670 [astro-ph.CO].

Weisskopf, M. C. et al. (Jan. 2002). "An Overview of the Performance and Scientific Results from the Chandra X-Ray Observatory". In: Publ. Astron. Soc. Pacific 114.791, pp. 1–24. DOI: 10.1086/338108. arXiv: astro-ph/0110308 [astro-ph].

White, Simon D. M. et al. (Dec. 1993). "The baryon content of galaxy clusters: a challenge to cosmological orthodoxy". In: Nature 366.6454, pp. 429–433. DOI: 10.1038/366429a0.

Yuan, Z. S. and J. L. Han (Aug. 2020). "Dynamical state for 964 galaxy clusters from Chandra X-ray images". In: *Monthly Notices of the Royal Astronomical Society* 497.4, pp. 5485–5497. ISSN: 0035-8711. DOI: 10.1093/mnras/staa2363. eprint: https://academic.oup.com/mnras/article-pdf/497/4/5485/33695831/staa2363.pdf. URL: https://doi.org/10.1093/mnras/staa2363.

Yuan, Z. S., J. L. Han, and Z. L. Wen (June 2022). "Dynamical state of galaxy clusters evaluated from X-ray images". In: Mon. Not, Roy. Astron. Soc. 513.2, pp. 3013–3021. DOI: 10.1093/mnras/stac1037. arXiv: 2204.02699 [astro-ph.GA].

Zenteno, A. et al. (June 2020). "A joint SZ-X-ray-optical analysis of the dynamical state of 288 massive galaxy clusters". In: Mon. Not, Roy. Astron. Soc. 495.1, pp. 705–725. DOI: 10.1093/mnras/staa1157. arXiv: 2004.01721 [astro-ph.GA].

Zhang, Congyao et al. (June 2024). "Mapping the intracluster medium in the era of high-resolution X-ray spectroscopy". In: Mon. Not, Roy. Astron. Soc. 530.4, pp. 4234–4255. DOI: 10.1093/mnras/stae1022. arXiv: 2310.02225 [astro-ph.HE].

ZuHone, J. A. et al. (Jan. 2013). "Cold Fronts and Gas Sloshing in Galaxy Clusters with Anisotropic Thermal Conduction". In: Astrophys. J. 762.2, 69, p. 69. DOI: 10.1088/0004-637X/762/2/69. arXiv: 1204.6005 [astro-ph.CO].

Zwicky, Fritz, E Herzog, and P Wild (1968). "Catalogue of Galaxies and of Clusters of Galaxies". In: *Pasadena: California Institute of Technology (CIT)*.